DEGRADATIONS AND IMPROVEMENTS IN PEM FUEL CELL MATERIALS: A COMPUTATIONAL STUDY

Thesis by

Ted Yu

In Partial Fulfillment of the Requirements

for the Degree of

Doctor of Philosophy

California Institute of Technology

Pasadena, California

2012

(Defended March 6, 2012)

Acknowledgement:

I would first of all like to thank God for giving me this opportunity to work on science and to try to unravel the mysteries of his beautiful universe. To my wife and daughter who I think about all the time. Thanks to my parents who taught me to be goal-oriented and creative. And my family members who have been so supportive. Thank you Professor Goddard for being such a spark of intellectual curiosity. To all the other professors at Caltech who may have unknowingly taught me the most important value, scientific integrity. Thanks to Pastor Raymond Petzholt and the MBCP family for praying for me. To our collaborators, Deborah Myers, Timo Hofmann, Clemens Heske, Rachid Yazami, Gerald Voecks, Peter Schultz, Arthur Edwards, and Pezhman Srivanian, it was a pleasure working with you all. Thanks to all the companies and agencies who sponsored our research: NSF, DOE, Ford, and MSC sponsors. Lastly, thank you to the Goddard group members for being a source of knowledge and comfort: Yao Sha, Boris Merinov, Shirley Wu, Seung Soon Jang, Adri van Duin, Ho-Cheng Tsai, Wei-Guang Liu, Mu-Jeng Cheng, Hai Xiao, Lianchi Liu, Qi An, Smith Nielsen, Jonathan Mueller, Jamil Tahir-Kheli, Sang Soo Han, and anyone else I might have missed.

Abstract:

The advantages of Proton Exchange Membrane (PEM) fuel cells include lower operating temperature than other fuel cells and size small enough to fit into a car. Improving the cost and durability of PEM fuel cell materials is a hot topic of research today.

The Nafion membrane and cathode catalysts are two areas where PEM fuel cells have issues of cost, durability, and efficiency. In order to improve these materials, researchers need a better understanding of the detailed mechanisms for basic operation and degradation. Computational quantum mechanics has improved in recent years to the point where it can provide accurate potential energy maps of reactions that are difficult to determine by laboratory experiments alone. With the basic understanding of mechanisms, experimentalists can make educated predictions of ways to improve fuel cell materials.

Experimental studies suggest that Nafion degradation is caused by generation of trace radical species (such as $OH^\bullet$, $H^\bullet$) when in the presence of H_2, O_2, and Pt. We use density functional theory (DFT) to construct the potential energy surfaces for various plausible reactions involving intermediates that might be formed when Nafion is exposed to H_2 (or H^+) and O_2 in the presence of the Pt catalyst. We find that $OH^\bullet$ can be generated in trace amounts on the Pt surface from HOOH and OOH_{ad}. Next, we look at various ways in which the $OH^\bullet$ can attack the Nafion sidechains or endgroups on the backbone.

Researchers are looking for ways to replace the Pt cathode catalyst, due to the preciousness of Pt and the low efficiency of the oxygen reduction reaction (ORR) on Pt, among other things. Alloying Pt with non-precious Co greatly increases the ORR efficiency. However, Pt_3Co was reported to not withstand long-cycle testing due to the migration of Co metals onto the catalyst surface and leaching of Co into the electrolyte. To overcome these challenges, we first study Pt_3Co to find out what makes these alloys so special in improving fuel cell efficiency, as well as what causes degradation to occur. Then, we apply the principles we learned in proposing improved fuel cell alloy catalysts.

Table of Contents:

Summary:

This work uses Density Functional Theory (DFT), a quantum-mechanics-based computational method, to tackle difficult challenges facing the commercialization of Proton Exchange Membrane Fuel Cell (PEMFC) today. PEMFC harnesses electricity by using catalysts to convert H_2 and O_2 gas fuel into water electrochemically.

First, we need to understand the fundamental reactions occurring in a PEMFC. The anodic reaction is $H_2 => 2H^+ + 2e^-$. The cathodic reaction is $2H^+ + 2e^- + ½O_2 => H_2O$. It is obvious that the cathodic reaction, or the oxygen reduction reaction (ORR), is multi-step, because an O-O bond needs to be broken and two O-H bonds need to be formed. In the chapter, "Comparison of Density of State of Pure Metals and Their Catalytic Activity using Quantum Mechanics", we look at the detailed mechanism of the ORR for different pure metal catalysts to find out why Pt is the catalyst of choice. While there are many theories in the literature on what happens during the ORR, the popular theories (Norskov and co-workers) depend only on the binding energy of adsorbates and do not include transition states or reactions. We believe the transition states are very important, and we include them in all our work. We also look at the density of states (DOS) for the different metals to evaluate how useful the DOS and values like the d-band center are in predicting catalytic behavior.

Amongst the different overpotentials that cause inefficiencies in a PEMFC (activation, Ohmic, and concentration), the activation overpotential associated with the ORR catalyst is the most severe. Therefore, the efficiency of a PEMFC can be most improved by finding a better cathode catalyst. Remarkable alloy catalysts such as Pt_3Co and Pt_3Ni offer better performance than pure Pt and reduce the amount of precious Pt by 25%. In "Mechanism for the Oxygen Reduction Reaction on Pt_3Co Alloy Fuel Cell Cathodes", we study the detailed reaction mechanism for Pt_3Co to understand how an alloy catalyst can have better reaction rates than pure Pt.

Another overpotential that can be improved is the Ohmic overpotential associated with the conductivity of the Proton Exchange Membrane (PEM). The PEM of choice is Nafion which has great ionic conductivity but has poor durability and high costs. In "The Mechanism for Degradation of Nafion in PEM Fuel Cells from Quantum Mechanics Calculations", we study the detailed mechanism of Nafion degradation to find out how trace OH radicals are formed on the Pt catalyst and how these radicals attack the Nafion chemical structure.

We look deeper into Nafion degradation in the section, "Degradation Mechanism of Nafion Polymer Backbone in PEM Fuel Cell from Quantum Mechanics Calculations". Here, we investigate the how OH radicals attack the Nafion polymer backbone instead of the side chain. There are conflicting experimental results that show where the OH radicals prefer to attack and degrade the Nafion structure (side chain or polymer backbone). We look at reactions between Nafion and OH radicals under different conditions to explain why experimentalists have conflicting results. We find the different degradation experimental conditions lead some experimentalists to believe degradation occurs at the polymer backbone while others believe it occurs at the side chain.

Another possible material cost of PEMFC that can be improved is the expensive Pt catalyst. While non-Pt catalysts such as Pd and Rh are known to be worse than Pt, we explore alloys of Pd and Rh to find alternative catalysts that perform just as well as Pt. In "Improved Non-Pt Alloys for the Oxygen Reduction Reaction at Fuel Cell Cathodes Predicted from Quantum Mechanics", we evaluate surface segregation and other material properties of 75 alloy catalysts and study in further detail our most promising candidate, Pd_3W.

While Pt_3Co is a remarkable ORR catalyst, its commercialization is not possible due to the leaching of Co into the electrolyte under real fuel cell operating conditions. We evaluate the surface segregation of Pt alloys under the effect of adsorbates in "Surface Segregation of Pt Alloys with Adsorbed O and OH Predicted from Quantum Mechanics". We find that when O and

OH are adsorbed on the surface, Pt_3Co favors Co to be on the surface, which will lead to Co leaching. We find other Pt alloys that will be stable when O and OH are adsorbed on the surface.

Another breakthrough in Pt alloy catalysts is the discovery that ternary alloys containing Zr (with Co or Ni) can lead to catalysts with better durability. We explain why the addition of Zr can improve the alloy durability in "Theoretical Study of Zr-Containing Ternary Alloy PEMFC Catalysts with Improved Durability", as well as the role of Co or Ni. Based on the insight from this study, we propose new ternary Pt alloy catalysts that potentially can be more durable than Pt_3Co and more active than pure Pt.

Comparison of Density of State of Pure Metals and their Catalytic Activity using Quantum Mechanics

T.H. Yu[1], T. Hofmann[2], Y. Sha[1] , B.V. Merinov[1], C. Heske[2,3,4], William A. Goddard III[1]

[1]Materials and Process Simulation Center, m/c 139-74 California Institute of Technology,
1200 East California Blvd., Pasadena, CA, 91125, USA

[2]Department of Chemistry, University of Nevada, Las Vegas (UNLV),
4505 S. Maryland Parkway, Las Vegas, NV 89154-4003, USA

[3]Institute for Synchrotron Radiation, Karlsruhe Institute of Technology (KIT)
Hermann-v.-Helmholtz-Platz 1, 76344 Eggenstein-Leopoldshafen, Germany
[4]Institute for Chemical Technology and Polymer Chemistry
Karlsruhe Institute of Technology (KIT)
Engesserstr. 18 / 20, 76128 Karlsruhe, Germany

Abstract

The density of state (DOS) of twelve transition metals (Ag, Au, Co, Cu, Fe, Ir, Ni, Os, Pd, Pt, Rh, Ru) were derived by quantum mechanics calculations. We use the DOS and corresponding band centers to see if there is any correlation with oxygen reduction reaction (ORR) catalytic activity. By looking at ORR reactions, we find trends between binding energy and critical barriers of reactions for this group of metals.

1) For the reaction O_{2ad} => $2O_{ad}$, the reaction barriers decrease as O and OH binding energy is stronger.

2) For the reaction OH_{ad} + H_{ad} => H_2O_{ad}, the reaction barriers increase as O and OH binding energy is stronger.

3) For the reactions O_{ad} + H_{ad} =>OH_{ad} and O_{ad} + H_2O_{ad} => $2OH_{ad}$, there is no clear trend.

The reason there is no trend in reactions that convert Oad to OHad is because the two binding energies are correlated. Trends between binding energy and barrier are only observed when O_{ad} and OH_{ad} are either reactants or products of the reaction but not both. When plotting the binding energy versus the highest reaction barriers, a V-shaped plot is observed with Pt at the bottom indicating the best ORR catalyst. For this diverse group of metals, plotting the d-band center with the critical reaction barriers does not form a V-shaped plot. No correlation was observed when plotting the d-band center with binding energy, in contrast to previous works which found correlation when a narrower subset of catalysts was studied. In order to see if there is correlation between the binding energy and the DOS, we compare the binding of ORR species on the (111) and (100) surface with the corresponding density of state. In this study, there were no clear trend between the changes in binding energy with characteristics in the density of state. Some of the density of states of the same metal with (100) and (111) orientations look nearly identical, even though their binding energies of ORR species are different. Our study of trends in this diverse group of metals found that the binding energy of O and OH correlates well with catalytic activity, and that the binding energy does not correlate well with the d-band center or DOS.

Keywords

Fuel cell, ORR, d-band center, electronic structure, catalysis, DOS

1. Introduction

We examine how the electronic structure of a metal can be used to identify its catalytic activity. For the purpose of facilitating the discovery of new catalysts, scientists often look for useful information from the electronic structure. Photoelectron spectroscopy (PES) has been widely used to provide experimental electronic structure information of metals[1-4]. Many recent works correlated PES results with trends in catalytic activity and found that the weighted mean energy density of the d-band or "d-band center" correlates linearly with binding energy in some cases. The electronic structure derived theoretically from quantum mechanics using density functional theory (DFT) which can be used to screen for potential new catalysts that may offer better performance than current catalysts[5-6]. This is particularly important for the application of polymer electrolyte membrane fuel cells (PEMFCs), where the oxygen reduction reaction (ORR) is sluggish and the present catalyst of choice, Pt, is rare. The d-band centers derived from both theory and experiments have been used to correlate trends in the binding energy of oxygen species and fuel cell activity[1-4,7-8]. In the case of Pt alloys, the plotting of the d-band center of various alloys versus its activity demonstrated a volcano plot, where there is an optimal d-band center corresponding to the peak of the volcano[2-4]. The d-band center at the peak of the volcano plot was explained to be an optimal electronic state where the binding energies of fuel cell ORR species are ideal. Particular reactions in the ORR are rate limiting, and the raising/lowering of the reactant/product energy of the most difficult reaction is desirable.

In some calculations of Pt alloys, this d-band center trends linearly with the binding energy of oxygen species[8], although this is not always the case[9]. The differences in trends may be due to many factors such as the theoretical method, experimental setup, and the way the data is analyzed to derive the d-band center. Fuel cell activity and the density of state correlate better when the comparison is made within a group of similar catalysts (such as the (111) surface of Pt alloys[1-4]). In this type of comparison, all of the catalysts have 100% Pt at the surface in the (111) orientation but are under different "ligand" or "strain" effect[10]. The "ligand" effect entails electronic contribution from subsurface solute atoms, while the "strain" effect entails the effect from compressed/stretched atom-atom distance on catalysis. Since different metals have different bulk structures (HCP, FCC, BCC) and surface orientations (111, 110, 0001), the ground state electronic structures of different pure metal surfaces do not correlate as well to binding trends[5,11-12]. The question remains whether the surface DOS of a metal contains the complete set of information needed to predict surface binding in these cases. To verify this claim, we examine also the case of identical metals with different surface orientations (111 versus 100), to see if the difference between the (111) and (100) surface density of state can explain the very different surface binding trends.

2.2 Computational Methods

Periodic quantum mechanics (QM) calculations were carried out with the SeqQuest code[13-14], which employs Gaussian basis functions at the optimized double zeta plus polarization level rather than the plane-wave basis often used in periodic systems. We used the Perdew-Becke-Ernzerhof (PBE) flavor[15] of density functional theory (DFT) in the generalized gradient approximation (GGA)[16] and allowed the up-spin orbitals to be optimized independently of the down-spin orbitals (spin-unrestricted DFT). All calculations were performed with spin optimization. We used small-core pseudopotentials with angular momentum projections[17-18].

The d-band structures were analyzed with the SeqQuest Post-Analysis Code[14]. The DOS was broadened by convolution with a 0.5 eV FWHM Gaussian function to approximate the experimental and lifetime broadening of the spectra.

3. Results and Discussion

The ORR reaction converts H^+ and O_2 into H_2O. A basic reaction mechanism involves O_2 gas dissociating on the catalyst surface and reacting with either H or H_2O[19] to form OH, and reacting with H again to form H_2O as seen in Figure 1.

We investigate the critical barriers of the ORR reaction as a function of binding energy of O. We see in Figure 2 that the barrier of the O_2 dissociation reaction decreases with the binding energy of atomic O. We also see that the barrier for H_2O formation increases with the binding energy of atomic O. In Figure 3, the barrier for the formation of OH_{ad} is shown. There are two different reactions to form OH from atomic O: direct OH formation[20] and O hydration[19]. In general, the barrier for OH formation from the O hydration mechanism[19] is much lower than OH formation directly. There appears to be no observable correlation with the barriers and the binding energy of O. The reason for the trends is because the atomic O and OH binding energy are highly correlated, as seen in Figure 4. Since the OO dissociation energy involves the formation of O_{ad}, the barrier will decrease as the energy of the product state is lowered. Since HOH formation involves the depletion of $OH_{ad,}$ the barrier will increase as the reactant state is lowered. In reactions where O_{ad} is the reactant and OH_{ad} is the product, there is no trend with the binding energy since both the reactant and product states are changed simultaneously. A previous work by Adzic[7] observed linear trends with the calculated OO dissociation barrier and OH formation barrier with atomic O binding energy. This trend was found amongst a specific group of catalysts with Pt monolayers on different metal substrates. We see that for the case of different pure metals, the OH formation barrier does not increase with oxygen binding.

In Table 1, we show our calculated band centers that are derived from the DOS shown in Figure 6. The surface d-band centers are compared with theoretical results from literature, and there is better agreement with work of Gajdos[12] with average absolute difference of 0.13 eV, while the agreement with Ruban[5] is worse with average absolute difference of 0.54 eV. We observe that the surface DOS has larger density near the Fermi level than the bulk DOS. This is especially true when comparing the surface and bulk DOS of the FCC atoms (Ni, Cu, Rh, Pd, Ag, Ir, Pt, Au), and a larger peak is evident near the Fermi level. The larger peak makes the surface band centers closer to the Fermi energy than the bulk band centers. The comparison of the density of state with experiments is published in parallel to an experimental work[21]. The experimental d-band centers differ partly due to the hybrid nature of experimental DOS, where it contains contribution from both surface and bulk DOS. Even when theoretical d-band centers are compared with experiments that measure only the surface DOS contributions, there are absolute differences of that are not insignificant[1].

Figure 7 shows the correlation between the different metal band centers and their atomic oxygen binding. When conducting a linear fit for the different calculated band centers, the bulk "d" electron band center fits the best with a R^2 value of 0.619, while the R^2 for bulk total, "d" surface, and bulk surface are: 0.595, 0.427, and 0.427, respectively.   A 0.619 R^2 value is still inadequate and shows that having a variety of metals does not show a good linear fit with the d-band center. In contrast, when this comparison was made with the same (111) Pt surface but different solute metals in the subsurface[8,22] or Pt with different Pt-Pt distances[9], the d-band theory fits better. It is noteworthy that this comparison of d-band center with atomic O binding energy has not been made previously in literature for a variety of pure metals. One has to make the comparison directly[5,11] with different articles by the same authors to see that there is poor linear fitting between these two values when the sample is a variety of pure metals.

Although this study found the surface d-band center to be an inadequate indicator for atomic oxygen binding for different pure metals, the question remains whether the DOS of a metal contains the information that correlates to its binding energy. The difficulty with evaluating the DOS of a catalyst and how it relates to activity is that there are so many different peak characteristics in a DOS. This is why the d-band center has become a useful value, because it lumps the entire DOS into a single value. To better understand the contributions of the DOS to binding, we compare (100) and (111) DOS of the same pure metal as seen in Figure 8. We see that the DOS is quite similar, and there are some cases (Ag and Pd in particular), where they are hard to distinguish to the naked eye. We tabulate the binding energy of O and OH in Table 2. Upon in-depth evaluation of the (100) and (111) DOS, we cannot see a clear trend in it that would explain the larger binding energy on the (100) surface versus the (111) surface.

In Table 2, we evaluate other catalyst characteristics to see if they can properly predict the larger binding on the (100) surface. We look again at the d-band center and see that it is smaller in value for all of the metals except two cases. The d-band theory[5,8] predicts that the binding energy increases as the d-band center decreases. In this evaluation, we see that the d-band center work for all cases except Ag and Au. We evaluate the electronic work function as well and see that it does predict the larger binding energy on the (100) surface, as all of the work function values are smaller on the (100) than for the (111) surface. This makes sense as the more weakly bound electrons on the (100) surface will be easier for the electronegative O and OH to bind with. Therefore, in this exercise, we find that the electronic work function properly predicts the larger binding energy on the (100) surface versus (111) surface.

4. Conclusion

In summary, this work evaluated the barriers of reactions for the ORR and compared the critical barrier versus the binding energy of O and OH. We find that the critical barrier of Pt is the lowest and there is a V-shaped plot when plotting the twelve metals with Pt at the center. The reason some of the metals (Ag, Au) have a higher barrier than Pt is because the OO dissociation barrier is higher, while the other metals (Pd, Ir, Cu, Rh, Ni, Ru, Co, Os) have a higher barrier than Pt because the H_2O formation barrier is higher. We explained that the binding energy of Pt with O and OH is at an ideal intermediate position where all of the barriers are low. Looking at values of the density of state and trends with the critical barriers, we did not find any clear trend when comparing this large set of pure metals. Although previous works found trends between the d-band center and activity in a specific group of similar catalysts, the d-band center theory does not fit well when different pure metals are compared. To look deeper, we examined the density of states of the pure metals to see if there are any characteristics that relate it to binding energy. We find that, when comparing pure metals of different orientations, the DOS look almost identical and there is no clear distinguishing factor that would explain the very different binding energies between the (100) and (111) surface. While the d-band center model works well in specific cases, neither this work nor any work to date have shown that this model works for a large group of pure metals.

Table 1: Comparison of the band centers derived from DOS with those in literature. The TDOS contains all s, p, and d electronic contributions, while the d-sum is just the d. The bulk is the result of three-dimensional crystal calculations. The surface is the topmost layer of the most favorable surface and derived from slab calculations. The surface d-sum results agree better with the work of Gajdos[12] (with an average absolute difference of 0.13 eV) than with the work of Ruban[5] (0.54 eV).

Element	Current Work				Reference	
	Surface		Bulk			
	TDOS	d-sum	TDOS	d-sum	Theory	Exp.
Fe	2.34	2.16	2.14	1.88	0.92[5]	1.55[21]
Co	2.10	1.89	2.54	2.16	1.17[5], 2.0[12]	1.54[21]
Ni	2.24	2.03	2.35	2.09	1.29[5], 1.48[6], 1.7[12]	1.20[21]
Cu	2.64	2.51	3.02	2.83	2.4[12], 2.67[5-6]	3.05[21]
Ru	2.69	2.63	3.04	2.85	1.41[5], 2.7[12]	
Rh	2.54	2.45	3.00	2.86	1.73[5], 2.3[12]	
Pd	2.13	2.03	2.44	2.30	1.8[12], 1.83[5]	2.09[21]
Ag	3.97	4.07	4.31	4.37	4.0[12], 4.30[5]	5.28[21]
Os	3.21	3.07	3.89	3.55		
Ir	3.11	3.29	4.00	3.75	2.11[5], 2.9[12]	
Pt	2.79	2.60	3.38	3.13	2.25[5], 2.4[12], 2.75[6]	2.36[23], 2.54[1], 2.94[21],

						4.77[24]
Au	3.53	3.47	4.06	3.94	3.5[12], 3.56[5], 3.91[6]	4.45[21]

Table 2: Comparison of the binding energy of O and OH on (111) versus (100) surface. The number in bold is the larger binding energy. We compare the difference in binding energy with properties of the catalyst surface. We see that in general, the binding energy increases as the surface changes from (111) to (100). This is correctly predicted by the d-band center model in the surfaces studied, except for Au and Ag (bold indicates a smaller d-band center, which corresponds to larger binding energy). The electronic work function appears to be a better predictor of binding energy trends, as the smaller electronic work function of the (100) surface makes the binding of electronegative O and OH much stronger.

	O Binding (eV)		**OH Binding (eV)**		**Surface d-band Center (eV)**		**Electronic Work Function (eV)**	
	(111)	(100)	(111)	(100)	(111)	(100)	(111)	(100)
Ni	4.85	**5.23**	3.18	**3.50**	2.03	**1.68**	4.86	**4.66**
Cu	4.18	**4.51**	2.85	**3.15**	2.51	**2.42**	4.74	**4.32**
Rh	**4.49**	4.39	2.92	**3.12**	2.45	**2.23**	5.07	**4.86**
Pd	3.78	**3.84**	2.53	**2.69**	2.03	**1.94**	5.08	**4.89**
Ag	3.04	**3.62**	2.35	**2.74**	**4.07**	4.10	4.4	**4.01**
Ir	**4.28**	4.18	2.74	**2.96**	3.29	**2.77**	5.39	**5.33**
Pt	3.22	**3.80**	2.38	**2.87**	2.60	**2.50**	5.8	**5.59**
Au	2.42	**2.56**	1.81	**2.20**	**3.47**	3.57	5.27	**4.88**

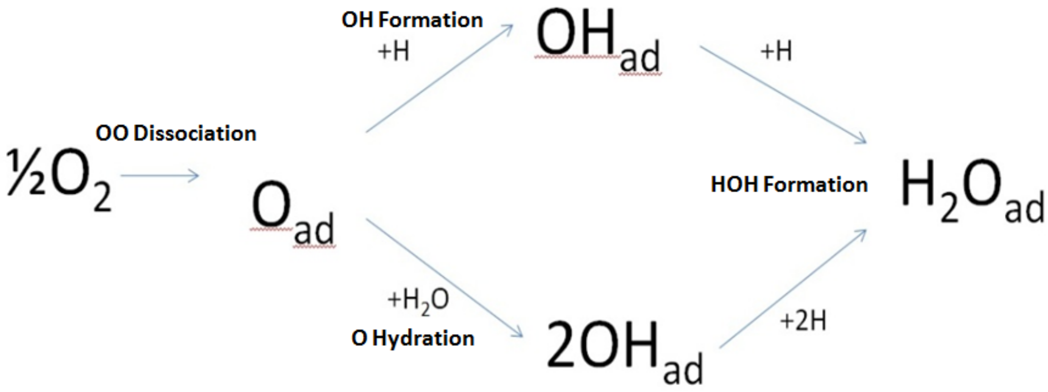

Figure 1: ORR Reaction mechanism. O_2 dissociates to form atomic O. The O reacts with either H or H_2O to form OH. OH reacts with H to form H_2O.

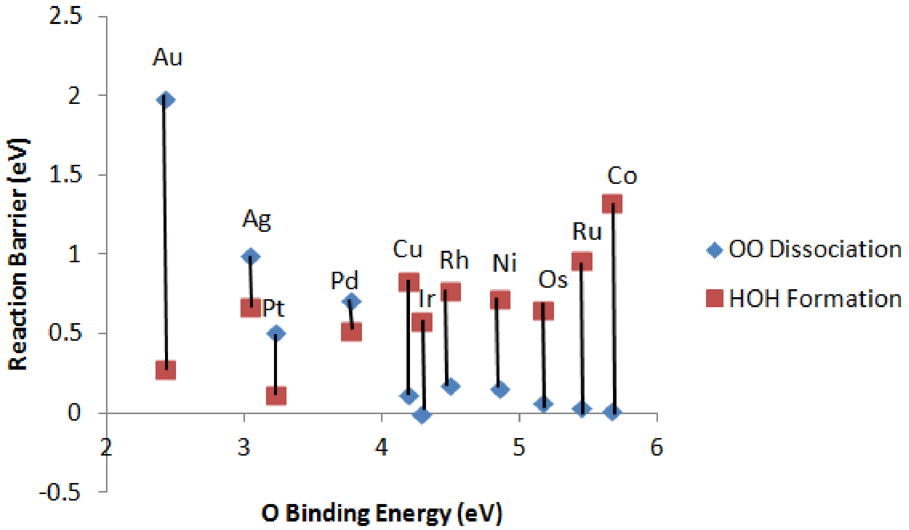

Figure 2: Barrier of OO dissociation (OO_{ad} => $2O_{ad}$) and HOH formation (OH_{ad} + H_{ad} => HOH_{ad}) as a function of atomic O binding energy. It is observed that that O2 dissociation barrier decreases as binding energy is stronger and HOH formation barrier increases as binding energy increases.

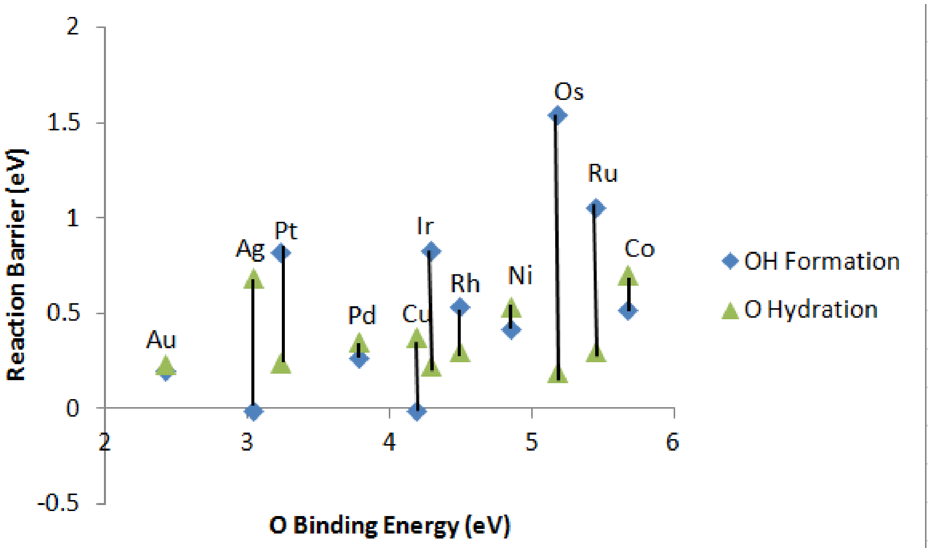

Figure 3: Barrier of OH formation (O_{ad} + H_{ad} => OH_{ad}) and O Hydration (O_{ad} + HOH_{ad} => $2OH_{ad}$) as a function of atomic O binding energy. The reaction barriers are not observed to be correlated with the binding energy.

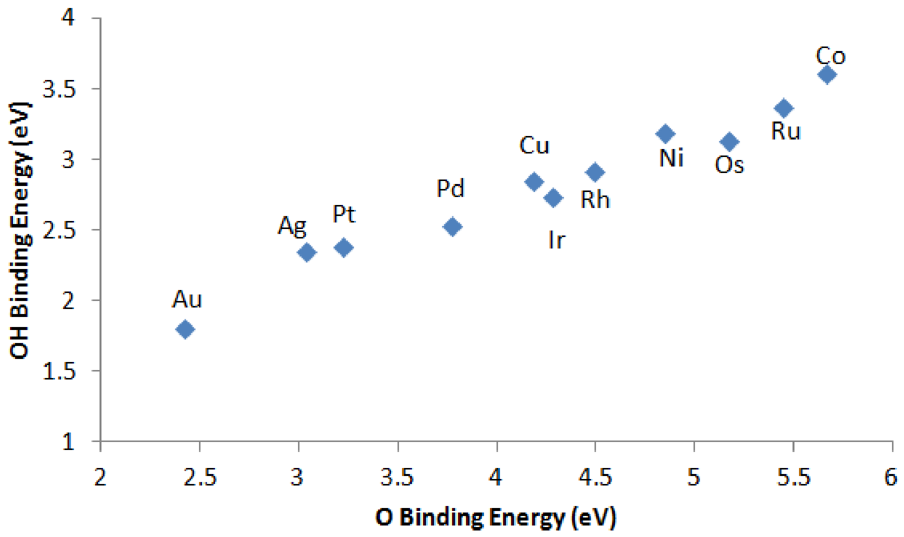

Figure 4: Plot of the binding energy of atomic O with OH. We see that the two binding energies are highly correlated.

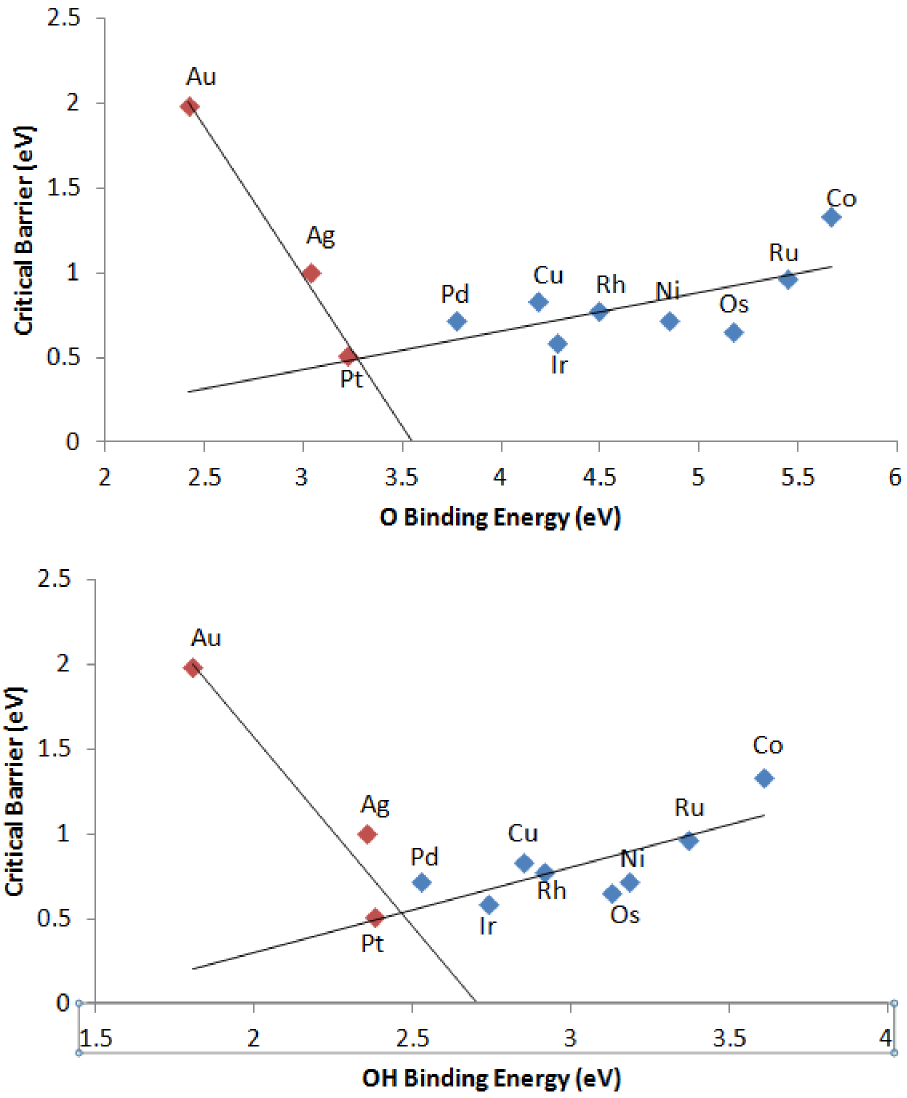

Figure 5: Plot of the O and OH binding energy with the rate-determining barrier of the ORR from the mechanism shown in Figure 1, with Pt showing the overall barrier. As the binding energy decreases, the barrier for the OO dissociation increases as in the case of Ag and Au. As the binding energy increases, the barrier for the HOH formation increases, as in the case of Co and Ru. The reason the HOH formation barrier increases with O binding energy is because O and OH binding are correlated. A stronger OH binding means OH + H => HOH is more difficult.

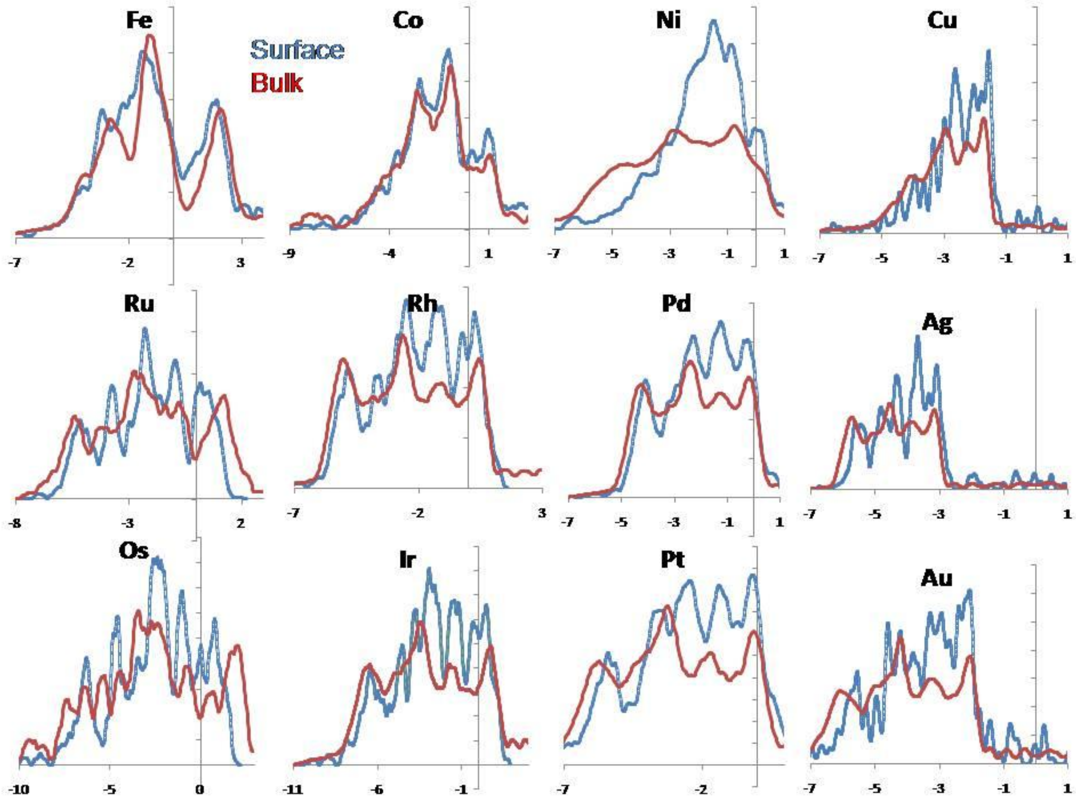

Figure 6: Total DOS of pure metals. The bulk bands show the total DOS for the metal with its bulk crystal structure (BCC - Fe; HCP - Co, Ru, Os; FCC - Ni, Cu, Rh, Pd, Ag, Ir, Pt, Au). The surface bands show the total DOS for top layer of the favorable surface orientation (110 - Fe; 0001 - Co, Ru, Os; 111 - Ni, Cu, Rh, Pd, Ag, Ir, Pt, Au).

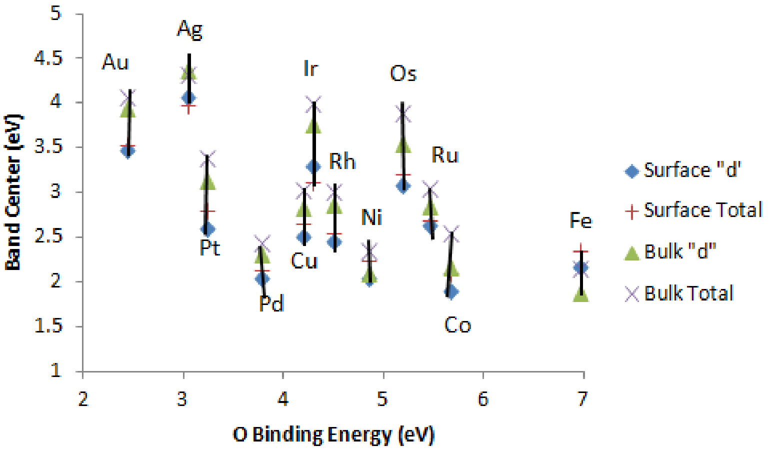

Figure 7: Trending the oxygen binding energy of twelve metals versus their band centers. For the extreme cases of Fe and Ag, we see a correlation between binding energy and band center. For most of the metals, there is no clear trend between binding and band centers.

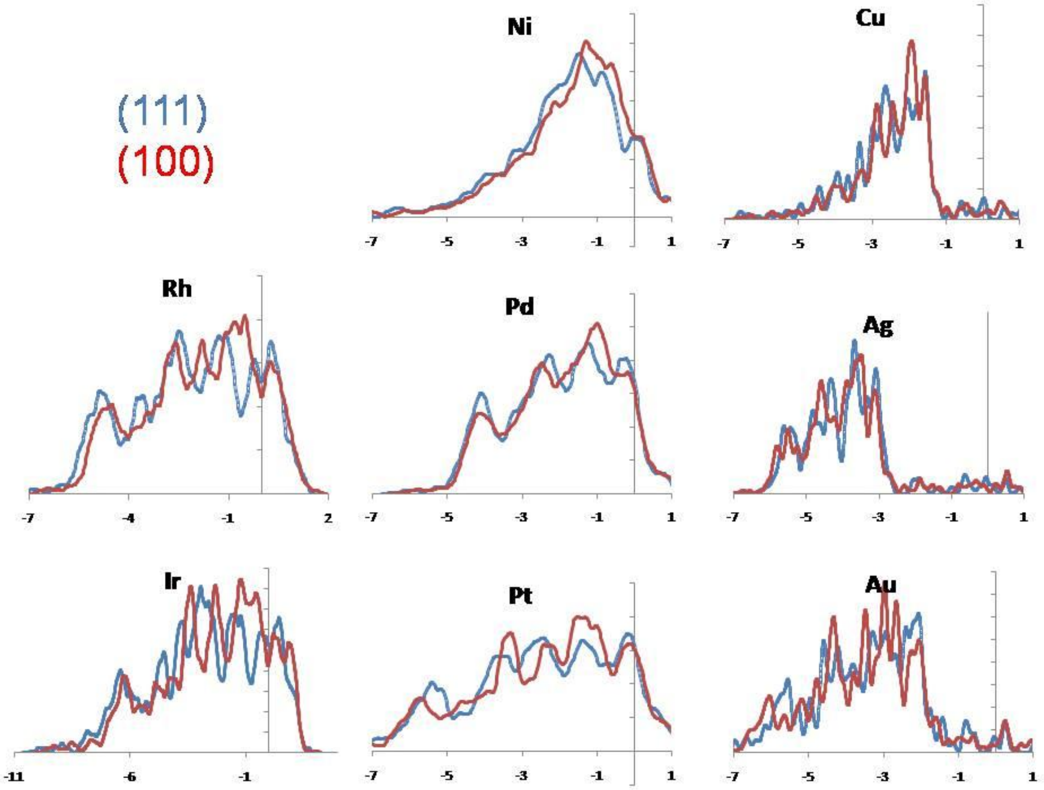

Figure 8: Comparison of (111) and (100) DOS for different pure metals. The differences are hard to distinguish. There is no distinct observable quality to the DOS that can pinpoint the larger binding energy of the (100) surface when compared to the (111) surface.

(1) Mun, B. S.; Watanabe, M.; Rossi, M.; Stamenkovic, V.; Markovic, N. M.; Ross, P. N. *J Chem Phys* **2005**, *123*.

(2) Norskov, J. K.; Stamenkovic, V.; Mun, B. S.; Mayrhofer, K. J. J.; Ross, P. N.; Markovic, N. M.; Rossmeisl, J.; Greeley, J. *Angew Chem Int Edit* **2006**, *45*, 2897.

(3) Stamenkovic, V. R.; Mun, B. S.; Arenz, M.; Mayrhofer, K. J. J.; Lucas, C. A.; Wang, G. F.; Ross, P. N.; Markovic, N. M. *Nat Mater* **2007**, *6*, 241.

(4) Stamenkovic, V. R.; Mun, B. S.; Mayrhofer, K. J. J.; Ross, P. N.; Markovic, N. M. *J Am Chem Soc* **2006**, *128*, 8813.

(5) Ruban, A.; Hammer, B.; Stoltze, P.; Skriver, H. L.; Norskov, J. K. *J Mol Catal Chem* **1997**, *115*, 421.

(6) Hammer, B.; Norskov, J. K. *Surf Sci* **1995**, *343*, 211.

(7) Zhang, J.; Vukmirovic, M. B.; Ye, X.; Mavrikakis, M.; Adzic, R. R. *Angew Chem Int Edit* **2005**, *44*, 2132.

(8) Menning, C. A.; Hwu, H. H.; Chen, J. G. G. *J Phys Chem B* **2006**, *110*, 15471.

(9) Hyman, M. P.; Medlin, J. W. *J Phys Chem C* **2007**, *111*, 17052.

(10) Schlapka, A.; Lischka, M.; Gross, A.; Kasberger, U.; Jakob, P. *Phys Rev Lett* **2003**, *91*.

(11) Norskov, J. K.; Rossmeisl, J.; Logadottir, A.; Lindqvist, L.; Kitchin, J. R.; Bligaard, T.; Jonsson, H. *J Phys Chem B* **2004**, *108*, 17886.

(12) Gajdos, M.; Eichler, A.; Hafner, J. *J Phys-Condens Mat* **2004**, *16*, 1141.

(13) Schultz, P. SEQQUEST, Sandia National Laboratory.

(14) Edwards, A. SEQQUEST Post Analysis Code.

(15) Perdew, J. P.; Burke, K.; Ernzerhof, M. *Phys Rev Lett* **1996**, *77*, 3865.

(16) Perdew, J. P.; Zunger, A. *Phys Rev B* **1981**, *23*, 5048.

(17) Melius, C. F.; Goddard, W. A. *Phys Rev A* **1974**, *10*, 1528.

(18) Goddard, W. A. *Phys Rev* **1968**, *174*, 659.

(19) Sha, Y.; Yu, T. H.; Merinov, B.; Shirvanian, P.; Goddard, W. A. *J Phys Chem Lett* **2011**, *2*, 572.

(20) Jacob, T.; Goddard, W. A. *Chemphyschem* **2006**, *7*, 992.

(21) Hofmann, T.; Yu, T. H.; Folse, M.; Weinhardt, L.; Bar, M.; Zhang, Y.; Merinov, B. V.; Myers, D. J.; Goddard, W. A.; Heske, C. *In Press* **2012**.

(22) Kitchin, J. R.; Norskov, J. K.; Barteau, M. A.; Chen, J. G. *J Chem Phys* **2004**, *120*, 10240.

(23) Ross, P. N.; Markovic, N. M. **2004**.

(24) Hwang, S. J.; Yoo, S. J.; Jang, S.; Lim, T. H.; Hong, S. A.; Kim, S. K. *J Phys Chem C* **2011**, *115*, 2483.

Mechanism for the Oxygen Reduction Reaction on Pt_3Co Alloy Fuel Cell cathodes

Ted H. Yu†, Yao Sha†, Boris V. Merinov†, Pezhman Shirvanian§ and William A. Goddard III†*

†Materials and Process Simulation Center, MC 139-74,

California Institute of Technology, Pasadena, California 91125

§Ford Motor Co., Research & Advanced Engineering

2101 Village Rd, Dearborn, Michigan 48104

1200 E California Blvd MC 139-74, Pasadena, CA 91125

Phone: +1 626 395 2731 FAX +1 626 585 0918

* Email: wag@wag.caltech.edu

ABSTRACT: We use quantum mechanics (QM) (density functional theory (DFT) at the PBE level) to predict the binding-site preferences and reaction barriers for all intermediates involved in the oxygen reduction reaction (ORR) on the low-energy surface of Pt_3Co alloy. Here we calculate that the surface layer is Co depleted (100% Pt) while the 2nd layer is Co enriched (50% Pt) as shown by experiment. Even though the top layer is pure Pt, we find that the sublayer Co imposes strong preferences in binding sites for most intermediates, which in turn strongly influences the reaction barriers. This strong preference leads to a strong site dependence of the barriers. Considering water as the solvent, we predict that at low coverage (of O and OH), the barrier of the rate-determining step (RDS) is 1.03eV, whereas at high coverage, this barrier decreases to 0.48eV. This can be compared to a barrier of 0.50 for pure Pt, explaining the improved rate for the alloy. We report the results both for gas phase and for aqueous phase environments.

KEYWORDS: ORR, Pt_3Co alloy catalyst, PEMFC, DFT, PBE, reaction mechanism

1.0 Introduction

The efficiency of the oxygen reduction reaction (ORR) ($4H^+ + 4$ e- $+ O_2 \rightarrow 2 H_2O$) at the cathode of proton exchange membrane (PEM) fuel cells (PEMFC) is a critical issue for commercial application of PEMFC in automobiles[1-4]. The best current catalysts are Pt and Pt-based binary alloys, including Pt_3Co[5,6] and[7] Pt_3Ni[8]. Several different hypotheses have been put forward for the improved ORR activity of these alloys, including the shift in the d-band[6] or a decrease in the surface lattice parameter to values optimal for ORR[9]. It has been argued that that the alloy makes OH removal favorable, increasing the surface area available for O_2 binding[8]. Another proposed theory explains that the critical step in the ORR involves O_{ad} as a reactant, and the lower binding energy of O_{ad} for Pt alloys[10] will make reactions involving O_{ad} easier and increase ORR rates.

A somewhat unique property of Pt_3Co and Pt_3Ni is the surface segregation observed experimentally from quantitative analysis of LEED experiments[11]. Our quantum mechanics (QM) (density functional theory (DFT) at the PBE level) calculations using finite slabs find the same segregation of the Pt_3Co alloy into a structure with 100% percent Pt on the surface layer, 50% on the 2nd layer, and 75% for deeper layers[12]. We consider that this strong segregation to form a pure Pt surface layer (analogous to a core-shell system) may be important in ensuring a long lifetime for these catalysts.

Starting with this segregated surface of Pt_3Co alloy, we use QM to predict the binding-site preferences and reaction barriers for all intermediates involved in the oxygen reduction reaction (ORR). This leads to a new detailed, atomistic-level chemical mechanism explaining the increased reactivity on Pt_3Co alloys. In particular, we find that subsurface Co influence the ORR kinetics on the surface even though the surface is 100% Pt.

2.0 Methodology

We model the Pt_3Co alloy as a two-dimensionally infinite periodic slab with four atoms per cell and six layers of atoms. We consider the atomic Pt composition as 100-50-75-75-75-75, as observed experimentally[13] and calculated theoretically[12]. All calculations used the Perdew-Becke-Ernzehof (PBE) functional of DFT. We used small core Norm-conserving angular momentum projected pseudopotentials[14-17] in which the 3p, 3d and 4s electrons of Co and the 5p, 5d, 6s electrons on the Pt are treated explicitly with 15 electrons for neutral Co and 16 for Pt. We used optimized double zeta plus polarization quality Gaussian-type orbitals on the Pt and Co with the SeqQuest software[18]. To represent the effects of solvent polarization, we use the implicit model developed earlier[19]. The periodic cell parameters of the slab are based on the optimized Pt_3Co bulk structure.

3 Binding sites

3.1 Notation

First, we studied the preference of H, O, OH, H_2O, O_2, and OOH on the various binding sites shown in Figure 1. Generally a closest packed (111) surface of fcc structured metals has four types of sites:

- On top, bonded to one Pt (μ_1), denoted as t;
- Bridging between two Pt (μ_2), denoted as b;
- Bridging between three Pt (μ_3) but in the fcc position (not above atoms of the top or 2nd layer), denoted as f;
- Bridging between three Pt (μ_3) but in the hcp position (above atoms of the 2nd layer), denoted as h.

However for the Pt_3Co surface, we need to take into account that the second layer is 50% Co and 50% Pt, while the third layer is 25% Co. We find that the binding energies to the pure Pt layer depend strongly on the nature of the 2nd-layer atoms. The various cases are tabulated in Figure 1. See

Figure 2 for details of the difference between sites.

Considering only the 1st and 2nd layers, we have two types of top sites: t_1 with one Co neighbor in the 2nd layer and t_2 with two. Considering also the 3rd layer, we can distinguish t_{1a} with no Co in the 3rd layer directly beneath the surface and t_{1b} with one. All t_2 sites are the same, even considering the 3rd layer Co, as shown in

Figure 2. .

Considering just the top two layers there are four μ_2 bridge sites, depending on the number of Co atoms underneath: b_0, b_1, b_2, and b_3 with 0, 1, 2 and 3 Co atoms in the 2nd layer. Considering also the 3rd layer, there are two subtypes for b_1, b_2, and b_3 depending on the distance to the Co in the 3rd layer. We denote the subtypes closer to the 3rd layer Co as b_{1a}, b_{2a}, b_{3a} and the others as b_{1b}, b_{2b}, b_{3b}, respectively. The b_0, b_{1a}, b_{1b}, b_{2a}, b_{2b}, b_{3a} and b_{3b} sites are shown in

Figure 2.

Considering just the top two layers, there are two fcc sites: f_1 and f_2 with one and two Co atoms in the sublayer triangle; also considering the 3rd layer, f_1 splits into f_{1a} and f_{1b}, with f_{1a} on top of the 3rd layer Co and the f_{1b} on top of the 3rd layer Pt.

Similarly, for just the top two layers there are two hcp sites: h_1 and h_2. Here h_1 is on top of the sublayer Co while h_0 is on top of the sublayer Pt. Considering the 3rd layer, the h_1 splits into h_{1a} and h_{1b}, with one and zero Co atoms in the projected triangle of 3rd layer atoms, as shown in

Figure 2.

3.2 Binding of H

As shown in Table 2, the preferred binding sites for H on the Pt_3Co surface are t_{1b} with a binding energy of 2.74eV, followed by t_{1a}, and b_0 with binding energy of 2.60eV without solvation. On the other hand, the b_{3a}, b_{3b}, and t_2 sites in the purple region have binding energy of 2.29-2.43eV without solvation, making them higher than the preferred binding site by 0.31eV without solvation.

As shown in Table 2, with solvation the preferred sites become t_{1b}, t_{1a}, and b_{1a}, with binding energies ranging from 2.79-2.83eV, followed by f_{1b}, h_{1b}, b_{1b}, f_2, b_0, h_{1a}, b_{2a}, h_2, and b_{2b}, with binding energies ranging from 2.57-2.75eV. This favorable region of H is colored orange in Figure 1. The barrier for migration of H within the orange region is small. The b_{3a}, b_{3b}, and t_2 sites in the purple region have binding energies of 2.39-2.47eV with solvation, making them higher than the preferred binding site by 0.32eV.

Consequently the blue region serves as a barrier region preventing hydrogen from diffusing between different orange stripes. For the pure Pt surface, the binding energies of H are 2.74eV without solvation and 2.83eV with solvation, with no such forbidden region, allowing H to migrate easily in all directions to react with other species.

3.3 Binding of O atom

On pure Pt, O_{ad} binds strongly to the fcc site, with a net bonding energy of 3.66eV without solvation and 4.36eV with solvation. For Pt_3Co, the binding energy for O_{ad} depends dramatically on the site. f_2 is preferred with a binding energy of 3.56eV followed by $f_{1a,}$ with 3.27eV gas phase. With solvent, f_2 and f_{1b} becomes the two dominant binding sites with binding energy of 4.63eV and 4.40eV. All other binding sites are at least 0.60eV less stable than f_2. This strong stabilization of f_2 arises because the two electropositive Co in the 2nd layer underneath makes this site more electron rich when compared to the f_{1a} and f_{1b} sites which sits over just one Co. Bonding with electronegative oxygen is enhanced over an electron rich site.

The next best sites in gas phase are b_0, f_{1b}, and h_{1a}. With solvation, all other sites are weaker than f_2 by at least 0.6eV. All the other sites have small barriers to fall into the f_2 site (except at extremely high coverage), with b_{1a}, b_{1b}, and b_{2b} sites being unstable.

The binding energy for the fcc site on pure Pt surface is 0.10eV stronger without solvation but 0.27 eV weaker with solvation than f_2. These results indicate that dissociation of O_2 strongly prefers to give O_{ad} at the f_2 site, with no migration to other sites.

3.4 Binding of OH

On pure Pt, OH has almost the same binding energy on all sites, with a binding energy of 2.22eV-2.28eV without solvation and 2.57-2.77eV with solvation.

For Pt_3Co, the best site without solvation is h_2 with a binding energy of 2.86eV. Here the OH bond tilts toward f_2, t_{1a}, t_{1b}, $b_{1a,}$ b_0 and b_{1b}. They are less stable than h_2 by 00.05, 0.06, 0.06, 0.09, and 0.15eV without solvation. With solvation, t_{1a} is the most preferred site with binding energy of 3.31eV, followed by f_2, t_{1b}, and h_2, with binding energy of 3.19-3.29eV. As comparison, OH binds much weaker to t_2, b_{3a} and b_{3b} with binding energy of 3.01-3.11eV. Hence OH selectively binds to the orange region, just as does H. OH_{ad} at other binding sites has a strong preference to migrate to this preferred region. This differs dramatically from the case of the Pt surface where the binding energies of OH range over 0.10eV without solvation and 0.06 eV with solvation, indicating that it can migrate easily.

3.5 Binding of O_2

For pure Pt, we find a binding energy of 0.46eV without solvation and 0.87eV with solvation, with a range of just 0.19 and 0.17 eV for various sites for gas phase and solution phase, respectively.

For the Pt_3Co surface O_2 binds most strongly (0.76 eV without solvation and 0.93eV with solution) to b_0. All other sites are higher by at least 0.14eV. Thus O_2 has a small preferred binding region b_0 Pt_3Co that is in the orange regions where H_{ad} binding is favorable. This gives a favorable migration pathway for formation of OOH

3.6 Binding of OOH

For pure Pt, OOH binds to the top sites with the terminal O bonded to the Pt and the OOH plane parallel to the surface. OOH prefers to have the OO bond heading to an adjacent Pt atom, leading to a binding energy of 1.06eV without solvation and 1.52eV with solvation.

For Pt_3Co, we find that t_{1b} is quite favorable, with binding energies of 1.13eV in gas phase and 1.60eV with solvation. Here the preferred orientation for the OO bond is also toward the adjacent Pt atom, similar to Pt (t sites), as opposed to f sites where the terminal O points toward an FCC site.

All other sites cannot bind OOH, leading instead to dissociation, so that once formed, OOH cannot migrate on the surface.

3.7 Binding of H_2O

H_2O binds only to top sites, but it does not have strong preference between different sites, with binding energies of 0.26-0.35eV in gas phase and 0.64-0.75eV with solvation, compared to 0.22 and 0.58eV on Pt. Comparing with the 0.40eV solvent stabilization of bulk H_2O, H_2O shows positive binding to both surfaces.

However H_2O does not bind to bridge, fcc, or hcp sites. Thus migration of H_2O from one top site to the next is through adsorption and dissociation. Hence the migration barrier is 0.35eV in gas phase and 0.35eV in solvation (0.75eV binding energy minus the 0.40eV solvation of H_2O).

3.8 Binding of H_2O_2

H_2O_2 has a binding energy on Pt_3Co of 0.28-0.49eV without solvation and 0.64-0.86eV with solvation, higher than the the 0.27 and 0.61eV on Pt.

3.9 Summary

As shown in Table 1 and Table 2, we find that O_2 prefers b_0, placing it close to $f_{2,}$ the only site preferred by O. H prefers to move within in the orange region, allowing it to attack O at the f_2 site to form OH at the t_{1a} or t_{1b} site.

OH can also move along b_0, t_{1a}, t_{1b}, f_2, and h_2.

OOH prefers top sites with the second O orienting near Pt.

H_2O prefers all top sites and H_2O_2 prefers bridge sites.

We see that there is a strong regional preference for O_2, O, H, OH, and OOH to remain in the orange stripes. Of the top sites, t_{1a} and t_{1b} are most preferred for all species. Similarly, b_0 or b_{1a} is predominantly preferred among bridge sites. As for three-fold binding sites (fcc and hcp, f_{1a}, f_{1b}, f_2, h_{1a}, h_{1b}, h_2), f_2 is strongly preferred. So when the surface is exposed to all the intermediates, at lower coverage (quarter layer), sites b_0, f_2, and t_{1a} (also t_{1b}) are preferred. Only at higher coverage will the adsorbates bind to other sites.

The big picture is that the chemistry prefers the orange region in Fig 1. The direct effect of this is that reaction barriers depend on whether the starting and ending sites are inside the preferred region.

4.0 Reaction barriers and possible mechanisms

Our previous studies showed that six fundamental steps are involved in the various possible mechanisms, namely,

a) O_2 dissociation: $O_{2a} \Rightarrow O_a + O_a$,

b) OH formation: $O_a + H_a \Rightarrow OH_a$,

c) H_2O formation: $OH_a + H_a \Rightarrow H_2O_a$,

d) OOH formation: $O_{2a} + H_a \Rightarrow HOO_a$,

e) OOH dissociation: $HOO_a \Rightarrow OH_a + O_a$,

f) hydration: $O_a + H_2O_a \Rightarrow OH_a + O_a$.

In putting these fundamental steps into an overall mechanism we distinguish three categories.

- **OO bond activation.** There are two mechanisms: O_2 dissociation (a) and OOH formation (d) followed by OOH dissociation (e).
- **OH formation**. There are two mechanisms: OH formation (b) and O hydration (f).
- **OH consumption**. There is one mechanism: H_2O formation (c).

A good catalyst must provide a low barrier in each of these three categories and a pathway for connecting them.

Starting from the preferred sites, we calculated the barriers for all six steps on Pt_3Co. The barriers with and without solvation and the comparison with pure Pt are shown in

Table 3 and Table 4.

4.1. Gas phase barriers at low coverage

OO bond activation: On Pt_3Co, the mechanism of OOH formation followed by OOH dissociation leads to a barrier of 0.26eV, compared to 1.08eV for the direct dissociation. This is similar to the case of Pt, where OOH formation has a barrier of 0.28 compared to 0.58eV for direct dissociation.

OH formation: On Pt_3Co, O hydration has a barrier of 0.47eV, compared with 0.70eV for the direct OH formation. This preference for O hydration is similar to the case of Pt where the O hydration barrier is 0.29eV, compared to 0.72eV for the direct OH formation.

OH consumption: On Pt_3Co, H_2O formation has a small barrier of 0.23eV, and is higher than the barrier for the Pt case.

Summarizing the three steps, we have the following preferred mechanism (denoted **OOH-form-hydr-gas)** for both Pt_3Co and Pt.

$O_2 + H \rightarrow OOH$ (E_a = 0.20eV for Pt_3Co and 0.28eV for Pt),

$OOH \rightarrow O + OH$ (E_a = 0.264eV for Pt_3Co and 0.14eV for Pt),

$O + H_2O \rightarrow 2OH$ (E_a = 0.47eV for Pt_3Co and 0.29eV for Pt),

$OH + H \rightarrow H_2O$ (E_a = 0.23eV for Pt_3Co and 0.11eV for Pt).

Figure 3 shows the potential energy surface of this preferred mechanism on both Pt and Pt_3Co surface. The RDS for this mechanism is O hydration with a barrier of 0.47eV for Pt_3Co. For Pt, the RDS is OOH formation with a barrier of 0.29eV. Hence for the gas phase, Pt out performs Pt_3Co.

4.2 Solution phase barriers at low coverage

OO bond activation: The best O_2 dissociation pathway starts from an b_0-bound O_2 and dissociates to form two O_{ad} at f_2 sites, with a barrier of 0.07eV (because solvent strongly favors dissociation), similar to that on Pt surface. On Pt_3Co, we find that OOH formation has a barrier of 0.12eV similar to the 0.19eV on Pt. OOH dissociation on Pt_3Co has a barrier of 0.18eV. Thus OOH formation and dissociation is not the favored pathway for the solvated system.

OH formation: For the second step, Pt_3Co has a direct OH formation barrier of 1.20eV, 0.11eV higherer than the 1.09eV on Pt. The O hydration step is less favorable on Pt_3Co, leading to a barrier of 01.03eV, compared with 0.50eV for Pt. As illustrated in our previous paper [20], O hydration is the dominant mechanism for forming OH on Pt. Hence O hydration is the preferred mechanism for both Pt_3Co and Pt with barrier of 1.03eV and 0.50eV. This suggests that P_3Co would have worse performance for formation of OH_{ad}.

OH consumption: For the consumption of OH, water formation on Pt_3Co (0.41eV barrier) is worse than for Pt (0.17eV barrier).

Summarizing these three steps lead to the **O_2-diss-hydr-low** mechanism:

$O_2 \Rightarrow 2O$ ($E_a = 0.07$ for Pt_3Co and 0.00 for Pt),

$O + H_2O \Rightarrow 2OH$ ($E_a = 1.03$eV for Pt_3Co and 0.50eV for Pt),

$OH + H \Rightarrow H_2O$ ($E_a = 0.41$eV for Pt_3Co and 0.11eV for Pt).

Figure 4 shows the potential energy surface of O_2-diss-hydr-low mechanism with solvent effect at different coverage. In solution O hydration is the RDS for both Pt_3Co and Pt, quite different than for gas phase. Hence the overall barrier becomes 1.03eV for Pt_3Co and 0.50eV for Pt. Thus, our results would suggest that Pt_3Co would not outperform Pt, which does not agree with the experimental result[8] that Pt_3Co is more efficient than Pt.

4.3 Higher coverage, solution phase

The above analysis was based on the assumption that the reactants are each at the preferred sites, that is, all reactants are within the orange region in Figure 1. In contrast, at higher coverage reactants might end up in the blue region, even though not preferred at low coverage. The adsorbate coverage on the catalyst surface can be as high as 2/3 monolayer, making the blue region accessible for binding. To consider the changes that might occur at higher coverage, we calculated the corresponding barriers for the blue region.

For O_2 dissociation, starting from b_{3a}, O_2 can dissociate to form O_{ad} in the f_{1a} and f_{1b} sites, with a barrier of 1.25eV with solvation and 0.72eV without solvation, both high barriers. An alternative is to form OOH with barrier of 0.13 eV and OOH dissociation barrier of 0.26 eV in solution. This leaves O_{ad} at f_{1b} (-4.40 eV binding). For f_{1b} O_{ad}, the corresponding O hydration reaction with nearby H_2O has a barrier of 0.48V in solution and has a barrier of 0.26 in the gas phase.

The following step of H_2O formation also has a low barrier of 0.32 eV with solvation and 0.24eV without solvation.

Hence, when the preferred region is covered with O_{ad}, O_2 can start to bind to the unfavored b_{3a}, and then form OOH which dissociates to O_{ad} and OH_{ad}. This allows a lower barrier for hydration into 2 OH. This might avoid the high O hydration (1.03eV barrier) and OH formation (1.20eV). The mechanism is as follows **OOH-diss-hydr-mechanism-high:**

$O_2 + H \rightarrow OOH$ (E_a = 0.19 at low coverage and 0.12 at high coverage),

$OOH \rightarrow O + OH$ (E_a = 0.00 at low coverage and 0.18 at high coverage),

$O + H_2O \rightarrow 2OH$ (E_a = 1.03eV at low coverage and 0.48eV at high coverage),

$OH + H \rightarrow H_2O$ (E_a = 0.41eV at low coverage and 0.32eV at high coverage).

Figure 3 shows the potential energy surface of OOH-form-hydr-high mechanism with solvent effect. The overall mechanism has O hydration as the RDS with a barrier of 0.48eV, smaller than the 0.50eV for Pt. This mechanism for the reaction on Pt_3Co happens at higher coverage.

Summarizing the above discussion, in gas phase the preferred mechanism is OOH-form-hydr with a RDS barrier of 0.47eV for Pt_3Co and 0.29eV for Pt. With solvation at low coverage, where all intermediates can bind to the preferred region, we predict that Pt_3Co would have slower kinetics than Pt with an overall barrier of 1.03eV. However, at higher coverage, the less preferred (blue) region leads to a RDS barrier of 0.48 eV, smaller than the Pt barrier of 0.50eV. This would be consistent with experiment.

5.0 Conclusion

We studied systematically the binding site preference of all reaction intermediates involved in ORR on Pt_3Co. The binding energy of adsorbates on the alloy surface show strong sublayer dependence. Compared with the pure Pt surface, the binding sites are partitioned into two regions, the preferred (orange) and the less-preferred (blue) region. The mechanism of ORR on Pt_3Co is different to that of Pt. At high coverages, O_2 first reacts with H_{ad} to form OOH_{ad}. OOH_{ad} then dissociates to OH_{ad} and O_{ad}. The O_{ad} next reacts with H_2O to produce OH_{ad}, which finally reacts with H_{ad} to form H_2O.

Due to the substantial difference in binding sites, ORR shows different kinetics on the preferred and less-preferred regions. The overall barrier for ORR in the preferred region is 1.03eV, while the barrier for the less-preferred region is 0.48eV. Thus ORR should be strongly coverage dependent. At low coverage, all reactants and intermediates adsorb only onto the preferred region, generating a slower reaction rate than with pure Pt. At higher coverage, O_2 begins to react on the less-preferred region, leading to a better rate as compared with pure Pt.

ACKNOWLEDGEMENTS: This work was supported partially by Ford Motor Company (Dr. Pezhman Shirvanian) and partially by the US Department of Energy under grant DE-AC02-

06CH11357. The facilities of the MSC used in this study were established with grants from DURIP-ONR and DURIP-ARO.

Figures and Tables.

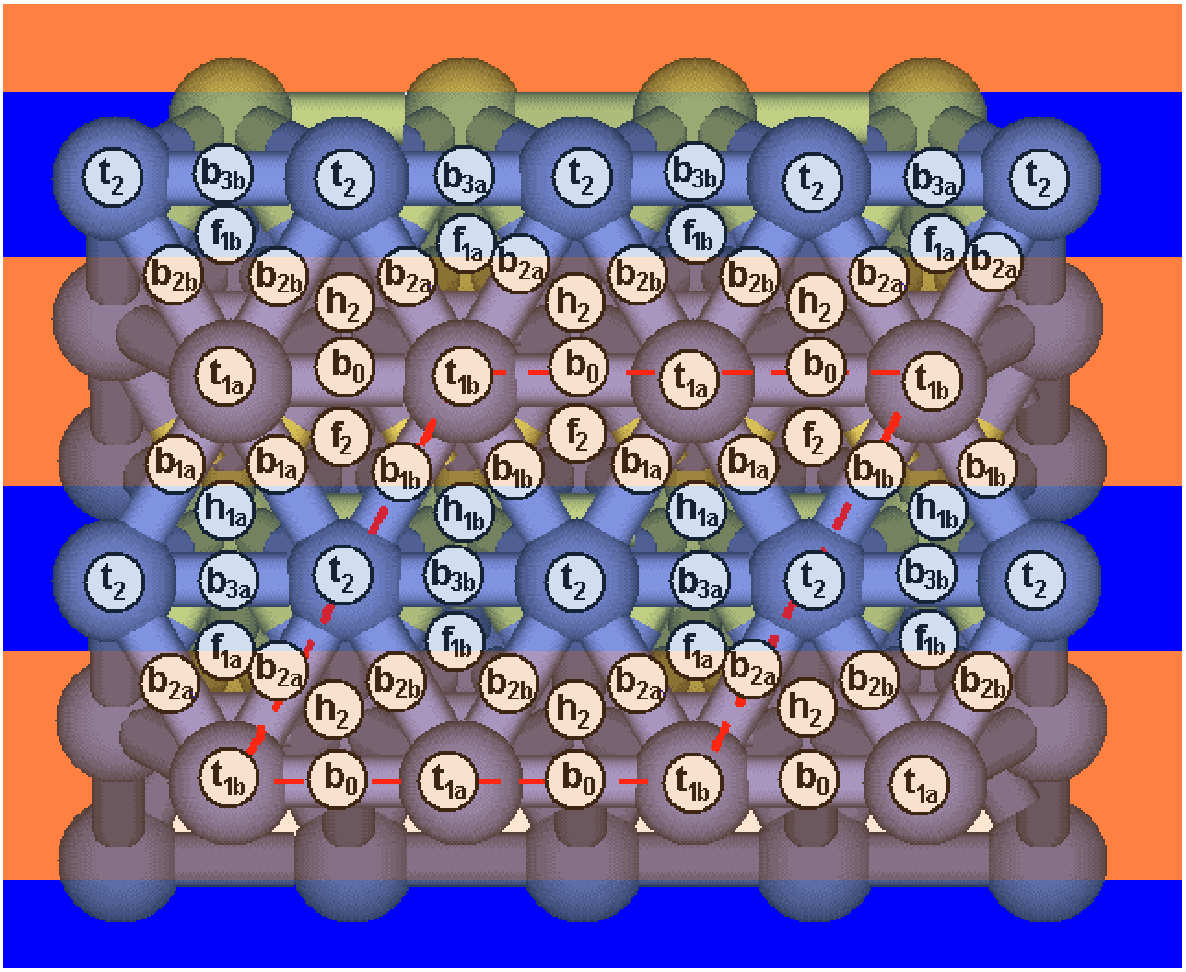

Figure 1. Binding sites on Pt_3Co surface. The blue and orange stripes indicate the partitioning of the Pt surface into two regions induced by the sublayer Co. The O_2, O, H, OH, and OOH species prefer to move only within the blue stripes.

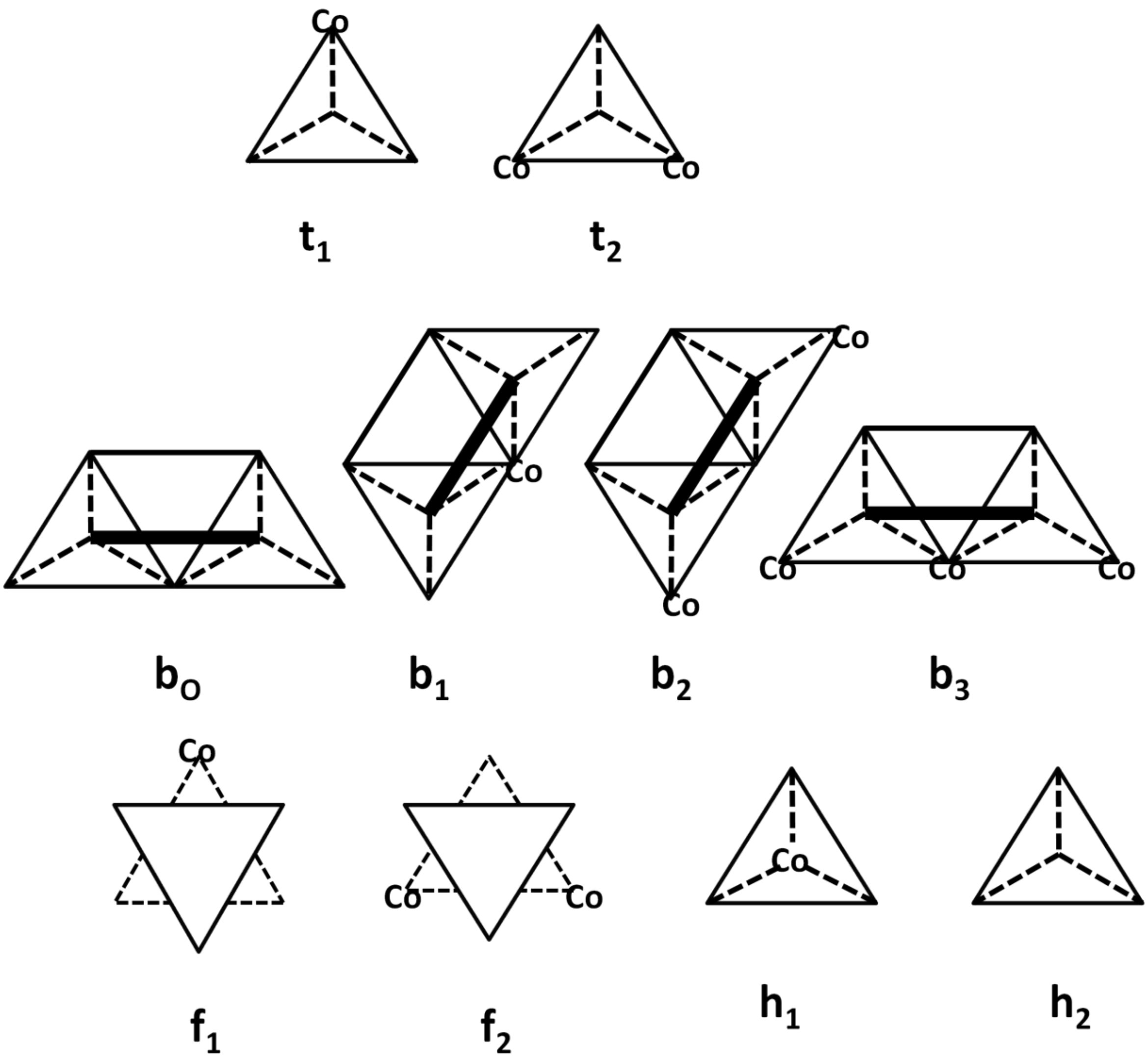
Co
Co
Co
t1
t2
Co
Co
Co
Co
Co
Co
Co
b0
b1
b2
b3
Co
Co
Co
Co
f1
f2
h1
h2

Figure 2. Illustration of various binding sites on Pt_3Co surface. For top sites t_1 and t_2, the triangle indicates the sublayer atoms. t_1 has one Co atom beneath it, while t_2 has two.

For bridge sites, the bridge itself is shown as the thick black line while the two termini of the black line connect the two surface atoms forming the bridge site. The trapezoid beneath are sublayer atoms. b_0-b_3 has 0-3 Co atoms in the sublayer.

An fcc site is in the center of a surface triangle (shown as solid triangle). f_1 and f_2 differ in the sublayer triangle beneath the surface triangle. f_1 has one Co beneath it while f_2 has two.

hcp sites are also in the center of a surface triangle. hcp sites have one sublayer atom beneath it. For h_1 it is Co while for h_2 it is Pt.

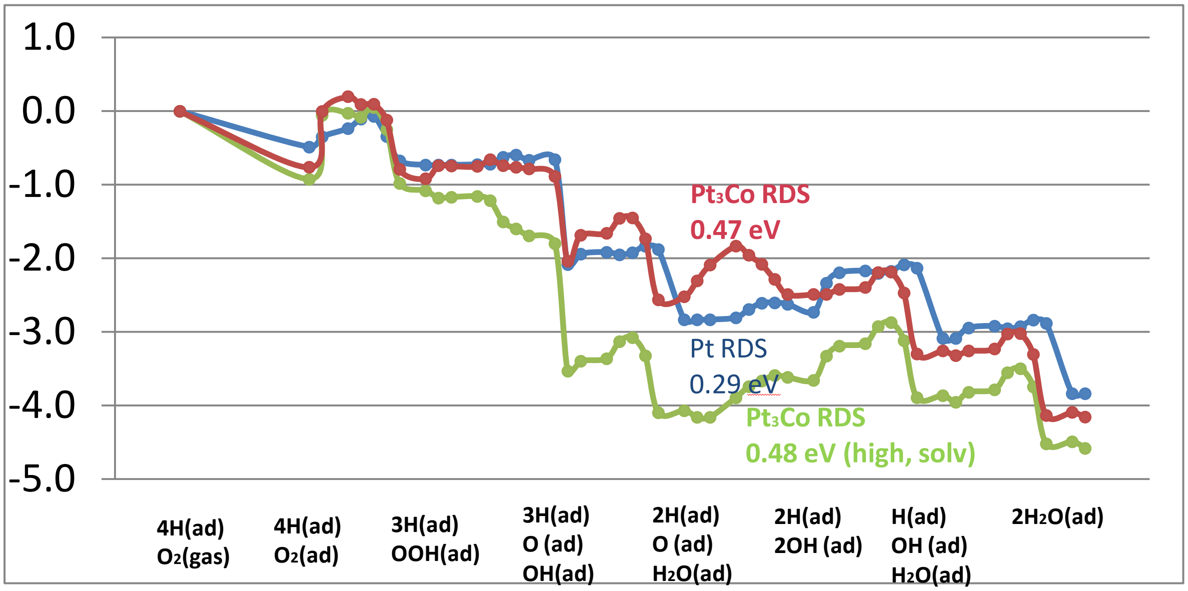

Figure 3. Potential energy surface including barriers for the OOH-form-hydr mechanism preferred for both Pt and Pt_3Co in gas phase. The green line shows the alternative mechanism at high coverage in solution phase for Pt_3Co.

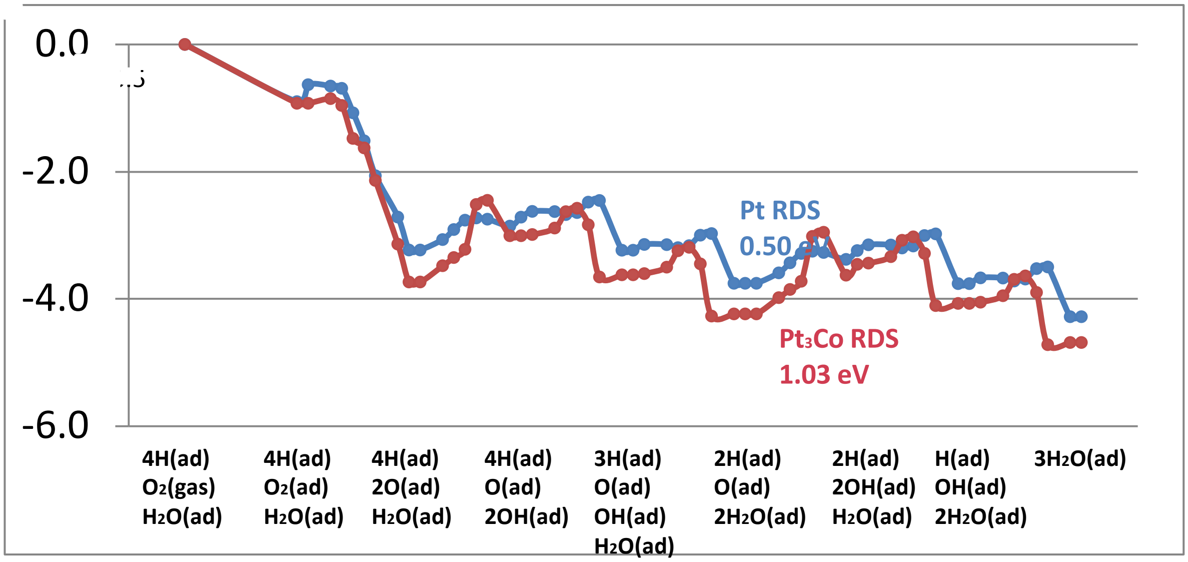

Figure 4. Potential energy surface including barriers for the O_2-diss-hydr mechanism preferred by both Pt_3Co and Pt in solution.

BE	BE	H	O	OH	O_2	OOH	H_2O	H_2O_2
Pt_3Co	t_{1a}	-2.71	-2.32	-2.80		-1.06	-0.26	
	t_{1b}	-2.74	-2.39	-2.80		-1.13	-0.35	
	t_2	-2.43	-2.22	-2.64		-0.98	-0.26	
	b_0	-2.59	-3.22	-2.71	-0.76			-0.36
	b_{1a}	-2.57		-2.77	-0.56			-0.37
	b_{1b}	-2.55		-2.70	-0.58			-0.37
	b_{3a}	-2.29	-2.91	-2.64	-0.63			-0.34
	b_{3b}	-2.31		-2.58	-0.46			-0.28
	b_{2a}	-2.58	-2.94	-2.65	-0.47			-0.46
	b_{2b}	-2.46	-2.91	-2.60	-0.31			-0.49
	f_2	-2.53	-3.56	-2.81	-0.36	-0.99		
	f_{1a}	-2.39	-3.27	-2.60	-0.35	-1.10		
	f_{1b}	-2.45	-3.14	-2.53	-0.28	-0.91		
	h_{1a}	-2.53	-3.09	-2.49	-0.41			
	h_{1b}	-2.49	-3.01	-2.54	-0.35			
	h_2	-2.48	-3.05	-2.86	-0.06			
	best	-2.74	-3.56	-2.86	-0.76	-1.13	-0.35	-0.49
Pt	t	-2.80	-2.50	-2.23		-1.06	-0.22	
	b	-2.70	-3.10	-2.25	-0.40			-0.27
	f	-2.72	-3.66	-2.22	-0.46			
	h	-2.70	-3.28	-2.28	-0.35			
	best	-2.80	-3.66	-2.28	-0.46	-1.06	-0.22	-0.27

Table 1. Binding energies of various species on different sites on Pt_3Co and Pt without solvation.

BE	sites	H	O	OH	O_2	OOH	H_2O	H_2O_2
Pt_3Co	t_{1a}	-2.79	-2.95	-3.31		-1.54	-0.69	
	t_{1b}	-2.83	-2.99	-3.29		-1.60	-0.75	
	t_2	-2.47	-2.76	-3.11		-1.46	-0.64	
	b_0	-2.70	-3.86	-2.99	-0.93			-0.71
	b_{1a}	-2.79		-3.16	-0.74			-0.72
	b_{1b}	-2.74		-3.12	-0.78			-0.74
	b_{3a}	-2.39	-3.50	-3.01	-0.76			-0.70
	b_{3b}	-2.46		-3.01	-0.63			-0.64
	b_{2a}	-2.69	-3.54	-3.01	-0.59			-0.82
	b_{2b}	-2.57	-3.57	-2.94	-0.45			-0.86
	f_2	-2.73	-4.63	-3.26	-0.79	-1.47		
	f_{1a}	-2.50	-3.90	-3.00	-0.52	-1.59		
	f_{1b}	-2.75	-4.40	-2.95	-0.51	-1.46		
	h_{1a}	-2.70	-3.85	-2.88	-0.58			
	h_{1b}	-2.75	-4.01	-3.00	-0.56			
	h_2	-2.61	-3.68	-3.19	-0.28			
	best	-2.83	-4.63	-3.31	-0.93	-1.60	-0.75	-0.86
Pt	t	-2.87	-3.09	-2.77		-1.52	-0.58	
	b	-2.82	-3.73	-2.63	-0.73			-0.61
	f	-2.85	-4.36	-2.57	-0.87			
	h	-2.81	-3.92	-2.64	-0.70			
	best	-2.87	-4.36	-2.77	-0.87	-1.52	-0.58	-0.61

Table 2. Binding energies of various species on different sites on Pt_3Co and Pt with solvation.

Reaction Barriers	Pt	Pt_3Co	Pt_3Co (high coverage)
H_2 Dissociation	0.00	0.17	
O_2 Dissociation	0.58	1.08	1.25
OH Formation	0.72	0.70	0.80
H_2O Formation	0.11	0.23	0.24
OOH Formation	0.28	0.20	0.13
OOH Dissociation	0.14	0.26	0.26
H-OOH dissociation	0.18	0.20	
O hydration	0.29	0.47	0.26**

* The O hydration on Pt is from 3x3 calculations because the c(2x2) cell is not large enough.

** For Pt_3Co, to keep the correct periodic condition, we used c(4x2).

Table 3. Reaction barriers for Pt_3Co and Pt without solvent effect.

Reaction Barriers	Pt	Pt_3Co	Pt_3Co (high coverage)
H_2 Dissociation	0.00	0.12	
O_2 Dissociation	0.00	0.07	0.72
OH Formation	1.09	1.20	1.02
H_2O Formation	0.17	0.41	0.32
OOH Formation	0.19	0.12	0.16
OOH Dissociation	0.00	0.18	0.08
H-OOH dissociation	0.04	0.29	
O hydration	0.50*	1.03**	0.48**

* The O hydration on Pt is from 3x3 calculations because the c(2x2) cell is not large enough.

** For Pt_3Co, to keep the correct periodic condition.

Table 4. Reaction barriers on Pt_3Co and Pt with solvent effect.

REFERENCES

(1) Kordesch, K.; Simader, G. *Fuel Cell and Their Applications*; VCH: New York, 1996.

(2) Appleby, A.; Foulkes, F. *Fuel Cell Handbook*; Van Nostrand Reinhold: New York, 1989.

(3) Brandon, N. P.; Skinner, S.; Steele, B. C. H. *Annu. Rev. Mater. Res.* **2003**, *33*, 183-213.

(4) Mehta, V.; Cooper, J. S. *J. Power Sources* **2003**, *114*, 32-53.

(5) Markovic, N. M.; Ross, P. N. *Surf Sci Rep* **2002**, *45*, 121-229.

(6) Stamenkovic, V. R.; Mun, B. S.; Arenz, M.; Mayrhofer, K. J. J.; Lucas, C. A.; Wang, G. F.; Ross, P. N.; Markovic, N. M. *Nat Mater* **2007**, *6*, 241-247.

(7) Stamenkovic, V.; Schmidt, T. J.; Ross, P. N.; Markovic, N. M. *J. Phys. Chem. B* **2002**, *106*, 11970-11979.

(8) Stamenkovic, V. R.; Fowler, B.; Mun, B. S.; Wang, G. F.; Ross, P. N.; Lucas, C. A.; Markovic, N. M. *Science* **2007**, *315*, 493-497.

(9) Yang, H.; Vogel, W.; Lamy, C.; Alonso-Vante, N. *J. Phys. Chem. B* **2004**, *108*, 11024-11034.

(10) Norskov, J. K.; Stamenkovic, V.; Mun, B. S.; Mayrhofer, K. J. J.; Ross, P. N.; Markovic, N. M.; Rossmeisl, J.; Greeley, J. *Angew Chem Int Edit* **2006**, *45*, 2897-2901.

(11) Gauthier, Y. *Surf Rev Lett* **1996**, *3*, 1663-1689.

(12) Yu, T.; Sha, Y.; Merinov, B.; Goddard III, W. *The Journal of Physical Chemistry C* **2010**, *114*, 11527-11533.

(13) Gauthier, Y.; Joly, Y.; Baudoing, R.; Rundgren, J. *Phys Rev B* **1985**, *31*, 6216-6218.

(14) Melius, C. F.; Goddard, W. A. *Phys. Rev. A* **1974**, *10*, 1528-1540.

(15) Melius, C. F.; Olafson, B. D.; Goddard, W. A. *Chem. Phys. Lett.* **1974**, *28*, 457-462.

(16) Redondo, A.; Goddard, W. A.; Mcgill, T. C. *Phys Rev B* **1977**, *15*, 5038-5048.

(17) Hamann, D. R. *Phys Rev B* **1989**, *40*, 2980.

(18) Schultz, P.; SeqQuest code project, Sandia National Laboratories, (http://www.cs.sandia.gov/~paschul/Quest/).

(19) Sha, Y.; Yu, T. H.; Liu, Y.; Merinov, B. V.; Goddard, W. A. *J Phys Chem Lett* **2010**, *1*, 856-861.

(20) Sha, Y.; Yu, T. H.; Merinov, B. H.; Shirvanian, P.; III, W. A. G. *Accepted by J. Phys. Chem. Lett* **2010**.

The Mechanism for Degradation of Nafion in PEM Fuel Cells from Quantum Mechanics Calculations

Ted H. Yu,[†] *Yao Sha,* [†] *Wei-Guang Liu,* [†] *Boris V. Merinov,* [†] *Pezhman Shirvanian,*[‡]
*and William A. Goddard III**[,†]
[†]Materials and Process Simulation Center

California Institute of Technology, MC 139-74, Pasadena, California 91125

[‡]Ford Motor Co., Research & Advanced Engineering

2101 Village Rd, Dearborn, Michigan 48104

1200 E California Blvd MC 139-74, Pasadena, CA 91125 M/S 139-74

Phone: +1 626 395 2731 FAX +1 626 585 0918

* Email: wag@wag.caltech.edu

ABSTRACT: We report results of quantum mechanics (QM) mechanistic studies of Nafion membrane degradation in a polymer electrolyte membrane (PEM) fuel cell. Experiments suggest that Nafion degradation is caused by generation of trace radical species (such as $OH^{\bullet}$, $H^{\bullet}$) only when in the presence of H_2, O_2, and Pt. We use density functional theory (DFT) to construct the potential energy surfaces for various plausible reactions involving intermediates that might be formed when Nafion is exposed to H_2 (or H^+) and O_2 in the presence of the Pt catalyst. We find a barrier of 0.53 eV for OH radical formation from HOOH chemisorbed on Pt(111) and of 0.76 eV from chemisorbed OOH_{ad}, suggesting that OH might be present during the ORR, particularly when the fuel cell is turned on and off. Based on the QM, we propose two chemical mechanisms for OH radical attack on the Nafion polymer:

1) OH attack on the S-C bond to form H_2SO_4 plus a carbon radical (barrier: 0.96 eV) followed by decomposition of the carbon radical to form an epoxide (barrier: 1.40 eV).
2) OH attack on H_2 crossover gas to form hydrogen radical (barrier: 0.04 eV), which subsequently attacks a C-F bond to form HF plus carbon radicals (barrier as low as 1.00 eV). This carbon radical can then decompose to form a ketone plus a carbon radical with a barrier of 0.86 eV.

The products (HF, OCF_2, SCF_2) of these proposed mechanisms have all been observed by F NMR in the fuel cell exit gases along with the decrease in pH expected from our mechanism.

KEYWORDS: Nafion, degradation, OH radical, heterogeneous catalysis, fuel cell, DFT, Pt Catalyst, ORR, PEMFC

MANUSCRIPT TEXT

1. **Introduction**

Proton exchange membrane fuel cells (PEMFCs) convert hydrogen to electricity efficiently, with water as their main waste product. Their small size and low operating temperature (~ 70-85^{o}C) make PEMFCs ideal for automotive applications if Nafion membranes could meet the 5,000-10,000 hour operational requirement. The general consensus is that hydrogen peroxide and radicals are involved in the chemical degradation of Nafion[1-14]. The presence of such radicals has been detected directly through spin trapping ESR methods[10,12,14] in a fuel cell environment. However there are several distinctly different interpretations of these experiments on how the radicals are generated and what mechanism is responsible for the Nafion chemical degradation. Since hydroxyl radicals are introduced by Fenton's reagents, many experiments have been conducted to show that Nafion does degrade in the presence of Fenton's reagents[1,5,7]. Since Fenton's reagents are not observed in appreciable quantities under normal fuel cell operating conditions, it has been suggested [8,9] that Pt nanoparticles break off from the cathode/anode catalyst during operation and form Fenton-like reagents with HOOH once they are in the membrane. However, experiments show that chemical degradation of Nafion can occur without nanoparticles breaking off[1-3,6], leading to the conclusion that hydroxyl radicals must be generated even when the Fenton-like reagents are not presented.

Nafion has excellent thermal and mechanical stability due to its fluoropolymer structure (Figure 1). But there is evidence that Nafion chemically degrades through OH radical attack at defects such as C-H and C=C that might result from the manufacturing process[4,7]. An often-cited defect vulnerable to such attack is the main chain carboxylic acid group that appears unintentionally from the initiators during polymerization process[1,5,6].

Many mitigation strategies have been proposed to reduce Nafion degradation in PEMFCs including:

1) decreasing Fenton contaminants,

2) chemically degrading OH radicals that are formed during operation,

3) chemical stabilization of defect sites, and

4) membrane reinforcement during cycling[15].

It would be useful to obtain a good understanding of the degradation mechanism, so that the focus could be on the most relevant strategies. For example, the strategy of reducing Fenton contaminants may be ineffective if Fenton's reagents are not the source of the OH radical. Also, the strategy to chemically stabilize defect sites may not be effective if the sites inherent to Nafion are vulnerable to radical attack.

Recently, Ghassemzadeh et al.[6] used F NMR to show that *Nafion degradation occurs only when Pt catalyst,* H_2*, and* O_2 *are all present, but not otherwise*. Their work emulated conditions for fuel cell operation at cathode and anode, when either H_2 or O_2 may cross over to the other electrode. After 120 hours of operation, the F NMR showed significant loss (~ 10%) of OCF_2 and SCF_2 side chain groups. This and some other studies[2,3] suggest that the degradation can occur at relatively mild open circuit conditions, where there is no dissolution of Pt catalyst into Nafion. In addition, Ghassemzadeh[6] observed significant degradation at the side chains and proposed mechanisms by which Nafion can degrade through non-defect side chain sites.

Here, we investigate mechanisms underlying the chemical degradation of Nafion under open circuit conditions using first-principles quantum mechanics (QM) as outlined in Section 2. Section 3 reports results of calculating the energetics of various possible degradation mechanisms.

2. Computational Methods

We used the SeqQuest[16] code for the Perdew, Burke, and Ernzerhof [17] (PBE) flavor of Density Functional Theory (DFT) with a double zeta plus polarization basis set of contracted Gaussian functions optimized for periodic calculations. Our calculations used a periodic slab of Pt with 6 closest-packed layers The density grid was 6 points per angstrom, while the reciprocal space grid was 5×5×0. We also predicted the effects due to solvation using a periodic Poisson-Boltzmann solver[18,19] to obtain the free energy of solute-solvent interaction.

Non-periodic QM calculations were carried out using the B3LYP[20,21] hybrid DFT functional with the Jaguar code[22]. Here we used the 6-311g**[23] basis set. All geometries were optimized using the analytic Hessian to determine that the local minima have no negative curvatures (imaginary frequencies), and the transition state structures lead to exactly one negative curvature. The vibrational frequencies from the analytic Hessian were used to calculate the zero-point energy corrections at 0 K, which were added to the Jaguar implicit solvation correction and the QM energy ($\Delta[E]$) to obtain the enthalpy at 0 K.

3. Results and Discussion

Formation of OH Radicals

Based on the QM (including solvation), we previously determined the mechanism for the oxygen reduction reaction (ORR) between the $(H_3O)^+$ migrating through the Nafion from the anode to the cathode and O_2 at the cathode to form H_2O on the Pt (111) surface[24,25]. The catalyst plays a crucial role in facilitating reactions that generate OH radicals chemisorbed on the catalyst. The current work used similar DFT calculations to determine the energetics of HOOH and OH radical formation on the Pt (111) surface (see Table 1 and corresponding structures in Figure 2). We find that on Pt in solution the barrier to form the OH radical from HOOH is 0.53 eV while the barrier to OH from OOH is 0.76 eV. Without the Pt catalyst, the barrier to form the OH radical from HOOH is 2.66 eV. This barrier is dramatically reduced on the Pt (111) surface, because Pt binds more strongly to both product species (O and OH) than to the reactant species (OOH and HOOH).

Our results demonstrate that OH radicals can be formed when H_2 and O_2 gases react on a Pt surface in a PEMFC as result of H_2 gas crossover to the cathode[10,13] or from O_2 gas crossover to the anode[12,14]. Figure 3 shows the potential energy landscape of reactions involving H_2 (or H^+), O_2 and Pt (111) surface in in the membrane during ORR. It should be noted that H_2 gas and H^+

have the same energy in the context of the standard hydrogen electrode[26]. Figure 3 includes data for the barriers for the OH formation, OOH formation, OOH dissociation, O_2 dissociation, and HOH formation published previously[25]. We find that the following mechanisms for forming OH radicals have reasonably low energetic barriers:

$H_2 + O_2 \rightarrow O_{2ad} + 2H_{ad} \rightarrow OOH_{ad} + H_{ad} \rightarrow O_{ad} + H_{ad} + OH_{radical}$ 0.76 eV (solv),

$H_2 + O_2 \rightarrow O_{2ad} + 2H_{ad} \rightarrow OOH_{ad} + H_{ad} \rightarrow HOOH_{ad} \rightarrow OH_{ad} + OH_{radical}$ 0.53 eV (solv),

if crossover of H_2 from the anode and O_2 from the cathode are present.

The Ghassemzadeh experiments [6] showed that Nafion *degradation is not observed* when Nafion is exposed to H_2 and O_2 gases without Pt. This agrees with our conclusion that the Pt catalyst surface plays a key role in OH radical formation, and therefore, Nafion degradation. Figure 3 shows that formation of OH radicals occurs only if O_{2ad} forms OOH_{ad} by reaction with H_{ad} (the upper blue path) rather than the O_{2ad} dissociating to $2O_{ad}$ (the lower orange path). This barrier for the O_2 dissociation is lower than that for the OOH formation, 0.25 vs. 0.37 eV. Thus, the energetically most favorable pathway does not lead to OH radical formation. However, under conditions where the Pt surface is highly saturated with adsorbates, O_2 dissociation may be inhibited because it requires two empty three-fold fcc sites to dissociate by forming two adsorbed oxygens[25]. When the Pt surface is completely saturated with both H_{ad} and O_{2ad}, the O_2 dissociation is limited by available surface space. In contrast, the OOH formation mechanism, which may lead to OH radical formation, is more favored when the surface is saturated with a concentrated amount of H and a dilute amount of O_2. Figure 4 illustrates this concept showing how $O_{2ad} \rightarrow 2O_{ad}$ can proceed at low coverage but is hindered when the surface is saturated with adsorbed H. Figure 4 also shows that $O_{2ad} + H_{ad} \rightarrow OOH_{ad}$ is not impeded by high coverage of adsorbed H. Indeed, the Ghassemzadeh experiments[6] show that Nafion degradation is greater for gas mixtures that are H_2-rich (90% H_2, 2% O_2, 8% Ar) than for those that are O_2-rich (20% O_2, 2% H_2, 78% Ar), which agrees with our proposed mechanisms.

Degradation of Nafion from OH Radicals

After OH radicals are formed on the Pt surface, they can chemically degrade Nafion. Various mechanisms have been proposed on how OH radicals attack Nafion. Some mechanisms focus on defect sites, created in small quantities due to inherent flaws in the manufacturing process[3-7]. In this case, eliminating these defect sites would be an effective strategy in preventing Nafion degradation. However, our analysis suggests that Nafion *degradation can occur even if there are no defects in the Nafion membrane*. Thus, it is inherent in the chemical structure of Nafion.

To determine whether OH radicals can attack defect-free Nafion, we focus on the sulfonic acid groups. The C-F bonds in Nafion chains are very strong, but the C-S bond can be attacked by OH radicals. Ghazzamedeh et al. proposed the mechanism in Figure 5 to explain Nafion side chain degradation in the presence of OH radicals[6]. We calculated the enthalpies of this mechanism, but find very high barriers for two steps in this mechanism, making it unlikely at the normal 80°C operating temperature:

1. The sulfonate radical breaking off from the side chain to form SO_3 was calculated to be +2.19 eV (Figure 5B).

2. The barrier to form an aldehyde and HF from an alcohol is 1.94 eV (Figure 5D).

Kumar [27] proposed a similar degradation mechanism and calculated its energetics using DFT (Gaussian 03). They found that three of the steps in the mechanism have barrier values between 1.52 and 1.91 eV. Both of these proposed mechanisms involve high barriers and require multiple OH radicals, making them implausible.

We propose a new Nafion side chain degradation mechanism that leads to low barriers and which require only one OH radical to initiate degradation of the Nafion side chain. Since the sulfonic acid side chain group is a very strong acid ($pK_a = -2.8$), we calculated the barrier of breaking the side chain group deprotonated ($-CF_2SO_3^-$) rather than protonated ($-CF_2SO_3H$). We find (Figure 6A) two mechanisms by which the OH radical can break the C-S bond:

1. C Attack: $OH^{\bullet}$ attack on the C.

   $CF_2\text{-}SO_3^- + OH^{\bullet} \rightarrow \text{-}CF_2OH + {}^{\bullet}SO_3^-$ $\Delta E = -1.95$ eV (barrier: 1.80 eV

2. S Attack. OH attack on the S atom.

   $\text{-}CF_2\text{-}SO_3^- + OH^{\bullet} \rightarrow \text{-}CF_2^{\bullet} + HSO_4^-$ $\Delta E = -0.92$ eV (barrier: 0.96 eV)

Alternatively, the OH radical can attack the minority species, a protonated sulfonic acid group in a similar fashion.

3. Neutral sulfonate attack:

   $\text{-}CF_2\text{-}SO_3H + OH^{\bullet} \rightarrow \text{-}CF_2^{\bullet} + H_2SO_4$ $\Delta E = -1.10$ eV (barrier: 0.81 eV)

We expect S-attack on the deprotonated sulfonic acid group (+0.96 eV) to be the dominant first step in degradation by OH radicals. The first initial step of breaking the C-S bond (Figure 6A), leads to formation of an epoxide that breaks off from the side chain (Figure 6B) (Barrier = 1.40 eV). This epoxide unzipping reaction can propagate along the side chain until the side chain is completely devoid of ether groups via (Figure 6B):

$\text{-}CF_2\text{-}CF\text{-}[O\text{-}CF_2\text{-}C(CF_3)F^{\bullet}]_z \rightarrow \text{-}CF_2\text{-}CF\text{-}[O\text{-}CF_2\text{-}C(CF_3)F^{\bullet}]_{(z-1)}$ + epoxide.

The epoxides formed by this mechanism can react with water to form tetrafluoroethylene glycol, $HO\text{-}CF_2\text{-}CF_2\text{-}OH$ (Figure 6C).

An alternative second process for decomposition after S-attack is for ethene to dissociate from the side chain via:

$\text{-}CF\text{-}[O\text{-}CF_2\text{-}C(CF_3)F]_z\text{-}O\text{-}CF_2\text{-}CF_2^{\bullet} \rightarrow \text{-}CF\text{-}[O\text{-}CF_2\text{-}C(CF_3)F]_z\text{-}O^{\bullet} + CF_2{=}CF_2$. ($\Delta E = 1.36$ eV)

The perfluoryl ethene can subsequently react with water to form $H\text{-}CF_2\text{-}CF\text{-}OH$ ($\Delta E = -1.82$ eV).

This S-attack mechanism leads to removal of both OCF_2 and SCF_2 groups from Nafion (both have been identified by F NMR[6]) . This explains why ~ 10% reduction of these groups from the Nafion occurs after 120 hours exposure to H_2, O_2, and Pt catalyst. Products of this reaction are

H_2SO_4 and tetrafluoroethylene glycol (or tetrafluoroethyl alcohol), which agree well with exit water analysis from experiment[6], which show the greatly reduced pH expected from sulfuric acid formation, and which observes F NMR signals of OCF_2 corresponding to the tetrafluoroethylene glycol.

Degradation of Nafion from H Radicals

Ghassemzadeh[6] experimentally observed HF in the exit stream of a fuel cell in which Nafion undergoes degradation, but HF is not a product of the mechanism described in the previous section. Next, we propose a second Nafion side chain degradation mechanism with low overall barrier that explains the formation of HF.

This reaction mechanism is shown in Figure 7. It begins with OH radicals reacting with H_2 crossover gas to form H radical (Figure 7A) (0.04 eV barrier). These H radicals then react with the C-F bond directly to form HF. It is favorable for an H radical to react with fluorines bonded to secondary or tertiary carbons with barriers and enthalpies listed below:

<u>Fluorine on secondary carbon</u>: $\Delta E = -1.00$ eV (barrier: 1.23 eV)

$-CF_2-C(CF_3)F-O-CF_2-CF_2-SO_3^- + H^\bullet \rightarrow -CF_2-C(CF_3)F-O-{}^\bullet CF-CF_2-SO_3^- + HF$

<u>Fluorine on tertiary carbon</u>: $\Delta E = -1.05$ eV (barrier: 1.00 eV) (Fig. 7B)

$-CF_2-C(CF_3)F-O-CF_2-CF_2-SO_3^- + H^\bullet \rightarrow -CF_2-C(CF_3)^\bullet-O-CF_2-CF_2-SO_3^- + HF$.

The easiest C-F bond to break is a fluorine on tertiary carbon bonded to two carbons and one oxygen. This is found in two locations:

1) on the side chain carbon bonded to the $-O-CF_2CF_2-SO_3^-$ group (described above), and

2) the backbone carbon that connects to the side chain.

<u>H radical reaction with fluorine on backbone carbon (Figure 7B):</u>

$-CF_2-CF_2-CF(O....SO_3^-)-CF_2-CF_2- + H^\bullet \rightarrow -CF_2-CF_2-C^\bullet (O....SO_3^-)-CF_2-CF_2- + HF$.

Following formation of the carbon radical and HF, the ether C-O bond can break to form a ketone and a carbon radical as shown in Figure 7C. This mechanism removes both OCF_2 and

SCF_2 groups from Nafion, and these groups will end up in the exit stream, as observed with F NMR [6].

Our proposed mechanism depends on having a modest concentration of H_2 gas in the same region where there is OH, since the H radicals are generated when H_2 gas reacts with OH radicals. Indeed Ghassemzadeh[6] showed that the rate of the Nafion degradation increases when the gas mixture (containing H_2, O_2, and Ar) is highly concentrated in H_2 rather than O_2. Thus our mechanism explains the experimental[6] observation that greater degradation occurs when there is increased H_2 in the system.

In addition, to H_{rad} reacting with the Nafion chain to form HF, it is also favorable for H_{rad} to react with the sulfonate group:

$CF_2\text{-}SO_3^- + H^\bullet \rightarrow -CF_2^\bullet + HSO_3^- \quad \Delta E = -0.91$ eV (no barrier)

The radical product of this reaction can continue to decompose the Nafion side chain as in Figure 6B-C. This reaction with H radical has similar exothermicity as the one involving OH radical (-0.91 vs. -0.92 eV), but has no barrier. The new product HSO_3^- could be expected to produce H_2SO_3 and SO_2, both of which were observed[2] in mass spectroscopy of the fuel cell cathode exit gas. This supports the role of H radicals in the degradation of Nafion.

Degradation of Nafion from OOH Radicals

The H radical discussed above would react with dioxygen to produce $OOH^\bullet$ ($\Delta E = -2.24$ eV, no barrier) which can also lead to degradation of Nafion, as suggested previously[4-6,9]. Thus, $OOH^\bullet$ can attack the C-S bond

$CF_2\text{-}SO_3^- + OOH^\bullet \rightarrow -CF_2^\bullet + HOSO_4^- \quad \Delta E = 0.62$ eV (Barrier = 1.22)

just as does $OH^\bullet$. However for OOH, the exothermicity is reduced by 1.54 eV and the barrier is 0.26 eV higher.

Conclusion

We show three mechanisms by which OH radical species form on a Pt surface, and which cause degradation of a defect-free Nafion polymer.

- S-attack: the OH radical reacts with the carbon-sulfur bond of the Nafion sidechain to form H_2SO_4 (lowering the pH) while generating radicals that decompose to $-OCF_2-$.
- C-attack: the OH radical attacks crossover H_2 leading to H radical that in turn reacts with the Nafion sidechains to form HF plus $-OCF_2-$ and $-SCF_2$ groups.
- S-attack by H radical: the H radical from OH reacting with crossover H_2, attacking the sulfonate group, forming H_2SO_3, leading to subsequent degradation similar to the S-attack mechanism.

All the products of these three mechanisms have been observed with F NMR and mass spectroscopy in the exit gases in fuel cell experiments, as has as the decrease in pH. We consider that the excellent agreement with the experimental observation provides a strong validation of our mechanisms for degradation of defect-free Nafion.

Previously, some workers have assumed that degradation of Nafion in a fuel cell is dominated by radicals attacking defects in the Nafion structure. For example, Choudhury assumed that degradation occurs at defects in the Nafion, and listed stabilization of polymer defects as a mitigation strategy to address this[15]. Another suggestion was that undesired Fenton's reagents are formed from Pt nanoparticles breaking off from the catalyst surface[8,9], and that elimination of Fenton's reagents will reduce degradation[15]. We showed in this paper that neither strategy should be completely effective because OH radicals generated by reactions associated with ORR on the Pt catalyst can attack a defect-free Nafion sidechain.

We suggest that one promising strategy to reduce Nafion degradation would be to modify the catalysts to disfavor formation of the peroxides that lead to OH formation during on-off cycling. Also, one might consider polymers that are more resistant to radical attack. For example, we found that H radical attacks fluorine on a tertiary carbon with a barrier of 1.00 eV, while the barrier for attacking fluorine on a secondary carbon is 1.23 eV. Thus maybe the Nafion side chain can be modified to eliminate fluorine on tertiary carbons altogether by replacing such F with CF_3. This will increase the barrier to form HF by 0.23 eV, slowing Nafion degradation. Additionally, our analysis shows that Nafion degradation will be greater on long side chain Nafion that has two F on tertiary carbon (Figure 1 with $z = 1$) compared to short side chain Nafion that have only one (Figure 1 with $z = 0$). Indeed this is consistent with recent experiments.[28]

ACKNOWLEDGMENT:

This work was supported with funding from the Ford Motor Company.

Table 1. The DFT-predicted reaction energetics involved in the formation of OH radical on a Pt surface. The energy of the reaction, ΔE, and barrier, E_{TS}, for the reactions are shown for both gas phase and solvation phase. The corresponding structures of the reaction are shown in Figure 2.

Reaction step barrier (eV)	ΔE(gas)	E_{TS}(gas)	ΔE(solv)	E_{TS}(solv)
$H_{ad} + OOH_{ad} \rightarrow HOOH_{ad}$ (Fig. 2A)	0.23	0.53	-0.09	0.26
$HOOH_{ad} \rightarrow OH_{ad} + OH^{\bullet}$ (Fig. 2B)	0.76	0.77	0.35	0.53
$OOH_{ad} \rightarrow O_{ad} + OH^{\bullet}$ (Fig. 2C)	0.91	0.97	0.42	0.76
HOOHad → 2OHad (Fig. 2D)	-1.31	0.45	-1.88	0.12

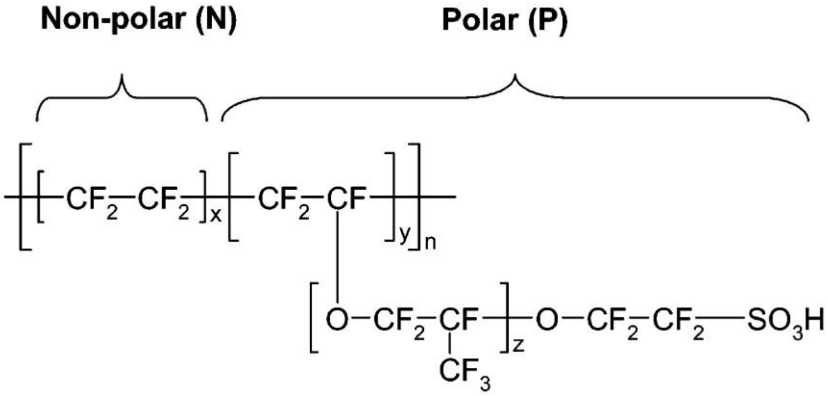

Figure 1. Chemical structure of Nafion. Nafion 117 has an average composition of x = 6.5, y = 1, z = 1. N indicates the nonpolar monomeric units while P indicates the polar monomeric units.

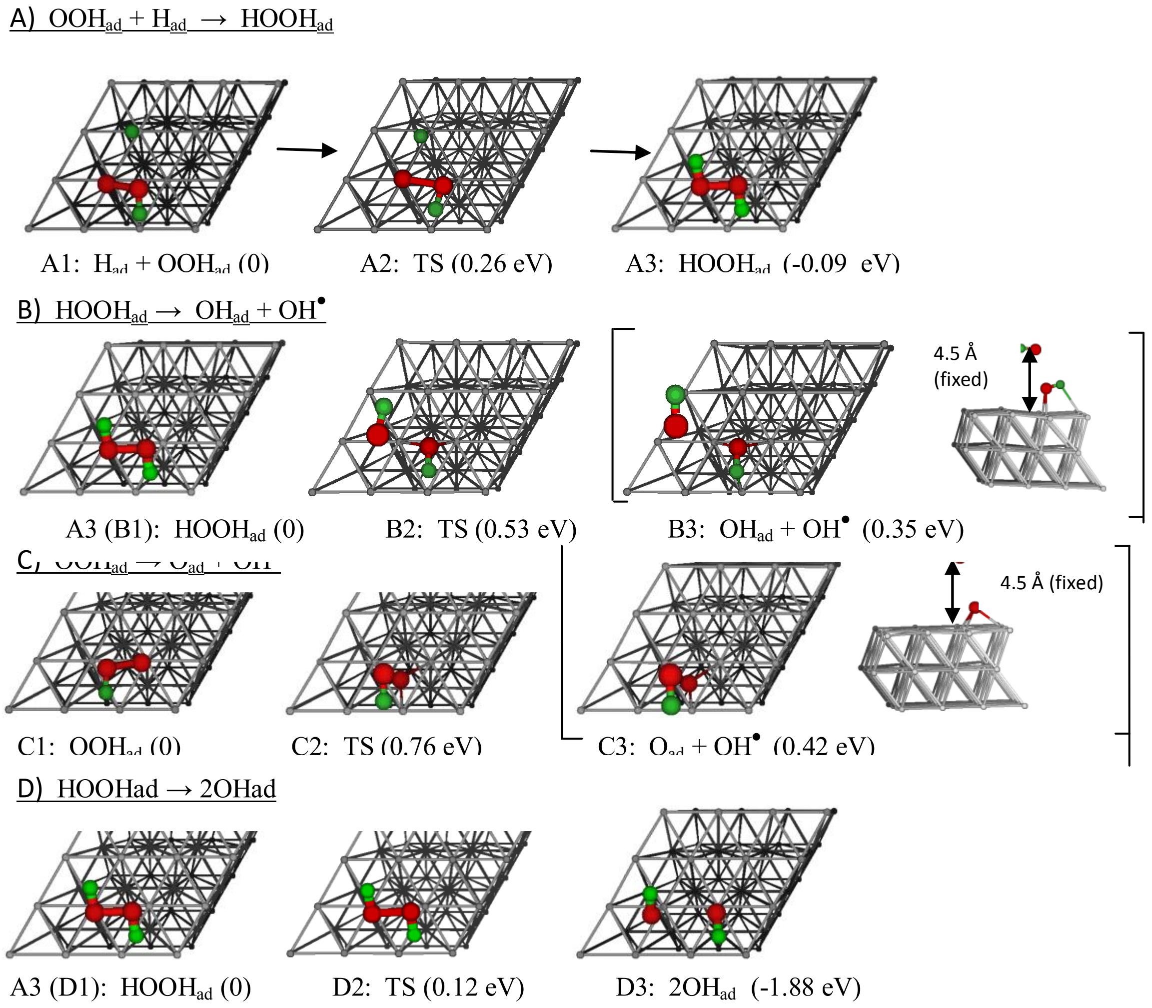

A) $OOH_{ad} + H_{ad} \rightarrow HOOH_{ad}$

A1: $H_{ad} + OOH_{ad}$ (0)

A2: TS (0.26 eV)

A3: $HOOH_{ad}$ (-0.09 eV)

B) $HOOH_{ad} \rightarrow OH_{ad} + OH^{\bullet}$

A3 (B1): $HOOH_{ad}$ (0)

B2: TS (0.53 eV)

B3: $OH_{ad} + OH^{\bullet}$ (0.35 eV)

C) $OOH_{ad} \rightarrow O_{ad} + OH^{\bullet}$

C1: OOH_{ad} (0)

C2: TS (0.76 eV)

C3: $O_{ad} + OH^{\bullet}$ (0.42 eV)

D) HOOHad → 2OHad

A3 (D1): $HOOH_{ad}$ (0)

D2: TS (0.12 eV)

D3: $2OH_{ad}$ (-1.88 eV)

Figure 2. Nudged elastic band (NEB) reaction paths of HOOH formation and OH radical formation from DFT, corresponding to solvent energies in Table 1. Calculated energy results for 2x2 cells (4x4 cells in figure shown for clarity)

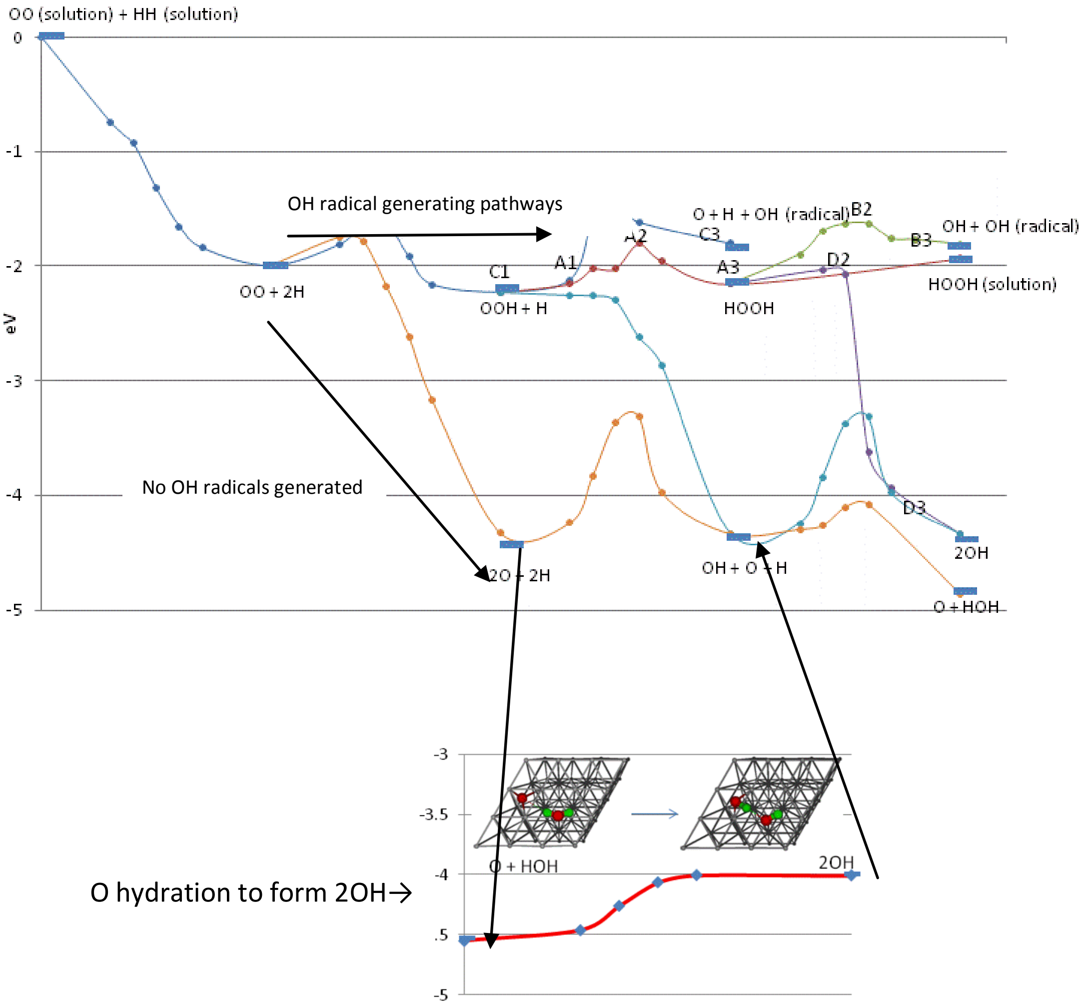

Figure 3. Potential energy map of H_2 (or H^+) and O_2 reacting in solvent phase. The labels A1 to C4 represent coordinate geometries shown in Figure 2 of our new reaction mechanisms. The other energies were calculated previously[25]. To form OH in the ORR, the reaction $O_{ad} + HOH_{ad} \rightarrow 2OH_{ad}$ (barrier = 0.50 eV)[25] was previously proposed as an alternative to direct OH formation from O_{ad} and H_{ad}.

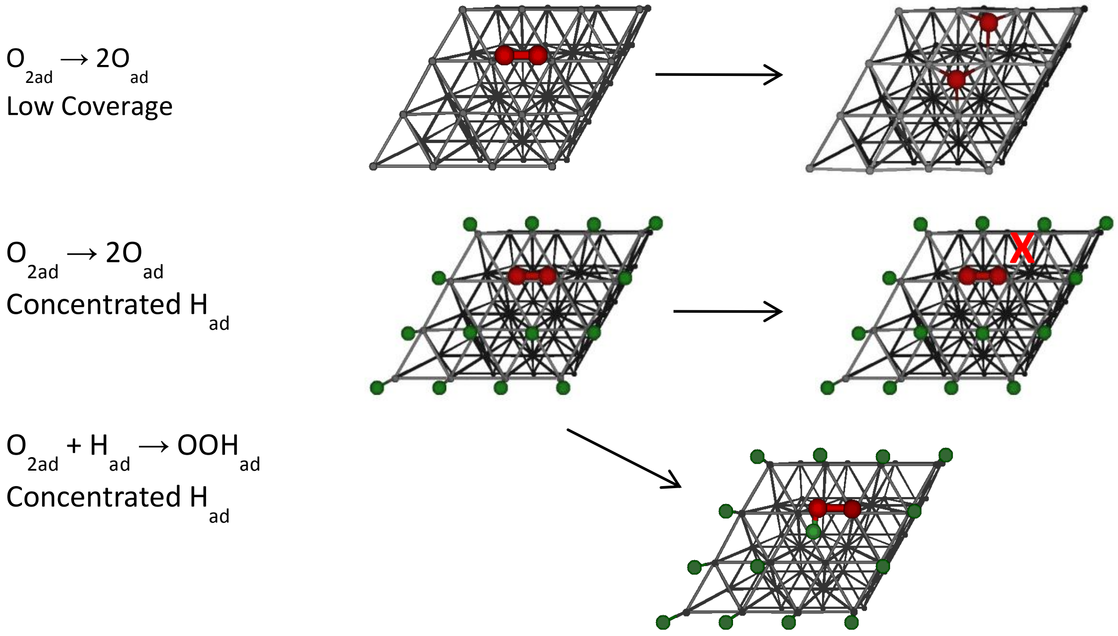

Figure 4. Illustration on the effect of high concentration of H_2 on the surface reactions of O_2. In a surface covered with H_{ad}, $O_{2ad} \rightarrow 2O_{ad}$ is hindered. However $H_{ad} + O_{2ad} \rightarrow OOH_{ad}$ is not. This explains why in experiments with a high concentration of H_2 gas, Nafion degradation occurs at a higher rate.

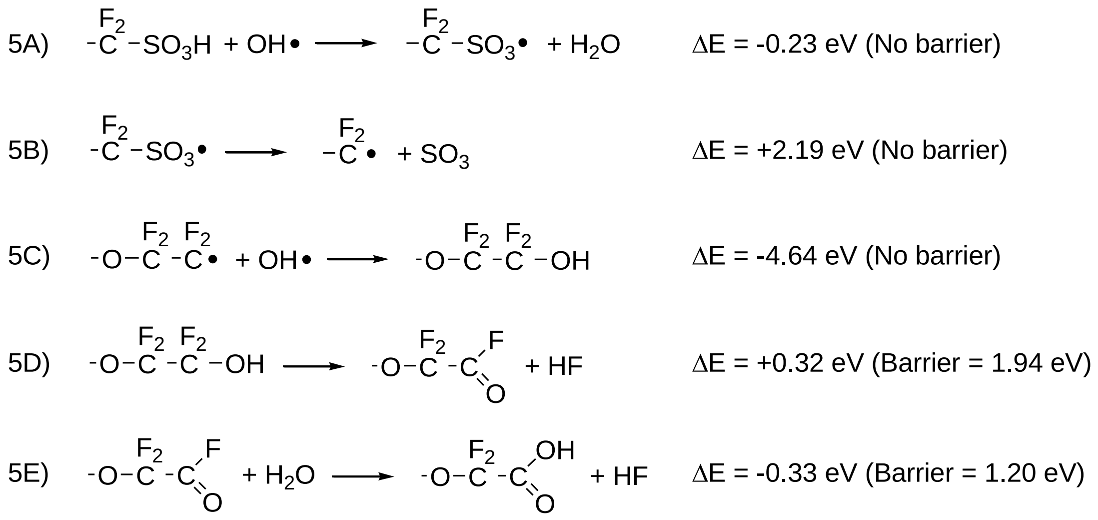

5A) $-\overset{F_2}{C}-SO_3H + OH\bullet \longrightarrow -\overset{F_2}{C}-SO_3\bullet + H_2O$ ΔE = -0.23 eV (No barrier)

5B) $-\overset{F_2}{C}-SO_3\bullet \longrightarrow -\overset{F_2}{C}\bullet + SO_3$ ΔE = +2.19 eV (No barrier)

5C) $-O-\overset{F_2}{C}-\overset{F_2}{C}\bullet + OH\bullet \longrightarrow -O-\overset{F_2}{C}-\overset{F_2}{C}-OH$ ΔE = -4.64 eV (No barrier)

5D) $-O-\overset{F_2}{C}-\overset{F_2}{C}-OH \longrightarrow -O-\overset{F_2}{C}-C(=O)F + HF$ ΔE = +0.32 eV (Barrier = 1.94 eV)

5E) $-O-\overset{F_2}{C}-C(=O)F + H_2O \longrightarrow -O-\overset{F_2}{C}-C(=O)OH + HF$ ΔE = -0.33 eV (Barrier = 1.20 eV)

Figure 5. Mechanism of degradation of Nafion sulfonic acid group proposed by Ghassemzadeh et al.[6] Energetics are from our DFT calculations. We consider steps 5B and 5D to be unlikely at normal fuel conditions.

6A) Radical Substitution:

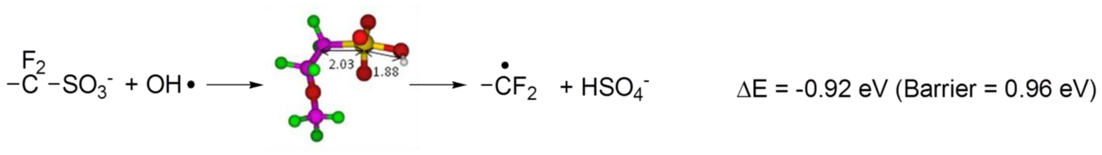

$-CF_2-SO_3^- + OH\bullet \longrightarrow \longrightarrow -\dot{C}F_2 + HSO_4^-$

6B) Epoxide Formation:

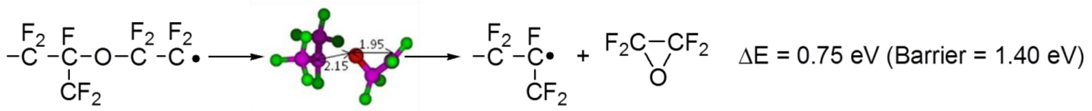

6C) Epoxide Hydrolysis:

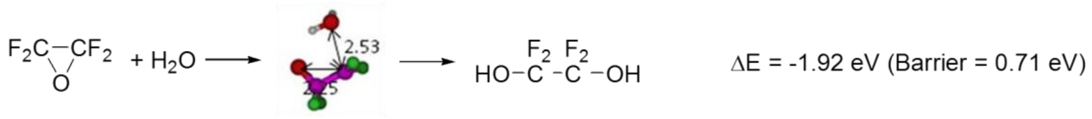

$F_2C(O)CF_2 + H_2O \longrightarrow \longrightarrow HO-CF_2-CF_2-OH$

Figure 6. Proposed degradation mechanism involving OH radical attacking Nafion sulfonic acid group.

7A) H Radical Formation:

7B) H Radical Attack F on Tertiary Carbon:

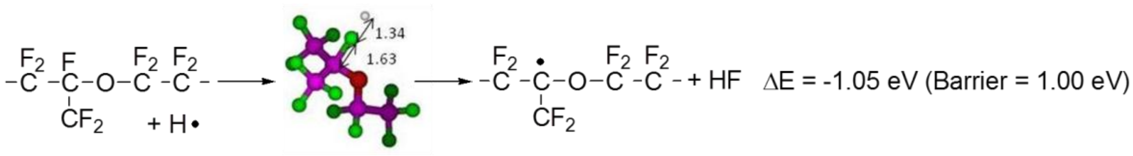

7C) Ketone Formation:

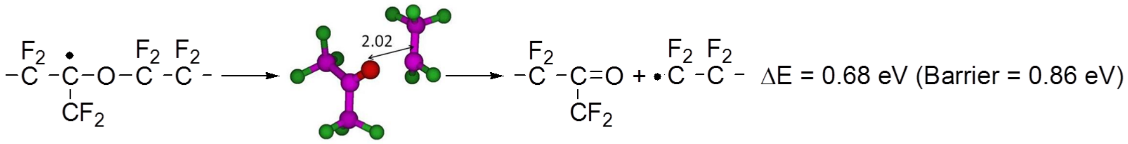

Figure 7. Proposed degradation mechanism involving H radical attacking Nafion sidechain.

REFERENCES

(1) de Bruijn, F. A.; Dam, V. A. T.; Janssen, G. J. M. *Fuel Cells* **2008**, *8*, 3-22.

(2) Teranishi, K.; Kawata, K.; Tsushima, S.; Hirai, S. *Electrochem Solid St* **2006**, *9*, A475-A477.

(3) Endoh, E.; Terazono, S.; Widjaja, H.; Takimoto, Y. *Electrochem Solid St* **2004**, *7*, A209-A211.

(4) Alentiev, A.; Kostina, J.; Bondarenko, G. *Desalination* **2006**, *200*, 32-33.

(5) Curtin, D. E.; Lousenberg, R. D.; Henry, T. J.; Tangeman, P. C.; Tisack, M. E. *J Power Sources* **2004**, *131*, 41-48.

(6) Ghassemzadeh, L.; Kreuer, K. D.; Maier, J.; Muller, K. *J Phys Chem C* **2010**, *114*, 14635-14645.

(7) Chen, C.; Levitin, G.; Hess, D. W.; Fuller, T. F. *J Power Sources* **2007**, *169*, 288-295.

(8) Gummalla, M.; Atrazhev, V. V.; Condit, D.; Cipollini, N.; Madden, T.; Kuzminyh, N. Y.; Weiss, D.; Burlatsky, S. F. *J Electrochem Soc* **2010**, *157*, B1542-B1548.

(9) Madden, T.; Weiss, D.; Cipollini, N.; Condit, D.; Gummalla, M.; Burlatsky, S.; Atrazhev, V. *J Electrochem Soc* **2009**, *156*, B657-B662.

(10) Kitazawa, M.; Nosaka, A. Y.; Nosaka, Y. *Journal of Applied Electrochemistry* **2008**, *38*, 491-496.

(11) Ohguri, N.; Nosaka, A. Y.; Nosaka, Y. *J Power Sources* **2010**, *195*, 4647-4652.

(12) Ohguri, N.; Nosaka, A. Y.; Nosaka, Y. *Electrochem Solid St* **2009**, *12*, B94-B96.

(13) Mittal, V. O.; Kunz, H. R.; Fenton, J. M. *J Electrochem Soc* **2007**, *154*, B652-B656.

(14) Panchenko, A.; Dilger, H.; Kerres, J.; Hein, M.; Ullrich, A.; Kaz, T.; Roduner, E. *Phys Chem Chem Phys* **2004**, *6*, 2891-2894.

(15) Choudhury, B. *"Material Challenges in Proton Exchange Membrane Fuel Cells" (Unpublished Presentation), International Symposium on Material Issues in a Hydrogen Economy*, *Nov. 12-15, 2007*.

(16) Schultz, P. SEQQUEST, Sandia National Laboratory.

(17) Perdew, J. P.; Burke, K.; Ernzerhof, M. *Phys Rev Lett* **1996**, *77*, 3865-3868.

(18) Holst, M. J.; Saied, F. *J Comput Chem* **1995**, *16*, 337-364.

(19) Sha, Y.; Yu, T. H.; Liu, Y.; Merinov, B. V.; Goddard, W. A. *Journal of Physical Chemistry Letters* **2010**, *1*, 856-861.

(20) Becke, A. D. *J Chem Phys* **1993**, *98*, 5648-5652.

(21) Lee, C. T.; Yang, W. T.; Parr, R. G. *Phys Rev B* **1988**, *37*, 785-789.

(22) JAGUAR *7.0, Schrodinger Inc., , Portland, OR*.

(23) Frisch, M. J.; Pople, J. A.; Binkley, J. S. *J Chem Phys* **1984**, *80*, 3265-3269.

(24) Yu, T. H.; Sha, Y.; Merinov, B. V.; Goddard, W. A. *J Phys Chem C* **2010**, *114*, 11527-11533.

(25) Sha, Y.; Yu, T. H.; Merinov, B.; Shirvanian, P.; Goddard, W. A. *Journal of Physical Chemistry Letters* **2011**, *2*, 572-576.

(26) Norskov, J. K.; Rossmeisl, J.; Logadottir, A.; Lindqvist, L.; Kitchin, J. R.; Bligaard, T.; Jonsson, H. *J Phys Chem B* **2004**, *108*, 17886-17892.

(27) Kumar, M.; Paddison, S. J. *Abstract #777, 218th ECS Meeting, 2010 The Electrochemical Society* **2010**.

(28) *DOE 2011 Annual Merit Review Meeting* **2011**, *Durability Improvements Through Degradation Mechanism Studies*.

SYNOPSIS TOC

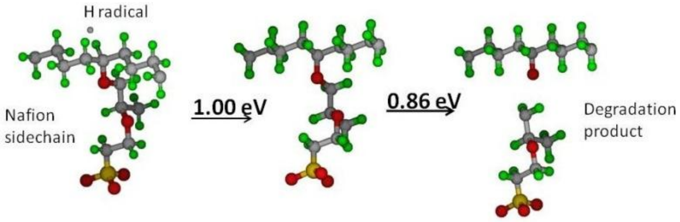

Degradation Mechanism of Nafion Polymer Backbone in PEM Fuel Cell from Quantum Mechanics Calculations

Ted H. Yu,[†] *Wei-Guang Liu,*[†] *Yao Sha,*[†] *Boris V. Merinov,*[†] *Pezhman Shirvanian,*[‡]
*and William A. Goddard III**[,†]
[†]*Materials and Process Simulation Center*

California Institute of Technology, MC 139-74, Pasadena, California 91125

[‡]*Ford Motor Co., Research & Advanced Engineering*

2101 Village Rd, Dearborn, Michigan 48104

1200 E California Blvd MC 139-74, Pasadena, CA 91125 M/S 139-74

Phone: +1 626 395 2731 FAX +1 626 585 0918

* Email: wag@wag.caltech.edu

ABSTRACT: We report results of quantum mechanics (QM) mechanistic studies of Nafion membrane degradation in a polymer electrolyte membrane (PEM) fuel cells. Experiments show that Nafion degradation occurs when Fenton reagents consisting of peroxide radicals attack end groups (-COOH, -CF=CF_2, -CF_2H) that can be formed during the manufacturing process. It has been proposed that after reactions with the end group, peroxide radicals continue to degrade Nafion along the polymer backbone. Studies have also shown that Nafion degradation can occur

along the polymer sidechain starting from the sulfonic acid, -SO_3^-, group. We study the degradation of the Nafion backbone using density functional theory (DFT) in two environments:

3) Fenton Environment: During Fenton degradation experiments, the environment contains high concentrations of peroxide radicals and water, but no O_2 or H_2 gas.
    - Polymer Backbone: We find the barrier for the rate-determining step for different endgroups are: R-COOH = 0.31 eV, R-CF=CF_2 = 0.22 eV, R-CF_2H = 0.09 eV.
    - Polymer Sidechain: We find the barrier for the rate-determing step to be 0.96 eV.
4) Fuel Cell Environment: During PEM fuel cell operations, water, O_2 and H_2 gas are present in the environment. There is only trace concentration of peroxide radicals. Therefore, we limit the degradation mechanism to contain only one peroxide radical reactant.
    - Polymer Backbone: We find the rate-determining barrier to be: R-COOH = 0.59 eV, R-CF=CF_2 = 0.74 eV, R-CF_2H = 0.59 eV.
    - Polymer Sidechain: We find the barrier for the rate-determing step to be 0.68 eV.

From our calculations, we find that Nafion degradation occurs much faster in a Fenton environment than in a fuel cell environment. In a Fenton environment, the barrier for attacking the backbone is lower than attacking the sidechain. In a fuel cell environment, the barriers for attacking the sidechain and backbone are the same.

KEYWORDS: Nafion, degradation, OH radical, heterogeneous catalysis, fuel cell, DFT, Pt Catalyst, ORR, PEMFC

1. **Introduction**

Proton exchange membrane fuel cells (PEMFCs) convert hydrogen to electricity efficiently, with water as their main waste product. A critical component of PEMFC is the proton exchange membrane, Nafion. At its current state, Nafion cannot meet the 5000-10,000 hour operational requirement for automobiles. In order to improve the durability of Nafion, many studies have been performed to determine the mechanism of degradation[1-13]. In a recent paper[14], we showed that Nafion degradation occurs when OH radicals attacks the Nafion sidechain. These OH radicals are generated on the Pt surface during fuel cell operation from HOOH and OOH_{ad} with barriers of 0.53 and 0.76 eV, respectively.

Another possible site for Nafion degradation is the polymer backbone[4,12-13]. While the Teflon chain is very strong, the degradation can be initiated when OH radicals attack endgroups (R-COOH, $R\text{-}CF_2{=}CF_2$, $R\text{-}CF_2H$) which are undesired byproducts of the manufacturing process[4]. Fenton's reagents have been shown to degrade the polymer backbone, and are used to simulate OH radicals in PEM fuel cells. In the presence of Fenton reagents, the polymer backbone degradation is significantly higher than sidechain degradation. By treating Nafion with elemental fluorine to reduce endgroup, the polymer has shown greater chemical stability in a Fenton test[4].

While Fenton's reagent is a useful way to introduce OH radicals into the system, the conditions differ from actual fuel cells. Fenton's reagent is a highly concentrated solution of oxygen radicals while the radical concentration during fuel cell operation was found in experiments to to be ~ 2 μM[8,15]. The concentration of radicals during fuel cell operation is so low that the likelihood of more than one radical participating in a degradation reaction is unlikely. Another key aspect of fuel cell operations is that there are O_2 and H_2 gases not present in Fenton degradation experiments.

2. Computational Methods

QM calculations were carried out using the B3LYP[16-17] hybrid DFT functional with the Jaguar code[18]. Here we used the 6-311g**[19] basis set. All geometries were optimized using the analytic Hessian to determine that the local minima have no negative curvatures (imaginary frequencies), whereas the transition state structures lead to exactly one negative curvature. The vibrational frequencies from the analytic Hessian were used to calculate the zero-point energy corrections at 0 K, which were added to the Jaguar implicit solvation correction and the QM energy ($\Delta[E]$) to obtain the enthalpy at 0 K.

3. Results and Discussion

We examine the possible reaction mechanisms that lead to chemical degradation of the Nafion polymer backbone. We look at the mechanisms starting with three different end groups: R-CF_2H, R-CF=CF_2, and R-COOH. We distinguish between two different reaction environments. In a Fenton environment, the conditions are such that more than one OH radical can participate in the degradation mechanism. In a fuel cell environment, the OH radicals generated on the Pt electrode are so few that we limit the mechanism to have only one OH radical reactant. In addition, there are O_2 and H_2 gas present in a fuel cell environment.

3.1 R-CF_2H end group initiation and chain propagation:

When the end group is R-CF_2H, the OH radical can attack the end group as follows:

Degradation initiation (R-CF_2H): $\text{R-CF}_2\text{H} + \text{OH}^\bullet \rightarrow \text{R-CF}_2^\bullet + \text{H}_2\text{O}$.

The transition state is described in Figure 2A with a barrier of 0.02 eV. After initiation, degradation can propagate along the chain continuously. The way it propagates may differ if it is in a Fenton environment or a fuel cell environment.

Chain propagation in Fenton environment: $\text{R-CF}_2\text{-CF}_2^\bullet + 2\text{OH}^\bullet \rightarrow \text{R-CF}_2\text{-CF}_2\text{OH} + \text{OH}^\bullet \rightarrow \text{R-CF}_2\text{-CF}_2\text{O}^\bullet \rightarrow \text{R-CF}_2^\bullet + \text{O=CF}_2$

The reaction can repeat with the R-$CF_2^\bullet$ product. The other product generated is a carbonyl fluoride and is known to react with water to form 2HF and CO_2[20]. The energetics and barriers are shown in Figure 2B to 2D. Chain propagation in a Fenton environment has a barrier of 0.09 eV. Rather than reacting with OH radical, the $\mathrm{R{-}CF_2{-}CF_2OH}$ can react with $\mathrm{H_2O}$ alternatively in the following water-catalyzed reaction:

$\mathrm{R{-}CF_2{-}CF_2OH + H_2O \rightarrow R{-}CF_2{-}CF{=}O + H_2O + HF}$.

The reaction has a barrier of 0.31 eV and the transition state is shown in figure 3C-ii.

<u>Chain propagation in fuel cell environment:</u> $\mathrm{R{-}CF_2{-}CF_2^\bullet + O_2 + H_2 \rightarrow R{-}CF_2{-}CF_2OO^\bullet + H_2 \rightarrow R{-}CF_2{-}CF_2OH + H^\bullet \rightarrow R{-}CF_2{-}CF_2O^\bullet + H_2O \rightarrow R{-}CF_2^\bullet + O{=}CF_2 + H_2O}$.

The reactions repeat with the $\mathrm{R{-}CF_2^\bullet}$ product. The energetics and barriers are shown in Figure 2E to 2G. The highest barrier is reaction 2F with 0.59 eV. We find that chain propagation has relatively low barrier for both environments but is more difficult in a fuel cell environment than in a Fenton environment.

3.2 R-CF=CF$_2$ end group initiation:

When the end group is $\mathrm{R{-}CF{=}CF_2}$, the OH radical can attack the end group as follows:

<u>Degradation initiation (R-CF=CF$_2$) in Fenton environment:</u> $\mathrm{R{-}CF_2{-}CF{=}CF_2 + 3OH^\bullet \rightarrow R{-}CF_2{-}CFOH{-}CF_2OH + OH^\bullet \rightarrow R{-}CF_2{-}CFO^\bullet{-}CF_2OH + H_2O \rightarrow R{-}CF_2^\bullet + O{=}CFCF_2OH + H_2O}$.

The transition states and energetics are described in Figures 3A to 3D. The $\mathrm{R{-}CF_2^\bullet}$ product can continue to degrade along the polymer backbone as described in the chain propagation in Fenton environment section above. The highest barrier is reaction 3D with 0.22 eV barrier.

<u>Degradation initiation (R-CF=CF$_2$) in fuel cell environment:</u> $\mathrm{R{-}CF_2{-}CF{=}CF_2 + OH^\bullet + O_2 + H_2 \rightarrow R{-}CF_2{-}CF^\bullet{-}CF_2OH + O_2 + H_2 \rightarrow R{-}CF_2{-}CFOO^\bullet{-}CF_2OH + H_2 \rightarrow R{-}CF_2{-}CFOOH{-}CF_2OH + H^\bullet \rightarrow R{-}CF_2{-}CFO^\bullet{-}CF_2OH + H_2O \rightarrow R{-}CF_2^\bullet + O{=}CFCF_2OH + H_2O}$.

The barriers and energetics are described in Figures 3E to 3G. The $\mathrm{R{-}CF_2^\bullet}$ product can continue to degrade along the polymer backbone as described in the chain propagation in fuel cell environment section above. The highest barrier is reaction 3F with barrier of 0.74 eV.

3.3 R-COOH end group initiation:

When the end group is R-COOH, the OH radical can attack the end group as follows:

Degradation initiation ($R\text{-}CF_2\text{-}COOH$): $R\text{-}CF_2\text{-}COOH + OH^\bullet \rightarrow R\text{-}CF_2\text{-}C(OH)_2O^\bullet \rightarrow R\text{-}CF_2^\bullet + O{=}C(OH)_2$.

The transition states and energetics are described in Figures 4A to 4B. The $R\text{-}CF_2^\bullet$ product can continue to degrade along the polymer backbone as described in the chain propagation section above. In a Fenton environment, the highest barrier is reaction 4A with a barrier of 0.31 eV. In a fuel cell environment, the most difficult reaction is during the chain propagation with a barrier of 0.59 eV.

3.4 $R\text{-}SO_3^-$ sidechain initiation:

We compare the energetics of the polymer backbone degradation with side chain degradation. The OH radical can also attack the sulfonic acid group on the polymer side chain as described previously[14]. The sulfonic acid group can be attacked in a Fenton environment as follows:

Degradation initiation ($R\text{-}CF_2\text{-}SO_3^-$) in Fenton environment: $R\text{-}CF_2\text{-}SO_3^- + OH^\bullet \rightarrow R\text{-}CF_2^\bullet + HSO_4^-$

The barrier for this reaction is 0.96 eV with transition state described previously[14]. Or it can attack a protonated sulfonic acid group.

Degradation initiation ($R\text{-}CF_2\text{-}SO_3H$) in Fenton environment: $R\text{-}CF_2\text{-}SO_3H + OH^\bullet \rightarrow R\text{-}CF_2^\bullet + H_2SO_4$

with a barrier of 0.81 eV.

The $R\text{-}CF_2^\bullet$ product can continue to degrade the polymer side chain as described in the chain above.

Degradation initiation ($R\text{-}CF_2\text{-}SO_3^-$) in fuel cell environment: $R\text{-}CF_2\text{-}SO_3^- + OH^\bullet + H_2 \rightarrow R\text{-}CF_2\text{-}SO_3^- + H^\bullet + H_2O \rightarrow R\text{-}CF_2^\bullet + HSO_3^- + H_2O$.

Rather than attacking the sulfonic acid group directly, the $OH^\bullet$ can react with H_2 to form $H^\bullet$ ($\Delta E = -0.59$ eV, barrier = 0.04). The $H^\bullet$ reacts with the sulfonic acid group without barrier to form

HSO_3^-, which is found in fuel cell experiments[2]. The rest of the side chain can degrade along the methods described in a previous paper. The side chain can also continue to degrade with the reaction mechanism described previously on chain propagation in fuel cell environment, with the highest barrier of 0.68 eV.

Table 1 summarizes the highest barrier for degradation for the different end groups and environments. We find that for polymer backbone degradation, the barriers are very low in a Fenton environment with barrier of only 0.09 eV. On the other hand, the side chain degradation is higher and has an initiation barrier of 0.96. Therefore, it is indeed much harder to degrade the Nafion side chain than the polymer backbone in a Fenton environment.

In a fuel cell environment, because there are fewer OH radicals, the barrier for the degradation of the polymer backbone is much higher at 0.59 eV. Also, the barrier for side chain degradation will be easier because of the presence of H_2 gas, which makes reactions with the sulfonate group barrierless. The overall barrier is 0.68 eV, and the critical barrier for degradation for side chain and polymer backbone are comparable. The reason side chain degradation is more common in a fuel cell environment is because the concentration of side chain groups is much higher than that of end groups. This explains why side chain group products are observed in degradation experiments conducted in a fuel cell-like environment[2,12].

Conclusion:

In summary, there is conflicting experimental evidence as to what part of the Nafion chemistry degrades in a fuel cell: the polymer backbone or the side chain. The bulk of the evidence that supports polymer backbone degradation comes from experiments that involve Fenton reagents as the source of OH radical. On the other hand, more recent experimental evidence under more realistic fuel cell conditions supports side chain degradation. We showed in this work that the barrier for polymer backbone degradation is very low (0.09 eV) in an Fenton environment, while the barrier for side chain degradation is difficult (0.96 eV). This would explain why polymer backbone degradation dominates in a Fenton environment. We also showed that under a fuel cell environment, the barriers of side chain and polymer backbone degradation are comparable (0.68 and 0.59 eV, respectively). This is because we took into account that in a fuel cell environment, there is a low concentration of OH radical and that there is H_2 gas, which can give rise to H radicals.

Acknowledgement: This work was supported with funding from the Ford Motor Company.

Table 1. The DFT-predicted reaction barriers for Nafion degradation.

Endgroup		Fenton Environment		Fuel Cell Environment	
		Initiation	Propgation	Initiation	Propagation
Main chain	R-CF_2H	0.02 eV	**0.09 eV**	0.02 eV	**0.59 eV**
	R-CF_2=CF_2	**0.22 eV**	0.09 eV	**0.74 eV**	0.59 eV
	R-COOH	**0.31 eV**	0.09 eV	0.31 eV	**0.59 eV**
Side chain	R-SO_3H	**0.81 eV**	0.33 eV	0	**0.68 eV**
	R-SO_3^-	**0.96 eV**	0.33 eV	0	**0.68 eV**

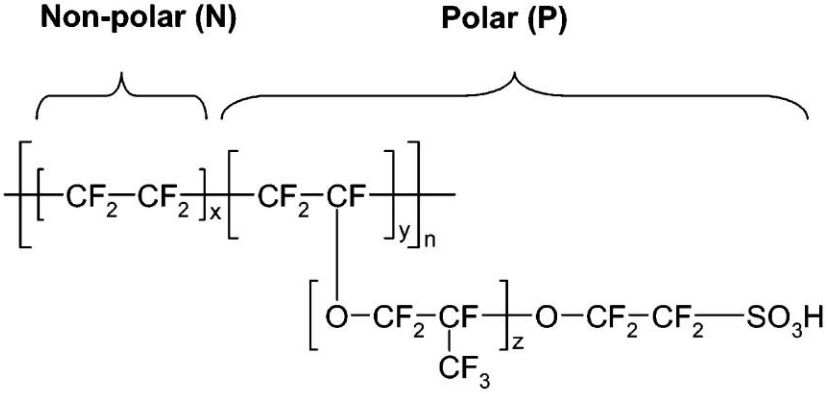

Figure 1. Chemical structure of Nafion. Nafion 117 has an average composition of x = 6.5, y = 1, z = 1. N indicates the nonpolar monomeric units while P indicates the polar monomeric units.

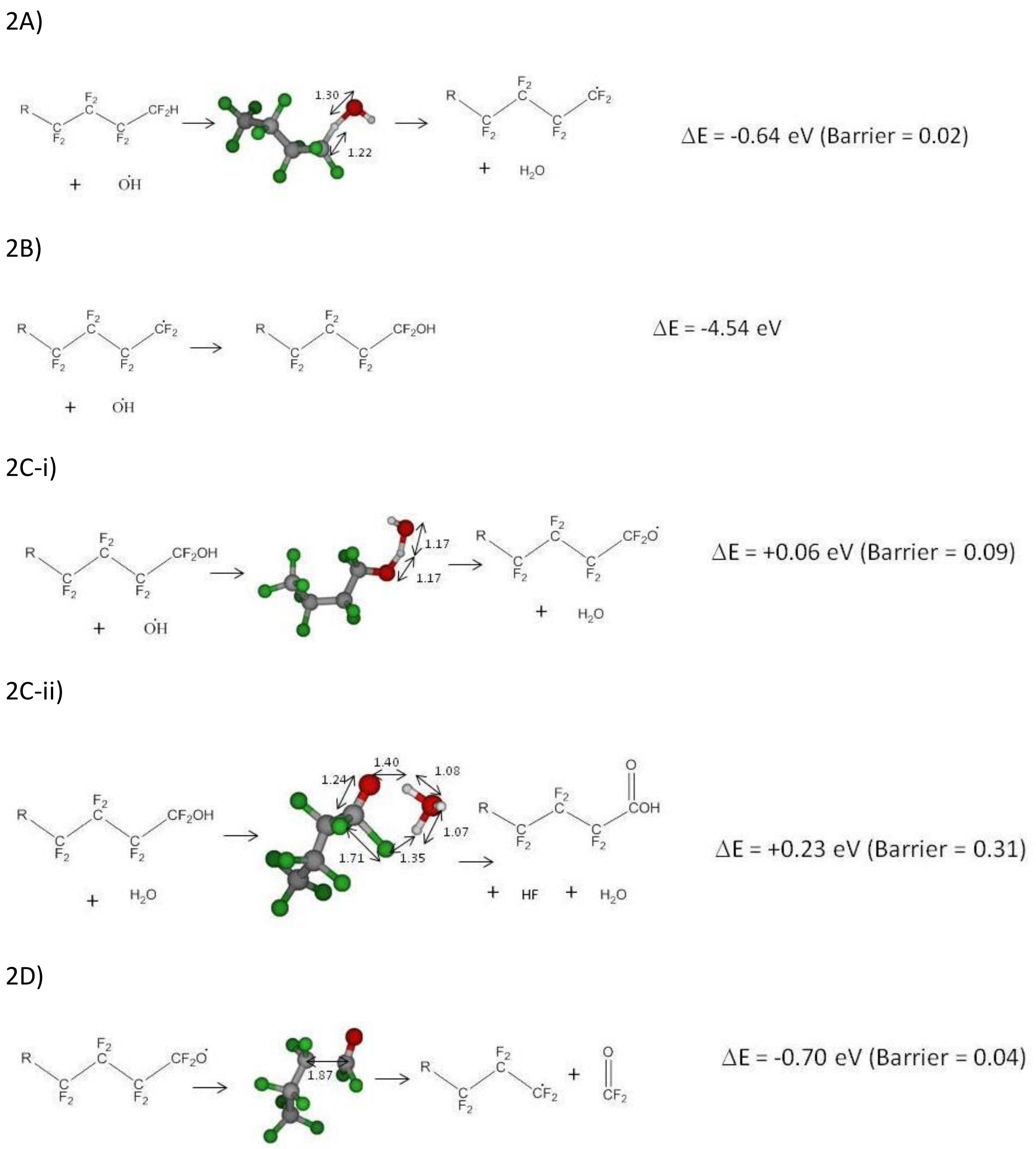

Figure 2A-D: Degradation mechanism in Fenton environment of the polymer backbone from R-CF_2H end group. From 2B, the reaction can react with $OH^\bullet$ proceeding to reaction 2C-i or it can react with H_2O proceeding to reaction 2C-ii. After 2D, the reaction mechanism repeats to 2B. The rate-limiting step is 2C-i with 0.09 eV barrier.

2E)

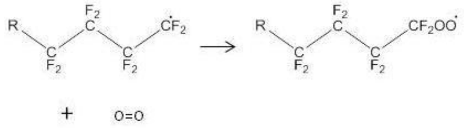

ΔE = -1.15 eV

2F)

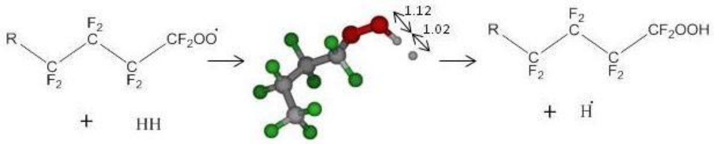

ΔE = +0.44 eV (Barrier = 0.59)

2G)

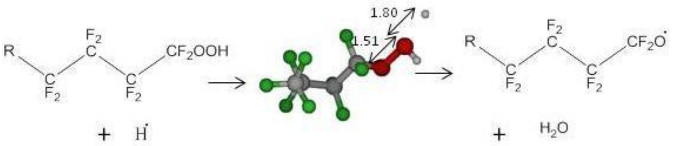

ΔE = -3.15 eV (Barrier = 0.04)

Figure 2E-G: Degradation mechanism in fuel cell environment of the polymer backbone from R-CF_2H end group. The mechanism starts with 2A and proceeds through 2E => 2G. It is followed by reaction 2D. The polymer backbone can continue to grade through 2D =>2G repeatedly. The rate-determining step is 2F with barrier of 0.59 eV.

3A-i)

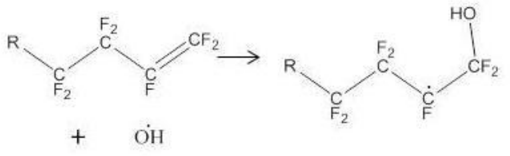

ΔE = -2.18 eV

3A-ii)

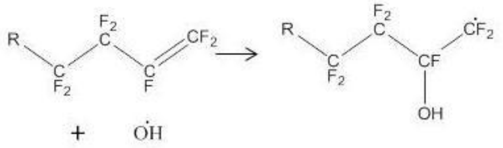

ΔE = -1.75 eV

3B-i)

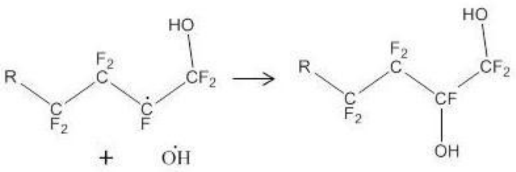

ΔE = -4.12 eV

3B-ii)

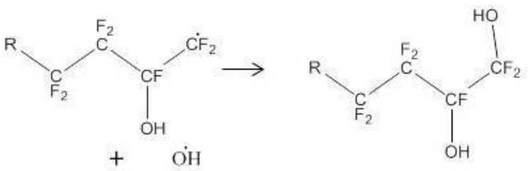

ΔE = -4.55 eV

3C)

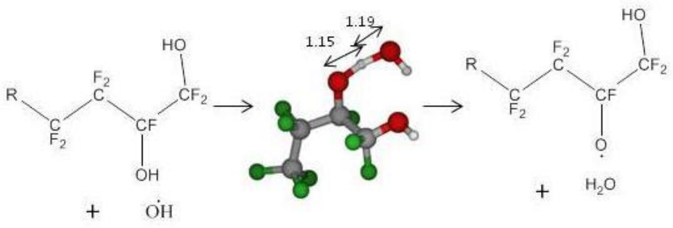

ΔE = -0.30 eV (Barrier = 0.07)

3D)

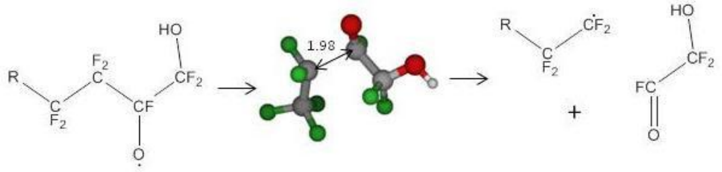

ΔE = -0.36 eV (Barrier = 0.22)

Figure 3A-D: Degradation mechanism in Fenton environment of the polymer backbone from R-$CF=CF_2$ end group. The mechanism proceeds through either steps 3A-i and 3B-i or 3A-ii and 3B-ii. It continues through 3C and 3D. After 3D, the polymer backbone can further degrade and repeat through reactions 2B => 2D. The rate-determining step is 3D with 0.22 eV barrier.

3E)

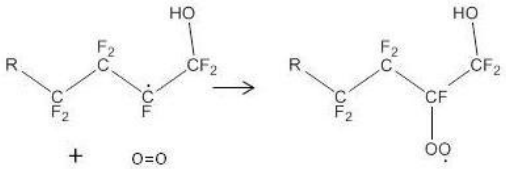

ΔE = -0.83 eV

3F)

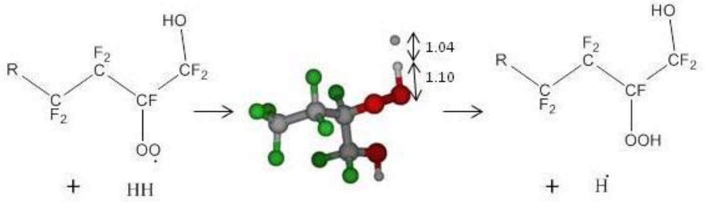

ΔE = 0.60 eV (Barrier = 0.74)

3G)

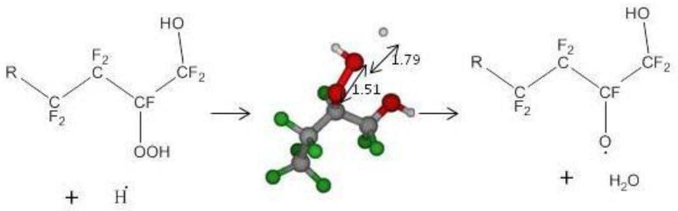

ΔE = -3.56 eV (Barrier = 0.08)

Figure 3E-G: Degradation mechanism in fuel cell environment of the polymer backbone from R-CF=CF_2 end group. The mechanism starts with 3A-i and continues through 3E to 3G, followed by 3D. After 3D, the polymer backbone can further degrade and repeat through reactions 2E => 2G followed by 2D. The rate-determining step is 3F with 0.74 eV barrier.

4A)

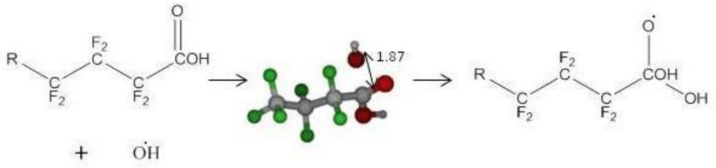

ΔE = -0.10 eV (Barrier = 0.31)

4B)

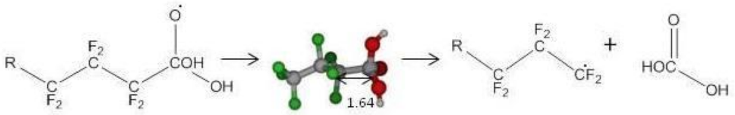

ΔE = -0.95 eV (Barrier = 0.15)

Figure 4: Degradation mechanism of the polymer backbone from R-COOH end group. In a Fenton environment, after 4B, the polymer backbone can continue to degrade through steps 2B to 2D, with 4A as the rate-determining step with a barrier of 0.31 eV. In a fuel cell environment, after 4B, the polymer backbone can continue to degrade through steps 2E-2G, followed by 2D, with 2F as the rate determining step and a barrier of 0.59 eV.

REFERENCES:

(1) de Bruijn, F. A.; Dam, V. A. T.; Janssen, G. J. M. *Fuel Cells* **2008**, *8*, 3.

(2) Teranishi, K.; Kawata, K.; Tsushima, S.; Hirai, S. *Electrochem Solid St* **2006**, *9*, A475.

(3) Endoh, E.; Terazono, S.; Widjaja, H.; Takimoto, Y. *Electrochem Solid St* **2004**, *7*, A209.

(4) Curtin, D. E.; Lousenberg, R. D.; Henry, T. J.; Tangeman, P. C.; Tisack, M. E. *J Power Sources* **2004**, *131*, 41.

(5) Gummalla, M.; Atrazhev, V. V.; Condit, D.; Cipollini, N.; Madden, T.; Kuzminyh, N. Y.; Weiss, D.; Burlatsky, S. F. *J Electrochem Soc* **2010**, *157*, B1542.

(6) Madden, T.; Weiss, D.; Cipollini, N.; Condit, D.; Gummalla, M.; Burlatsky, S.; Atrazhev, V. *J Electrochem Soc* **2009**, *156*, B657.

(7) Kitazawa, M.; Nosaka, A. Y.; Nosaka, Y. *Journal of Applied Electrochemistry* **2008**, *38*, 491.

(8) Ohguri, N.; Nosaka, A. Y.; Nosaka, Y. *J Power Sources* **2010**, *195*, 4647.

(9) Mittal, V. O.; Kunz, H. R.; Fenton, J. M. *J Electrochem Soc* **2007**, *154*, B652.

(10) Panchenko, A.; Dilger, H.; Kerres, J.; Hein, M.; Ullrich, A.; Kaz, T.; Roduner, E. *Phys Chem Chem Phys* **2004**, *6*, 2891.

(11) Chen, C.; Levitin, G.; Hess, D. W.; Fuller, T. F. *J Power Sources* **2007**, *169*, 288.

(12) Ghassemzadeh, L.; Kreuer, K. D.; Maier, J.; Muller, K. *J Phys Chem C* **2010**, *114*, 14635.

(13) Alentiev, A.; Kostina, J.; Bondarenko, G. *Desalination* **2006**, *200*, 32.

(14) Yu, T. H.; Sha, Y.; Liu, W. G.; Merinov, B. V.; Shirvanian, P.; Goddard, W. A. *J Am Chem Soc* **2011**, *133*, 19857.

(15) Ohguri, N.; Nosaka, A. Y.; Nosaka, Y. *Electrochem Solid St* **2009**, *12*, B94.

(16) Becke, A. D. *J Chem Phys* **1993**, *98*, 5648.

(17) Lee, C. T.; Yang, W. T.; Parr, R. G. *Phys Rev B* **1988**, *37*, 785.

(18) JAGUAR *7.0, Schrodinger Inc., , Portland, OR*.

(19) Frisch, M. J.; Pople, J. A.; Binkley, J. S. *J Chem Phys* **1984**, *80*, 3265.

(20) Ryan, T. A.; Ryan, C.; Seddon, E. A.; Seddon, K. R. *Phosgene and Related Carbonyl Halides*; Elsevier Science: New York, 1996.

Surface Segregation of Pt Alloys with Adsorbed Oxygen Species Predicted from Quantum Mechanics

Ted H. Yu, Yao Sha, Boris V. Merinov, and William A. Goddard III[1]

Materials and Process Simulation Center (139-74)

California Institute of Technology, Pasadena, California 91125

Abstract

Based on the hypothesis that alloy catalysts for the oxygen reduction reaction (ORR) at fuel cell cathodes should have a surface layer that is noble (e.g. Pt, Pd, or Rh) while the second layer should have 50% of more electropositive metal to decrease the critical barriers for ORR, we used quantum mechanics (QM) to examine 80 binary alloys of composition Y_3X where Y=Pt, Pd, or Rh and X is any of the three rows of transition metals (columns 3-11). This study identified X=Re (best), W, Os, Mo, Ru, Ir, Tc, Rh, Co, Ta, Nb, and Ni as good segregating alloys for Pd_3X. Of these we selected Pd_3W as particularly promising since it is known experimentally to form an ordered alloy and was found to have a desirable d-band center.

We then examined the critical barriers for various steps of the ORR with Pd_3W and compared them to the analogous barriers for Pt, Pt_3Co, and Pd. These results suggest that Pd_3W will exhibit ORR properties dramatically improved over pure Pd and close to that of pure Pt. The cost of Pd_3W is ~ 6 times less than pure Pt, suggesting that Pd_3W catalysts might lead to significant decreases in catalyst cost, while maintaining performance.

Keywords: Segregation, Pd-based alloys, ORR non-Pt catalysts, DFT

---

[1] Corresponding author: William A. Goddard III, e-mail address: wag@wag.caltech.edu

Introduction

The major motivation for this study is to find dramatically less expensive cathode catalysts for polymer electrolyte membrane fuel cell (PEMFC) than pure Pt, while maintaining or improving the high performance for the oxygen reduction reaction (ORR) exhibited by Pt. An obvious candidate would be to replace Pt with Pd, which would decrease the cost by a factor of 5[1]. However, the performance of Pd for ORR is dramatically worse than for Pt[2]. Thus we wanted to explore whether there might be alloys[3,27] of Pd that could achieve higher performance. Here we were stimulated by the observation that Pt_3Co and Pt_3Ni have enhanced ORR catalytic activity over pure Pt[4,54] and also lead to a unique segregation in which the first layer is 100% Pt while the second layer is ~ 50% base metal,[5,40] (Co or Ni). Thus although the second layer is completely covered by the surface layer, it enhances the ORR of the surface layer (pure Pt), while the noble metal overlayer helps protect the electropositive metal from oxidation. Even so, the Co and Ni alloying elements tend to become depleted from the surface under FC operating conditions.[6]

In order to determine new alloy candidates for PEMFC cathodes, we considered 80 binary alloys of composition Y_3X, where Y=Pt, Pd, or Rh and X is any of the three rows of transition metals (columns 3-11). Our strategy was first to find all binary alloys in which there is a strong segregation of the noble metal to the surface (100%) with a concomitant enrichment of the base metal in the second layer (50%)[7-10]. Here we used QM calculations (density functional theory (DFT) of the PBE[12] flavor) on a 4-layer slab to determine these energy differences. These studies correctly identified that Pt_3Co (0.50 eV) and Pt_3Ni (0.46 eV) would have this segregation property while Pt_3Fe (0.11 eV) would not, as observed from LEED experiments[5]. Of these systems with a strong preference for segregation, we selected the ones known to have a Y_3X intermetallic phase as the most likely to lead to a stable, noble metal, protective surface. We identified Pd_3W as particularly promising.

Having selected the systems with the best surface segregation, we then used QM to examine the reaction pathways for ORR, comparing Pd_3W with bulk Pd and bulk Pt and also with the

Pt_3Co and Pt_3Ni cases. Pt_3Co and Pt_3Ni are better than Pt, as observed; Pd is much worse than Pt, as observed. We find that Pd_3W has a performance much better than Pd, suggesting that it is an excellent candidate for experimental study.

Computational Methods

Periodic quantum mechanics (QM) calculations were carried out with the SeqQuest code,[11] which employs Gaussian basis functions rather than the plane wave basis often used in periodic systems. We used the Perdew-Becke-Ernzerhof (PBE) flavor[12] of DFT in the generalized gradient approximation (GGA)[13,14] and allowed the up-spin orbitals to be optimized independently of the down spin orbitals (spin unrestricted DFT). All calculations were performed with spin optimization.

Angular-momentum-projected norm-conserving nonlocal effective core potentials[15,36] (pseudopotentials) were used to replace the core electrons. Thus, the Pt atom was described with 16 explicit electrons (six 5p, one 6s, and nine 5d), the Pd atom with 16 (six 4p, one 5s, and nine 4d), and the Rh atom with 15 (six 4p, one 5s, and eight 4d). The Gaussian basis functions were contracted to the double zeta plus polarization level from calculations on the most stable unit cell of the pure elements. The real space grid density was 5 points per Angstrom, while the reciprocal space grid was 5×5×0 for slab calculations.

For the three-dimensional structure we assumed the $L1_2$ cubic unit cell with the base metal X at the corner and the noble metal Y centered on the faces, and then we optimized the lattice parameter (tabulated in the supporting information (SI), Table S1). The reciprocal space grid was 12×12×12. The bulk spin is tabulated in Table S3.

To describe the surface segregation and ORR, we assumed the closest packed (111) surface and used the 2 × 2 hexagonal periodic unit cell in the *a* and *b* directions based on the bulk lattice constants, while allowing 4 independent metal atoms per layer. For calculating segregation energies, we considered the four-layer slab (Figure 1), in which the top two layers are allowed to relax, but the bottom two layers were fixed with the atoms in their bulk structure positions. The spin of the four layer slabs is tabulated in Table S3. The five and six layer slabs were also calculated for some cases with the top two layers relaxed and remaining layers fixed. The segregation energy was found to be comparable for the four, five, and six layer cases, indicating that the four layer case is sufficient (tabulated in supporting information (SI), Table S2). A vertical mirror symmetry plane was added perpendicular to the layers in all cases. To determine the surface d-band center of the alloys, density of state module of the Seqquest code was employed[11].

To calculate the energetics of 2nd layer enrichment of 3-d base atoms, we used 2X2 five layer slabs (Figure 3) with the 3rd layer fixed. The lattice parameter used was the average lattice parameter of the two alloys being compared. For example, to compare Pt_3Co and Pt_3Fe, the average of the calculated FCC lattice parameter of the two was used in the comparison. Otherwise, the same parameters were used as those of the 4-layer slabs in the segregation energy calculations.

To calculate the energy surface and barrier for the various ORR reactions, we used a three-layer slab, in which the top two layers were allowed to relax but the bottom layer was fixed. Due to the use of Gaussian basis functions, it was not necessary to add an artificial vacuum surface as often done with plane wave basis sets.[16]

Water plays an important role in PEMFCs, being part of the PEM and present in both the fuel and oxidant. Thus solvation by the water likely contributes to the energetics and rates of the reactions. We estimate this solvent effect by the Poisson-Boltzmann model using Adaptive Poisson-Boltzmann Solver (APBS)[17,18] (a solvent radius of 1.4 Å and a dielectric constant of 78 were applied). These calculations were carried out using the CMDF[19] module to obtain the free energy surface for the ORR.

Results and Discussion

Segregation. Table 1 shows (for Pd_3X, and Pt_3X, Rh_3X) the calculated segregation energies for having a pure noble metal, Y, in the top layer with 50% of X in the second layer (and 25% in subsequent layers) termed “surface segregated”, versus the uniform distribution of 25% X in every layer “surface uniform”. (Here positive indicates segregation is favorable.) Figure 1a-c shows this graphically.

Validations of our calculations can be made by comparing with experimental segregation results. Pd-Co[38], Pd-Ni[52], Pt-Fe[5,33,40], Pt-Co[5,30], Pt-Ni[5,41], Pt-Cu[51], Pt-Ir[42], Pt-Ru[44,46], Pt-Mo[45], and Pt-Rh[5,46,47] alloys have been shown to be Pt segregating at the surface, where the % of Pt is higher than that of the bulk concentration, corresponding to the positive segregation energy calculated in this study. In addition to the top layer being enriched in noble metal, Pd-Ni[52], Pt-Co[5], Pt-Ni[5,41], Pt-Cu[51], Pt-Rh[5,46,47], and Pt-Ru[46] were shown experimentally to have 2nd layer enrichment of base metal by low energy electron diffraction (LEED), medium energy ion spectroscopy (MEIS) or depth profiling, also corresponding to their positive segregation energy. From our calculations, a negative segregation energy implies segregation of the base metal to the surface. Experiments have been conducted on Pd-Au[50], Pd-Ag[49,50], and Pt-Au[43,46,48] that show segregation of the base metal to the surface corresponding to the negative segregation energy calculated in this study.

Further validation of our calculations is given in Figure 2, where we compare the theoretical segregation energy of Pt_3Fe, Pt_3Co, and Pt_3Ni with the degree of surface segregation found in a low energy electron diffraction (LEED) experiment by Gauthier[5]. For Pt_3Co and Pt_3Ni, LEED experiments show that the surface layer concentration is nearly 100% Pt, while the second layer is about 50% Co or Ni, and the third is nearly 75% Pt[5]. Consistent with this, the theory predicts that this segregated structure is more stable than the uniform by 0.50 and 0.46 eV for X = Co and Ni, respectively. In contrast the LEED shows very little 2nd-layer Fe enrichment in Pt_3Fe, which is consistent with the much smaller segregation energies (0.10 eV) predicted for Fe and other 3d metals.

In comparison with previous theoretical studies of surface segregation in transition metal alloys[7-9], a comprehensive early study[7] of surface segregation energies of 1 X 1 surfaces cover almost all combinations of bimetallic transition metal alloys. Our 2 X 2 layer study results differ in some cases, as expected, because the unit cells differ. Studying segregation in 2 X 2 layer slabs allow us to compare layers with mixed concentration per layer (0%, 25%, 50%, 75%, 100%), whereas the 1 X 1 comparison study can only compare 0% or 100%. A similar study of 2 X 2 5-layered surface structures of Pt_3X alloys (but not Rh_3X and Pd_3X alloys) comparing the "surface segregated" and "surface uniform" cases[9] has the same qualitative result as the Pt alloy cases in this study (the segregation energies have the same signs). Quantitatively, the one case where the results differ significantly is for Pt_3Fe where the reference[9] shows segregation energy of (0.41 eV[2]). In this work, the four-, five-, six-layer studies (see Table 1, 2 and S2) show small positive segregation energy in Pt_3Fe (0.10 - 0.12 eV). Otherwise, the Pt results in this study are fairly consistent with the results from Balbuena[9]. Other than the cases when the segregation energies are very large (Pt_3Re and Pt_3Mo) and the Pt_3Fe case, the values compare well and are within 0.15 eV difference.

The reason for the difference in Pt_3Fe segregation energy between this study and Balbuena's[9] can be due to small differences in the DFT calculation. Both studies use the PBE[12] flavor of DFT, but the difference could be due the smaller core electrons in the present work. We treat 16 valence electrons for Pt and 14 valence electrons for Fe, while VASP uses 10 valence electrons for Pt and 8 valence electrons for Fe. In this case, our results are more accurate. We use Gaussian basis sets rather than plane wave basis sets, which allow very accurate slab calculations.

Table 1a-c identifies even more strongly segregating base atoms for Pt, including Re (best), W, Os, Tc, Mo, Ru, and Ir (in decreasing segregation energy). More importantly we identified a

---

[2] The reference[9] displays the energy as -0.41 rather than +0.41.

number of base atom cases for Pd favoring a strong tendency for segregation: Re (best), W, Os, Mo, Ru, Ir, Tc, Rh, Co, Ta, Nb, and Ni in decreasing segregation energy (Table 1 and Figure 1). In general, the segregation energy of Pd and Pt alloys are similar for the same base atoms. But in all cases, Rh alloys lead to lower segregation energies than Pd and Pt alloys for the same base metal. The best base atoms for high segregation energy are metals with high cohesive energy, such as Re, W, Os, and Mo.

Among the Pd_3X alloys with strong segregation energies[20], only Pd_3W is known to have a stable phase at this 3:1 composition[21], as observed for Pt_3Co and Pt_3Ni alloys. We expect that such systems with a stable ordered phase at 3:1 ratio are more likely to be ordered. This, plus the relative abundance of W, makes Pd_3W a most promising candidate for investigating the catalytic properties. In addition, we consider Pd_3Ta, Pd_3V, and Pd_3Nb with their moderately positive segregation energy (comparable to Pt_3Co and Pt_3Ni) and stable 3:1 phase as other good candidates[20,22].

2nd-Layer Enrichment of Base Metal.

In Figure 3, calculations compare the 2nd-layer enrichment of base metals in a 3:1 alloy. Because the segregation energy calculated in the previous section is a measure of both the tendency for an alloy to have 100% noble metal at the surface and enrichment of 50% base metal at the 2nd layer, we perform energy calculations that measure only the 2nd-layer effects. We are motivated by the experimental findings that Pt_3Ni, Pt_3Co, Pt_3Fe, and Pt_3Ti have nearly 100% Pt[5,30,33,37,40,41] on the surface, while the theoretical segregation energies vary dramatically (0.46 eV, 0.50 eV, 0.11 eV, -0.67 eV, respectively). The five-layer cells for the calculations and the energetic results are shown in Figure 3. The calculations show that in terms of 2nd-layer enrichment of base metals the order is: $Pt_3Ni > Pt_3Co > Pt_3Fe > Pt_3Ti$. Pt_3Ti has a very large energetic penalty to be enriched in Ti in the second layer. Compared to Pt_3Fe, Pt_3Co, and Pt_3Ni, the penalty for 2nd-layer enrichment is ~1.7 eV for a 2 X 2 cell. This would explain why the segregation energy of Pt_3Ti is negative (-0.67), even though experiments[37] show that the surface of Pt_3Ti is nearly 100% Pt, and confirms what was previously theorized[9]. Pt_3Fe has a moderate 2^{nd}-layer base metal enrichment penalty compared with Pt_3Co and Pt_3Ni (0.16 and 0.26 eV, respectively). The moderate penalty of Pt_3Fe is explained well by both experimental results[5] and theory (Figure 2). The 2^{nd}-layer concentration of Pt in Pt_3Fe, Pt_3Co, and Pt_3Ni is 88%, 48%, and 30% Pt, respectively. As such, Pt_3Fe has a 2^{nd} layer that is depleted in base metal (12% Fe < 25% Fe in bulk), whereas both Pt_3Co and Pt_3Ni are enriched in base metal. In summary, the segregation energy of alloys that experiments have shown to be nearly 100% Pt at the surface, differ because of the energetic penalties associated with having 50% base metal in the 2^{nd} layer.

d-Band Centers of Alloys. For alloy catalysts, a simple model was proposed that correlates the d-band center of the surface metal to catalytic activity[31]. Using this model, adsorption energy of simple adsorbates (O, CO, H) were found to correlate well with the center of the surface metal d-band[31-32]. We report the d-band center of the surface layer of the surface segregated (100-50-75-75% noble metal) case in Table 2. We see that the most negative d-band-shifting base atom for Pd is Ta (-2.44 eV) followed by W (-2.39 eV), making them the non-Pt alloys with d-bands closest to Pt in this study. The d-band centers of Rh alloys are more positive than both Pd and Pt alloys. In comparison, the d-band center for notable catalysts include pure Pt (-2.47 eV), Pt_3Co (-2.75) and Pt_3Ni (-2.70). As it turns out, Pd_3W has the second most negative d-band center, amongst the Pd alloys studied, making it a promising alloy for further study.

Reaction pathways for ORR. Two general types of pathways have been suggested for ORR[8,34,35]; one involving O_2 dissociation into 2 atomic oxygen and another involving association of O2 with H to form OOH. .

O_2 dissociation mechanism:

$$O_2 \xrightarrow[\text{i}]{} 2O \xrightarrow[\text{ii}]{2H} 2OH \xrightarrow[\text{iii}]{2H} 2H_2O \quad (1),$$

proceeds via an initial O_2 dissociation, O_{2ad} => $2O_{ad}$, followed by OH formation H + O_{ad} => OH_{ad}, and finally H_2O formation H + OH_{ad} => H_2O_{ad}

OOH association mechanism:

$$O_2 \underset{iv}{\xrightarrow{H}} OOH \underset{v}{\xrightarrow{}} O + OH \underset{ii}{\xrightarrow{H}} 2OH \underset{iii}{\xrightarrow{2H}} 2H_2O \quad (2),$$

starts with activation of the O_{2ad} by H to form OOH_{ad}, H + O_{2ad} => OOH_{ad}, followed by O-O bond cleavage, OOH_{ad} => O_{ad} + OH_{ad}, and then formation of OH and H_2O by adding H.

Theoretical models have suggested that the O_2 dissociation mechanisms have higher critical barriers and the OOH association mechanism is favorable[24,35]. In contrast, experiments have shown that O_2 dissociates quite readily in water environments, suggesting the barrier is lower than what has been theoretically calculated[39]. Thus, there is no consensus on the exact mechanism of ORR, justifying a need for further study. To simplify modeling, we assume that the H is adsorbed on the Pt surface, but of course, it might be delivered directly by the H_3O^+ in solution. This is likely most important for the OH formation step. The barriers to these reactions have been calculated at various potentials including fuel cell operating potentials[24,26,34,35]. There is no consensus on a method to calculate barriers of reactions of H_3O^+ with adsorbed ORR species. In a pioneering paper, Norskov and co-workers[35] computed the energetics but not the barriers of reactions of hydronium with ORR species. Another study[26] was devoted to estimating the barrier of OO_{ad} + H_3O^+ => H_2O + OOH_{ad} in water, and these barriers were calculated with reference to H_2 in the fuel cell anode. In another approach, Kasai et al.[53] computed hydronium barriers with reference to vacuum at zero potential and found that in this context, these ORR reactions have no barriers. Although each approach has its merit, there are assumptions made to simplify the reaction so that the reaction pathway involving hydronium can be estimated. In the following study, zero potential barriers were calculated with hydrogen adsorbed on the metal surface[8,19]. An implicit solvent effect was added to the calculations to simulate the effects of water. These barriers will provide insights into the difference in the reaction barriers as we vary the metal and alloys, and provide benchmarks for which alloys/metals are better.

These various barriers are shown in Figure 4 for Pt, Pt_3Co, Pd, and Pd_3W.

Implications for ORR. Figure 4 shows dramatic differences between Pt, Pt_3Co, Pd, and Pd_3W in terms of the reaction barriers for the various fundamental steps. For example, the direct OH formation has a low barrier for Pd and Pd_3W (0.70 and 0.54 eV), whereas this barrier is high for Pt_3Co and Pt (1.26 and 1.33 eV). However, for Pt and Pt_3Co the alternative mechanism of OOH formation provides a low barrier of 0.35 and 48 eV, respectively.

Also, the H_2O formation barrier, H_{ad} + OH_{ad} => H_2O, is much lower for Pd_3W (0.69 eV) than for pure Pd (0.90 eV). Since this is the rate-determining step for these cases, the Pd_3W catalysis should be much better than pure Pd.

Considering that OH is formed by H_{ad} adding to O_{ad}, this would be relatively favorable for Pd and Pd_3W (0.7 and 0.54 eV, respectively) but very unfavorable for Pt and Pt_3Co (1.33 and 1.26 eV, respectively). However, in a PEMFC, the OH formation can result by protonation of O_{ad} by solvent H_3O^+.

Thus, we consider that the rate-determining step for ORR on Pt is adding H_{ad} to OH_{ad} to form H_2O_{ad}, with a barrier of 0.51 eV for Pt and 0.48 eV for Pt_3Co. Note, that this barrier is 0.90 eV for Pd, significantly higher than that for pure Pt, 0.51 eV. However, for the Pd_3W alloy this barrier is 0.69 eV, dramatically improved over the barrier of 0.90 eV for pure Pd.

Comparison to experiment. As we carried out this work we were unaware of any previous studies on Pd-W catalysts for fuel cells. Indeed, based on our results, Debbie Myers of Argonne National Labs in December 2008 initiated a series of experiments to validate our predictions.

However, upon completion of our manuscript, an experimental paper showing that alloying of Pd with W enhances the catalytic activity for ORR compared to pure Pd was published[27]. According to the experimental results, nanoparticles with the composition $Pd_{95}W_5$ exhibit the maximum activity for the ORR, which is nearly as good as the activity of Pt. Our study for the infinite slab suggests that the best composition would be Pd_3W[3]. A difference here is that the experiment deals with carbon supported nanoparticles having the $Pd_{100-x}W_x$ ($0 \leq x \leq 30$) face-centered, cubic solid solutions, whereas our calculations were carried out on the Pd_3W (111) surface using the two-dimensional infinite slabs.

No electrochemical data were presented or discussed in Ref. 27 for $Pd_{70}W_{30}$ (which is close in composition to Pd_3W). Clearly further investigations of these alloys, including Pd_3W, is in order, particularly, their catalytic activity for ORR. These computational results on Pd_3W suggest that Pd_3Mo should also be segregated and effective for ORR. Indeed experiments indicate that Pd-Mo is also a good ORR catalyst[27].

Summary and Conclusion

We examined 80 binary alloys with composition Y_3X to find 12 systems with a strong driving force to segregate with the noble metal Y at the surface and the more electropositive metal X preferring the 2nd layer, which we expect to provide good ORR performance simultaneous with stability under oxidation conditions. We compared our segregation results with experimental LEED results and found that they agree well. We further compared the 2nd-layer enrichment of 3d base atoms in Pt alloys and found that some alloys have a higher energy penalty to be enriched in the 2nd layer, which leads to a negative segregation energy. We find that the 2nd-layer enrichment of 3d atom is such that Pt3Ni (high) > Pt3Co (high) > Pt3Fe (moderate) > Pt3Ti (low), agreeing well with experimental results. We also examined surface d-band centers of the these alloys with a 100% Pt 1st layer and 50% Pt 2nd layer and found Pd_3Ta and Pd_3W to be non-Pt alloys with d-band centers closest to Pt. From this set we examined the ORR performance on the Pd_3W system, which we considered the best candidate. Indeed we predict much better performance than pure Pd, perhaps close to that of pure Pt. Since the cost of this material[1] would

---

[3] There is a report on the Pd-W phase diagram[21] characterizing the Pd_3W phase as hexagonal. This seems surprising since Pd is fcc cubic, while W is bcc cubic. Also experimental results on Pd-W alloys find that $Pd_{0.6}W_{0.4}$ and $Pd_{3.2}W_{0.8}$ are both fcc, while $Pd_{0.046}W_{0.954}$ is bcc.[28,29]

be ~ 1/6 that of pure Pt, we suggest experimental examination of catalysts with compositions near those of Pd_3W. Moreover such systems should be more stable under the oxidizing conditions of the fuel cell. We found a number of good candidates with alloys of W, Ta, V, and Nb, particularly favorable. We chose to focus first on Pd_3W, since it is a known intermetallic compound and has a d-band center close to Pt.

We examined the various reaction steps for ORR, with the hope that the rate for Pd_3W would be substantially better than Pd, just as Pt_3Co is better than Pt. Indeed we found Pd_3W to have substantially lower barriers than Pd, nearly as good as Pt and Pt_3Co. If Pd_3W turns out to be less sensitive to leaching under oxidative conditions, as suggested by our calculations, its lower cost (by a factor of 6) could make it a practical alternative to Pt for PEM fuel cells.

The rate-determining step for both Pd and Pd_3W is the water formation, but the corresponding barrier is noticeably lower for the Pd_3W alloy, 0.69 eV, compared to that for pure Pd, 0.90 eV.

Due to the favorable segregation energy and overall energetics which are similar to those of Pt, Pd_3W can be considered as a promising candidate for further theoretical and experimental investigations of its catalytic properties. According to our computational data, Pd_3Ta, Pd_3V, and Pd_3Nb are other promising candidates for further review.

Acknowledgement. This work was supported by the US Department of Energy under grant DE-AC02-06CH11357. The facilities of the Materials and Process Simulation Center (MSC) used in this study were established with grants from DURIP-ONR, DURIP-ARO, and NSF-MRI. Additional support for fuel cell research in the MSC is provided by Ford Scientific Research Labs. We thank Drs. Deborah Meyers and Gerald Voecks, and Prof. Clemens Heske for useful discussions.

Supporting Information Available: Optimized lattice parameters for various Y_3X metal alloys, calculated segregation energies shown graphically for Pt_3X and Rh_3X. Segregation energy of 4, 5, and 6 layer slabs to verify that the 4 layer slab model is sufficient. This material is available free of charge via the Internet at http://pubs.acs.org.

References and Notes

(1) All metal quotes, http://www.kitco.com/market/

(2) Kinoshita, K. *Electrochemical Oxygen Technology*, Wiley, New York, USA **1992**, p. 170.

(3) Fernandez, J.L.; Raghuveer, V.; Arumugam, Manthiram; Bard, A.J. *J. Am. Chem. Soc.* **2005,** *127*, 13100-13101.

(4) Markovic, N.M.; Ross, P.N. *Surface Science Report* **2002**, *45*, 121-229.

(5) Gauthier, Y. *Surface Review and Letters* **1996**, *3*, 1663-1689.

(6) Watanabe, M.; Tsurumi, K.; Mizukami, T.; Nakamura, T.; Stonehart, P. *J. Electrochem. Soc.* **1994,** *141*, 2659-2668.

(7) Ruban, A.V.; Skriver, H.L.; Norskov, J.K. *Phys. Rev. B.* **1998,** *59*, 15990-16000

(8) Jacob, T.; Goddard III, W.A. *Chem. Phys. Chem.* **2006**, *7*, 992-1005.

(9) Ma, Y.; Balbuena, P.B. *Surface Science* **2008**, *602*, 107-113.

(10) Nilekar A.U. ; Ruban A.V. ; Mavrikakis M. *Surface Science* **2009**, *603*, 91-96.

(11) (a) Schultz, P. SEQQUEST, Sandia National Laboratories, http://dft.sandia.gov/Quest/. (b) Feibelman, P.J. *Phys. Rev. B* **1987**, *35*, 2626-2646. (c) SEQQUEST post-analysis code by Arthur Edwards, http://dft.sandia.gov/Quest/SeqQ_Kudos.html

(12) Perdew, J.P.; Burke, K.; Ernzerhof, M. *Phys. Rev. Lett.* **1996**, *77*, 3865-3868.

(13) Ceperley, D.M.; Alder, B.J. *Phys. Rev. Lett.* **1980**, *45*, 566-569.

(14) Perdew, J.P.; Zunger, A. *Phys. Rev. B* **1981**, *23*, 5048-5079.

(15) Goddard, W.A. *Phys. Rev.* **1968**, *174*, 659-662.

(16) Kresse, G.; Furthmueller, J. *Phys. Rev. B* **1996**, *54*, 11169-11186.

(17) Baker, N.; Sept, D.; Joseph, S.; Holst, M.; McCammon, J. *Proceedings of the National Academy of Sciences* **2001**, 181342398.

(18) Holst, M.; Saied, F. *Journal of Computational Chemistry* **1995**, *16*, 337-364.

(19) Sha, Y.; Yu, T.H.; Liu, Y.; Merinov, B.V.; Goddard, W.A.; *J. Phys. Chem. Lett.* **2010,** *1,* 856-861.

(20) Alloy Phase Diagrams Center, http://www.asminternational.org/AsmEnterprise/APD/

(21) Naidu, S.V.N.; Rao, P.R. *Alloy Phase Diagrams* **1990**, *16*, 67.

(22) Darby Jr., J.B.; Downey, J.W.; Norton, L.J. *Trans. Metall. Soc. AIME* **1963**, *227*, 1028.

(23) Cai Y. ; Anderson A.B. *J. Phys. Chem. B,* **2004,** *108,* 9829

(24) Filhol J.S.; Neurock M. *Angew. Chem., Int. Ed.*, **2006,** *45,* 402.

(25) Skulason E. ; Karlberg G.S. ; Rossmeisl J. ; Bligaard T. ; Greeley J. ; Jonsson H. ; Norskov J.K. *Phys. Chem. Chem. Phys.*, **2007**, *9*, 3241-3250.

(26) Janik M.J. ; Taylor C.D. ; Neurock M. *J. Electrochem. Soc.*, **2009**, 156, B126

(27) Sarkar, A.; Vadivel Murugan, A.; Manthiram, A. *J. Mat. Chem.* **2009**, *19*, 159-165.

(28) Luo, H.L. *J. Less Common Met.* **1968**, *15*, 299-302.

(29) Goetz, W.K.; Brophy, J.H. . *J. Less Common Met.* **1964**, *6*, 345-353.

(30) Stamenkovic, V.R. ; Mun B.S. ; Mayhofer, K.J.J. ; Ross, P.N. ; Markovic, N.M. ; *J. Am. Chem. Soc*., **2006**, *128*, 8813.

(31) Hammer B. and Norskov J.K. *Surf. Sci.* **1995** *343* 211-220.

(32) Kitchin J.R. ; Norskov J.K.; Barteau M.A. ; Chen J.G. ; *J. Chem. Phys.*, **2004,** *120*, 10,240

(33) Stamenkovic, V.R., Mun, B.S. ; Arenz M. ; Mayrhofer, K.J.J. ; Lucas, C.A., Wang, G., Ross, P.N. ; Markovic, N.M. ; *Nat. Mat.* **2007,** *6*, 241.

(34) Anderson, A.B. ; Albu, T.V. ; *J. Electrochem. Soc*., **2000**, *147(11),* 4229.

(35) Norskov, J.K. ; Rossmeisl, J. ; Logadottir, A. ; Lindqvist, L. ; Kitchin, J.R. ; Bligaard, T. ; Jonsson, H. ; *J. Phys. Chem. B* **2004,** *108*, 17886.

(36) Melius, C.F.; Goddard, W.A. *Phys. Rev. A* **1974**, *10*, 1528-1540.

(37) Chen, W. ; Paul J.A.K. ; Barbieri, A. ; Van Hove, M.A. ; Cameron, S. ; Dwyers, D.J. ; *J. Phys. : Condens. Matter*, **1993,** *5*, 4585.

(38) Lesiak, B; Bilinski, A; Jozwik, A.; *Surf. Interface Anal.,* **2006,** *37,* 1143-1150.

(39) Ogasawara H. ; Naslund, L.A. ; MacNaughton, J.B. ; Anniyev, T. ; Nilsson A. ; *ECS Trans,* **2008**, *16,* 1385-1394.

(40) Deckers, S. ; Habraken, .H.P.M.F. ; Van der Weg, W.F. ; Denier van der Gon, A.W. ; Pluis, B. ; Van der Veen, J.F. ; Baudoing, R.; *Phys Rev .B.,* **1990,** *42*, 3253.

(41) Creemers, C. ; Deurinck, P. ; *Surface and Interface Analysis* **1997,** *25*, 177.

(42) Hoernstroem, S.E. ; Johansson, L.I. *App. Surf. Sci.* **1986,** *27* 235.

(43) Hoernstroem, S.E. ; Johansson, L.I.; Flodstroem, A. *App. Surf. Sci.* **1986,** *26*, 27.

(44) Gasteiger, H.A.; Ross Jr., P.N. ; Cairns, E.J. ; *Surface Science* **1993,** *293,*

67.

(45) Grgur, B.N. ; Markovic, N.M. ; Ross Jr., P.N. ; *J. Phys. Chem. B*, **1998,** *102*, 2494.

(46) Tsong, T.T. ; Ren, D.M. ; Ahmad, M. ; *Phys Rev B* **1988** *38*, 7428.

(47) Brown, D. ; Quinn, P.D. ; Woodruff, D.P. ; Noakes, T.C.Q. ; Bailey, P. ;

Surf. Sci. **2003,** *497*, 1

(48) Tsong, T.T.; Ng, Y.S.; McLane Jr., S.B.; *J. Chem. Phys.* **1980,** *73,* 1464.

(49) Wouda, P.T.; Schmid, M.; Nieuwenhuys, B.E.; Varga, P.; *Surf. Sci.* **1998,** *417,* 292

(50) Anton, R.; Eggers, H.; Veletas, J. *Thin Solid Films* **1993,** *226,* 39.

(51) Gauthier, Y.; Senhaji, A.; Legrand, B.; Treglia, G.; Becker, C.; Wandelt, K.; *Surf. Sci.* **2003,** *527,* 71-79.

(52) Derry, G.N.; Wan, R. *Surf. Sci.* **2004,** *566-568,* 862-868.

(53) Son, D.N.; Nakanishi, H.; David, M.Y.; Kasai, H.; *J. Phys. Soc. Jpn.,* **2009** *78-11,* 114601-1

(54) V. Stamenkovic, B. Fowler, B.S. Mun, G. Wang, P.N.Ross, C.A. Lucas, N.M. Markovic, *Science* **2007,** *315***,** 493-497.

Table 1. Segregation energy (eV) of various Y_3X metal alloys, where Y=Pd, Pt, or Rh and X is a transition metal. Large positive segregation energy implies that the top layer is pure noble metal, while the second layer is 50% noble metal. A star (*) next to the segregation energy indicates that a Y_3X phase has been observed experimentally. X is ordered by the segregation energy for Pd_3X.

Base \ Noble	Pd	Pt	Rh	Base \ Noble	Pd	Pt	Rh
Y	-2.679*	-2.451*	-2.326*	Cu	0.031	0.142	-0.307
Zr	-1.983*	-2.062*	-1.708*	Ni	0.311	0.462*	-0.217
Sc	-1.496*	-1.286	-1.356*	Nb	0.311*	-0.266*	-0.692*
Hg	-0.822	-0.778	-1.451	Ta	0.334*	-0.281*	-0.891*
Ti	-0.477*	-0.671*	-0.572*	Co	0.409	0.500*	0.007
Cd	-0.471	-0.468*	-1.133	Rh	0.474	0.391	0.000
Au	-0.392*	-0.328	-0.757	Tc	0.742	1.029	0.555
Ag	-0.223	-0.177	-0.513	V	0.668*	0.181*	0.054*
Fe	-0.133*	0.105*	-0.170	Ir	0.764	0.566	0.175
Mn	-0.105*	-0.122*	-0.358	Ru	0.884	0.830	0.555
Cr	-0.074*	-0.023	-0.189	Mo	1.232	1.002	0.178
Zn	-0.001	0.056*	-0.705	Os	1.275	1.327	0.909
Pt	-0.001	0.000	-0.501	W	1.996*	1.372	0.108*
Pd	0.000	0.005	-0.335	Re	2.089	1.686	0.853

Table 2. d-band center (eV) of various Y_3X metal alloys, where Y=Pd, Pt, or Rh and X is a transition metal. We see that Pd_3Ta and Pd_3W are most negative and closest to Pt.

Base \ Noble	Pd	Pt	Rh	Base \ Noble	Pd	Pt	Rh
Ta	-2.44	-2.85	-2.13	Co	-2.08	-2.75	-2.17
W	-2.39	-2.95	-2.27	Ir	-2.03	-2.65	-2.24
Ti	-2.37	-2.78	-2.10	Ni	-2.03	-2.70	-2.19
Nb	-2.37	-2.79	-2.10	Mn	-1.98	-2.65	-2.16
V	-2.31	-2.84	-2.26	Y	-1.97	-2.23	-1.59
Re	-2.28	-2.85	-2.31	Rh	-1.95	-2.59	-2.16
Zr	-2.25	-2.55	-1.86	Cu	-1.92	-2.58	-2.11
Mo	-2.25	-2.83	-2.26	Zn	-1.89	-2.58	-1.91
Os	-2.21	-2.76	-2.27	Pt	-1.83	-2.47	-2.09
Tc	-2.21	-2.79	-2.29	Pd	-1.82	-2.44	-2.04
Sc	-2.12	-2.52	-1.77	Cd	-1.66	-2.24	-1.70
Cr	-2.11	-2.73	-2.26	Au	-1.61	-2.18	-1.88
Ru	-2.11	-2.68	-2.23	Ag	-1.59	-2.17	-1.85
Fe	-2.10	-2.71	-2.10	Hg	-1.57	-2.13	-1.69

Figure Captions

Figure 1. Illustration of the structures used for predicting segregation of Y_3X alloys. We use a two dimensionally infinite four-layer (bottom layer fixed) slab of closest packed atoms with 4 independent atoms per layer. Here the 4 base metals, X, are shown in green, while the 12 noble metal atoms, Y, are gold. Shown is the segregation energy of a) Pd_3X , b) Pt_3X, and c) Rh_3X alloys, where positive implies segregation with the top layer pure Y, and the second layer 50% Y. A star (*) next to the base metal indicates a stable Y_3X phase has been observed experimentally.

Figure 2. Predicted segregation energies from theory for Pt_3X alloys, where positive shows that 100% Pt is preferred in the top layer and 50% in the second layer[3]. Experimental results:

Pt_3Co: 100% Pt in top layer and 48% 2nd layer (52% difference),

Pt_3Ni: 99% Pt in top layer and 30% 2nd layer (69% difference),

Pt_3Fe: 96% Pt top layer and 88% 2nd layer (8% difference).

Here we have plotted the difference between experimental top and 2nd layer Pt concentrations.

Figure 3.

Predicted 2nd-layer base metal enrichment energies of Pt_3Co, Pt_3Ni, Pt_3Fe, and Pt_3Ti. The diagram compares the energetics of 2nd-layer base metal enrichment between alloys. Pt_3Ni was found to be slightly favored over Pt_3Co for enrichment by 0.05 eV. Of the alloys, Pt3Ti was found to be least likely to be enriched by ~ 1.7 eV versus the other alloys. This figure explains why these alloys have been experimentally found to be nearly 100% Pt[5,30,33,37,40,41] on the surface layer, while their calculated segregation energy varied significantly. The difference in segregation energy is due to the difference in the 2^{nd}-layer enrichment energies.

Figure 4. Left: Reaction path for H_{ad} + OH_{ad} => H_2O_{ad} on the segregated Pd_3W (111) alloy surface (each point is the quantum mechanics (PBE) energy along the nudged elastic band (NEB) pathway for the vacuum case). Also shown are energies corrected for solvation by water.

Right: Summary of barriers for various reaction steps in the oxygen reduction reaction (ORR) for several catalysts. Numbers are based on quantum mechanics (PBE) in vacuum + solvation in H_2O. Barriers in boldface are important for the rate-determining step either in the O_2 dissociation or OOH association mechanism. Bottom: Picture of a (111) Pd_3W surface before and after the H_{ad} + OH_{ad} => H_2O_{ad} reaction.

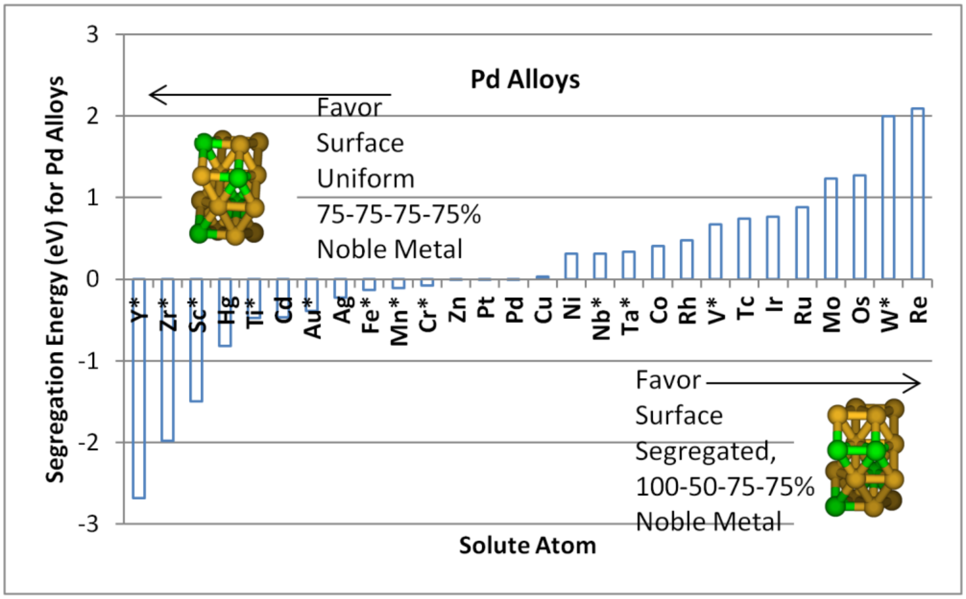
Pd Alloys
Segregation Energy (eV) for Pd Alloys
3
2
1
0
-1
-2
-3
Favor
Surface
Uniform
75-75-75-75%
Noble Metal
Y*
Zr*
Sc*
Hg
Ti*
Cd
Au*
Ag
Fe*
Mn*
Cr*
Zn
Pt
Pd
Cu
Ni
Nb*
Ta*
Co
Rh
V*
Tc
Ir
Ru
Mo
Os
W*
Re
Favor
Surface
Segregated,
100-50-75-75%
Noble Metal
Solute Atom

Figure 1a

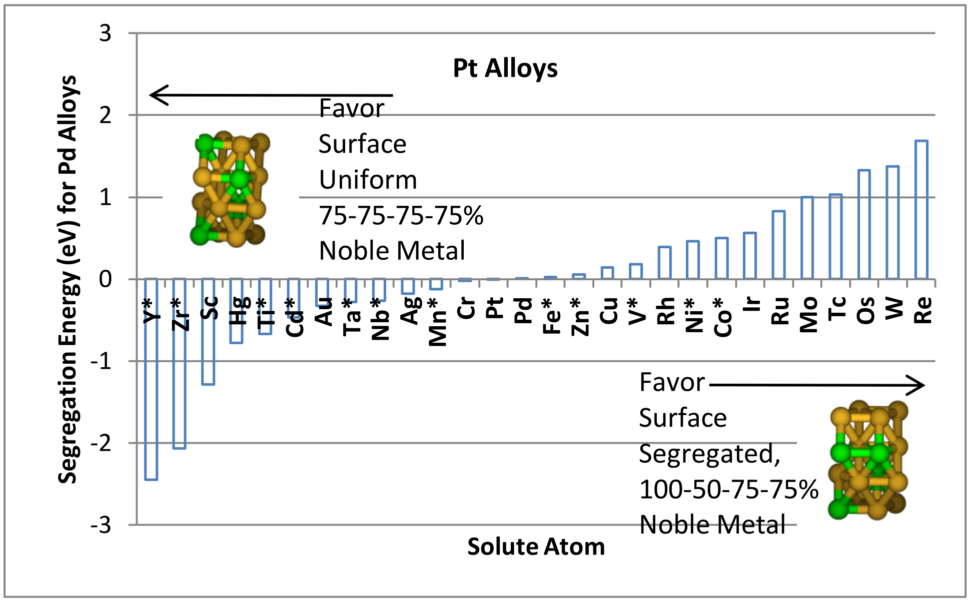
Pt Alloys
Segregation Energy (eV) for Pd Alloys
3
2
1
0
-1
-2
-3
Favor
Surface
Uniform
75-75-75-75%
Noble Metal
Y*
Zr*
Sc
Hg
Ti*
Cd*
Au
Ta*
Nb*
Ag
Mn*
Cr
Pt
Pd
Fe*
Zn*
Cu
V*
Rh
Ni*
Co*
Ir
Ru
Mo
Tc
Os
W
Re
Favor
Surface
Segregated,
100-50-75-75%
Noble Metal
Solute Atom

Figure 1b

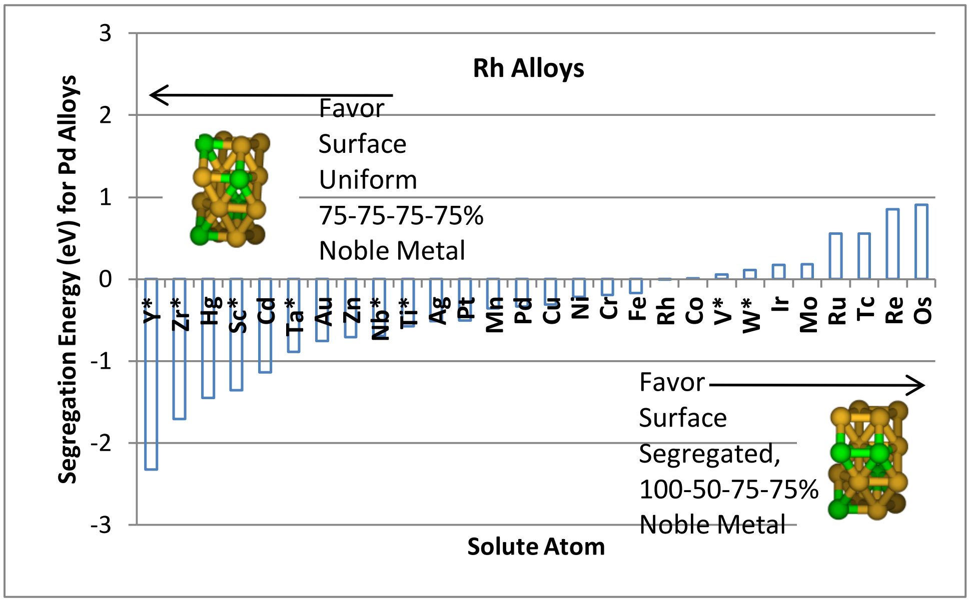
Rh Alloys
Segregation Energy (eV) for Pd Alloys
3
2
1
0
-1
-2
-3
Favor
Surface
Uniform
75-75-75-75%
Noble Metal
Y*
Zr*
Hg
Sc*
Cd
Ta*
Au
Zn
Nb*
Ti*
Ag
Pt
Mn
Pd
Cu
Ni
Cr
Fe
Rh
Co
V*
W*
Ir
Mo
Ru
Tc
Re
Os
Favor
Surface
Segregated,
100-50-75-75%
Noble Metal
Solute Atom

Figure 1c

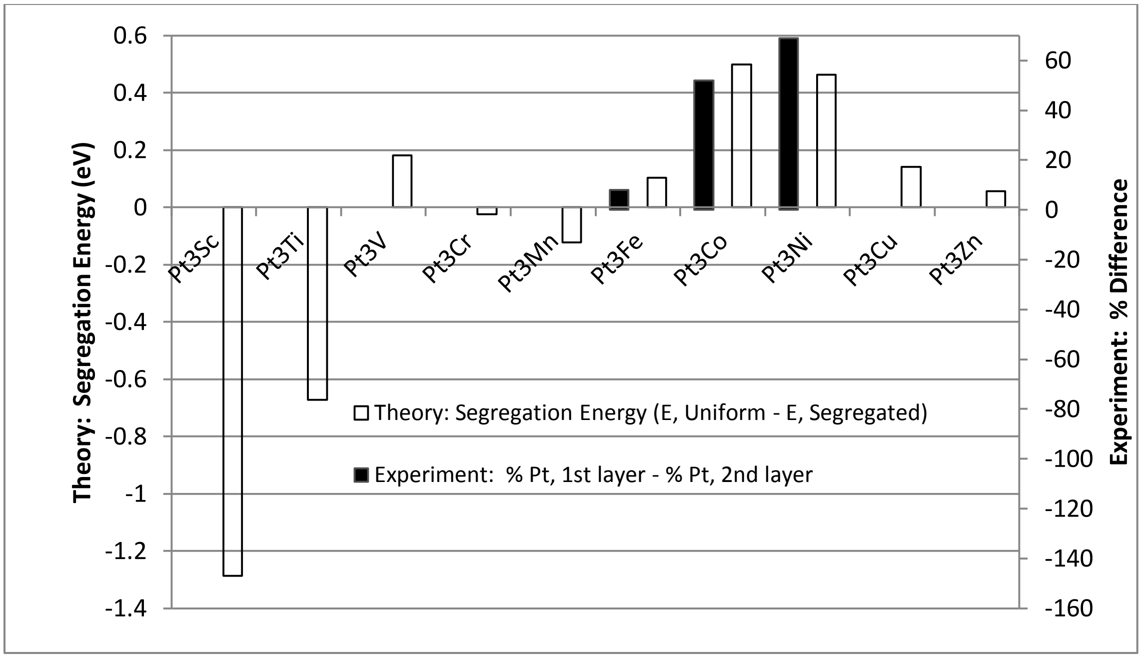
Theory: Segregation Energy (eV)
Experiment: % Difference
0.6
0.4
0.2
0
-0.2
-0.4
-0.6
-0.8
-1
-1.2
-1.4
60
40
20
0
-20
-40
-60
-80
-100
-120
-140
-160
Pt3Sc
Pt3Ti
Pt3V
Pt3Cr
Pt3Mn
Pt3Fe
Pt3Co
Pt3Ni
Pt3Cu
Pt3Zn
□ Theory: Segregation Energy (E, Uniform - E, Segregated)
■ Experiment: % Pt, 1st layer - % Pt, 2nd layer

Figure 2

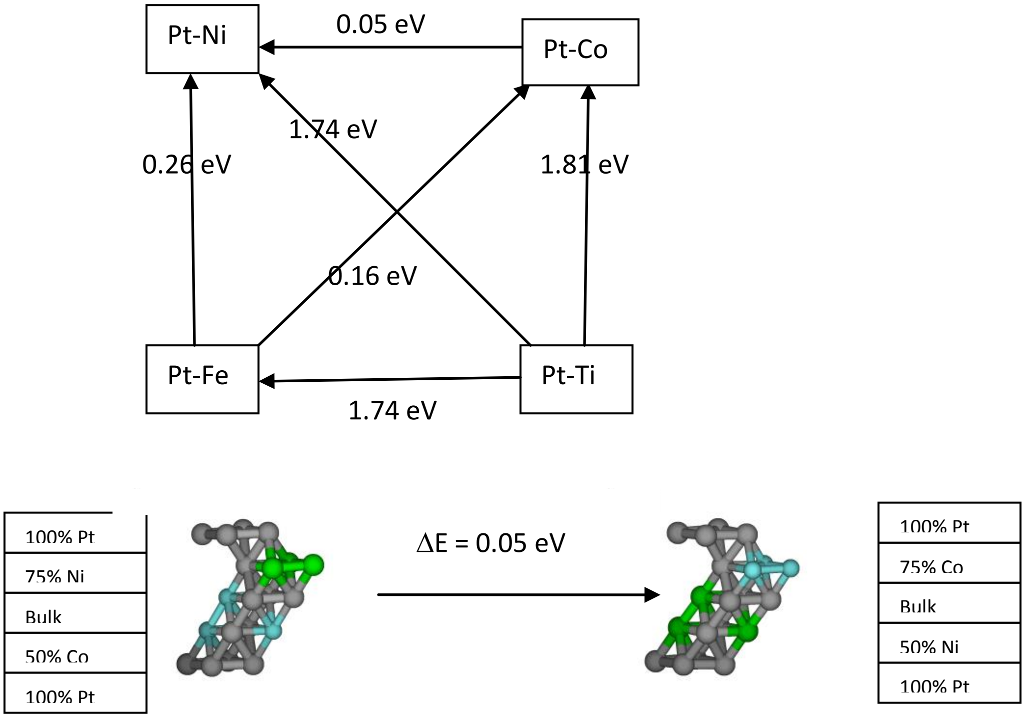
Pt-Ni
0.05 eV
Pt-Co
1.74 eV
0.26 eV
1.81 eV
0.16 eV
Pt-Fe
Pt-Ti
1.74 eV
100% Pt
75% Ni
Bulk
50% Co
100% Pt
ΔE = 0.05 eV
100% Pt
75% Co
Bulk
50% Ni
100% Pt

Figure 3

Barrier for $OH_{ad} + H_{ad} \Rightarrow H_2O_{ad}$ on Pd_3W

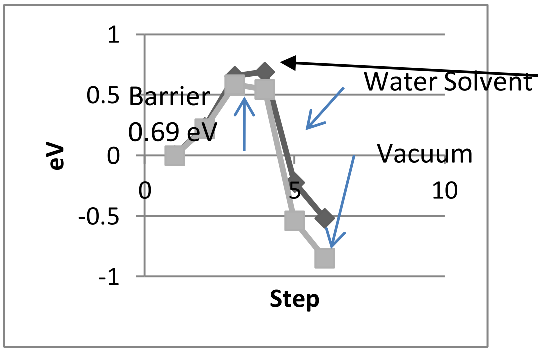

Barrier in water (eV)	Pd	Pd_3W	Pt	Pt_3Co
i) $O_{2ad} \Rightarrow 2O_{ad}$	**0.11**	**0.55**	0.35	1.11
ii) $O_{ad} + H_{ad} \Rightarrow OH_{ad}$	**0.70**	**0.54**	1.33	1.26
iii) $OH_{ad} + H_{ad} \Rightarrow H_2O_{ad}$	**0.90**	**0.69**	**0.51**	**0.38**
iv) $OO_{ad} + H_{ad} \Rightarrow OOH_{ad}$	0.63	0.52	**0.35**	**0.48**
v) $OOH_{ad} \Rightarrow O_{ad} + OH_{ad}$	0.32	0.75	**0**	**0**
Rate Det. Step for ORR	0.90	0.69	0.51	0.48

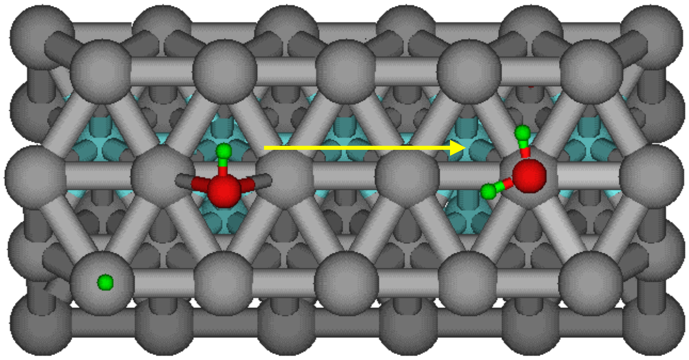

Figure 4

Base\Noble (Angstrom)	Pd	Pt	Rh
Ag	3.989	4.012	3.923
Au	3.998	4.022	3.929
Cd	4.022	4.047	3.955
Co	3.875	3.899	3.794
Cr	3.915	3.927	3.807
Cu	3.881	3.907	3.804
Fe	3.898	3.925	3.812
Hg	4.044	4.073	3.979
Ir	3.923	3.953	3.849
Mn	3.930	3.940	3.817
Mo	3.953	3.982	3.868
Nb	3.979	4.008	3.901
Ni	3.868	3.889	3.789
Os	3.909	3.944	3.841
Pd	3.944	3.968	3.868
Pt	3.953	3.979	3.876
Re	3.936	3.955	3.850
Rh	3.922	3.947	3.841
Ru	3.915	3.940	3.836
Sc	4.003	4.013	3.935
Ta	3.967	4.001	3.894
Tc	3.949	3.950	3.848
Ti	3.927	3.957	3.857
V	3.904	3.929	3.811
W	3.947	3.982	3.811
Y	4.124	4.133	3.867
Zn	3.916	3.939	3.836
Zr	4.024	4.055	3.966

Table S1: Lattice parameter of Y_3X cubic cell, where Y is the noble metal and X is the base metal

Alloy\Layers Segregation Energy (eV)	4 Layers	5 Layers	6 Layers
Pt_3Ti	-0.82	-0.91	-0.89
Pt_3Fe	0.10	0.12	0.11
Pt_3Co	0.50	0.40	0.39
Pt_3Ni	0.46	0.37	0.38

Table S2: Segregation energy of alloys of 4, 5 ,and 6 layer slabs

Surface Segregation of Pt Alloys with Adsorbed O and OH Predicted from Quantum Mechanics

Ted H. Yu,[†] Yao Sha,[†] Boris V. Merinov,*[,†] Pezhman Shirvanian,[‡] and William A. Goddard III*[,†]

Materials and Process Simulation Center

California Institute of Technology, MC 139-74, Pasadena, California 91125

Ford Motor Co., Research & Advanced Engineering

2101 Village Rd, Dearborn, Michigan 48104

Abstract

The segregation energy with adsorbed O and OH for 28 Pt_3X alloys where X is a transition metal was calculated with quantum mechanics. The calculations found that surface segregation became energetically unfavorable for Pt_3Co and Pt_3Ni in the presence of adsorbed O (-0.615 and -0.616 eV, respectively) and adsorbed OH (-0.046 and -0.150 eV, respectively). Pt_3Mo and Pt_3W, which were previously calculated to be strongly segregating without adsorbates, were calculated to be strongly non-segregating in the presence of adsorbed O (-1.91 and -2.26 eV, respectively) and adsorbed OH (-0.555 and -0.719 eV, respectively). Pt_3Ir and Pt_3Os were calculated to energetically favor surface segregation in the presence of both adsorbed O (+0.119 and +0.090 eV, respectively) and adsorbed OH (+0.268 and +0.510 eV, respectively). The results suggest that Pt_3Os and Pt_3Ir will stay surface segregated during fuel cell operations where OH and O are active adsorbed surface species. Pt_3Os is a better candidate than Pt_3Ir because the phase diagrams indicate that the two elements can be mixed.

Keywords: Segregation, Pt-based alloys, DFT, Co leaching, Ni leaching, Pt_3Co, Pt_3Ni, Pt_3Os

Introduction

Surface segregation for Pt alloys, where the surface layer is 100% Pt while the second layer has more than 50% of the alloy solute[1] (e.g., Co, Ni) is an important surface property that contributes to the improved catalytic properties[2] of Pt alloy catalysts in fuel cell cathodes. During the oxygen reduction reaction (ORR), adsorbates such as O and OH[3] on the catalyst surface can lead to undesirable leaching of the alloy solute onto the catalyst surface. Studies[4-6] have shown that the subsurface Co in Pt_3Co catalysts leaches onto the surface and into the solution during extended fuel cell operations. Over time, the subsurface layers become Co free, and this renders these layers pure Pt. The catalyst essentially becomes a Pt catalyst, and the electrolyte becomes filled with undesirable Co products. Ni leaching has been observed in Pt_3Ni as well[7].

In previous works[8, 9], surface segregation energy has been studied by QM by comparing the energy of the "surface uniform" slab, where the slab layers are all 75% Pt, and the desirable "surface segregated" slab, where the top layer is pure Pt, and the second layer is enriched in solute metals. Pt_3Co and Pt_3Ni were predicted to be surface segregating, while Pt_3Fe was predicted to be only slightly surface segregating, as seen in experiments[1]. However, these studies do not take into account what happens when the surfaces are exposed to ORR adsorbates, which is the case when fuel cells are operating. Previous work predicted when one of those adsorbates, O, is on the Pt surface, Pt_3Co and Pt_3Ni are no longer energetically favor surface segregation[10]. Both O and OH species have been known to accumulate on the Pt surface sites as intermediates of the ORR[11, 12].

Therefore, it is important to find Pt alloy catalysts where the solute metal is energetically favored to remain subsurface when the surface is exposed to adsorbed ORR species. We use quantum mechanics (QM) to examine 28 Pt binary alloys to identify good segregating alloys that maintain the favorable segregating property when the oxidative species, O and OH, are adsorbed on the surface. To calculate the segregation energy, we use the lowest energy O and OH surface binding sites from Pt_3Co and Pt_3Ni studies (see supplemental information S1).

Results and Discussion

Figure 1 and Table 1 display the segregation energy with adsorbed O and OH with adsorption sites shown in Figure 2. For O adsorbed surface segregation, the best five solute metals were Ir, Os, Au, Rh, and R. For OH adsorbed surface segregation, the best five solute metals were Os, Re, Ir, Ru, and Tc. All of these solute metals are considered difficult to oxidize and have positive electric potentials versus hydrogen electrode. All but one (Tc) are considered noble metals. As a general rule, segregation becomes unfavorable when the O and OH are adsorbed on a metal that is easily oxidized. In Table 2, the change in segregation energy when oxygen is adsorbed on a surface is tabulated with the heat of formation of the corresponding metal oxide.

The segregation energy can vary significantly when O or OH are adsorbed on the surface. For example, without adsorbed species, the best five segregation energies were Pt alloyed with Re, W, Os, Tc, and Mo[9]. Notably, the segregation energy of Pt_3W and Pt_3Mo changes from strongly favorable to strongly unfavorable with adsorbed O and OH, as both W and Mo are known to easily react to form oxides (Table 2).

In the presence of adsorbed O and OH, only two alloys were found to have favorable segregation energy, Pt_3Ir[13] and Pt_3Os. Looking at the Pt-Os diagram[14], up to 20% Os can be mixed into the Pt structure. On the other hand, Ir cannot be mixed into the Pt structure[15]. Therefore, PtOs is the more promising of the two alloys that merit further study and is predicted to be more resistant to solute metal leaching than Pt_3Co or Pt_3Ni.

In summary, we found only a few Pt binary alloys favor surface segregation in the presence of adsorbed O or OH. Out of these, only Pt_3Os and Pt_3Ir show surface segregation in the presence of both species. However, further study is needed to see if Pt_3Os or Pt_3Ir will have good ORR performance.

Table 1: Segregation Energy of adsorbed O, adsorbed OH, no adsorbates (from previous work[9]). * indicates the Pt_3X alloy has a reported 3:1 phase. Positive indicates favoring of surface segregation. Only Pt_3Ir and Pt_3Os favor surface segregation in all three cases.

	O	OH	No adsorbate
Pt_3Ir	0.12	0.27	0.57
Pt_3Os	0.09	0.51	1.33
Pt_3Au	-0.01	-0.11	-0.33
Pt_3Rh	-0.14	0.05	0.39
Pt_3Ru	-0.15	0.25	0.83
Pt_3Pd	-0.17	-0.05	0.01
Pt_3Ag	-0.26	-0.18	-0.18
Pt_3Cu	-0.54	-0.07	0.14
Pt_3Co*	-0.62	-0.05	0.50
Pt_3Ni*	-0.62	-0.15	0.46
Pt_3Hg	-0.67	-0.60	-0.78
Pt_3Tc	-0.69	0.12	1.03
Pt_3Re	-0.87	0.44	1.69
Pt_3Cd*	-0.91	-0.64	-0.47
Pt_3Zn*	-0.95	-0.27	0.06
Pt_3Fe*	-0.97	-0.44	0.02
Pt_3Mn*	-1.61	-0.92	-0.12
Pt_3Cr	-1.92	-1.20	-0.02
Pt_3Mo	-1.92	-0.56	1.00
Pt_3W	-2.26	-0.72	1.37
Pt_3V*	-2.45	-1.15	0.18
Pt_3Sc	-3.32	-2.75	-1.29
Pt_3Ti*	-3.61	-2.69	-0.67
Pt_3Nb*	-3.67	-2.39	-0.27
Pt_3Y*	-3.93	-3.62	-2.45
Pt_3Ta*	-4.29	-2.89	-0.28
Pt_3Zr*	-4.31	-3.89	-2.06

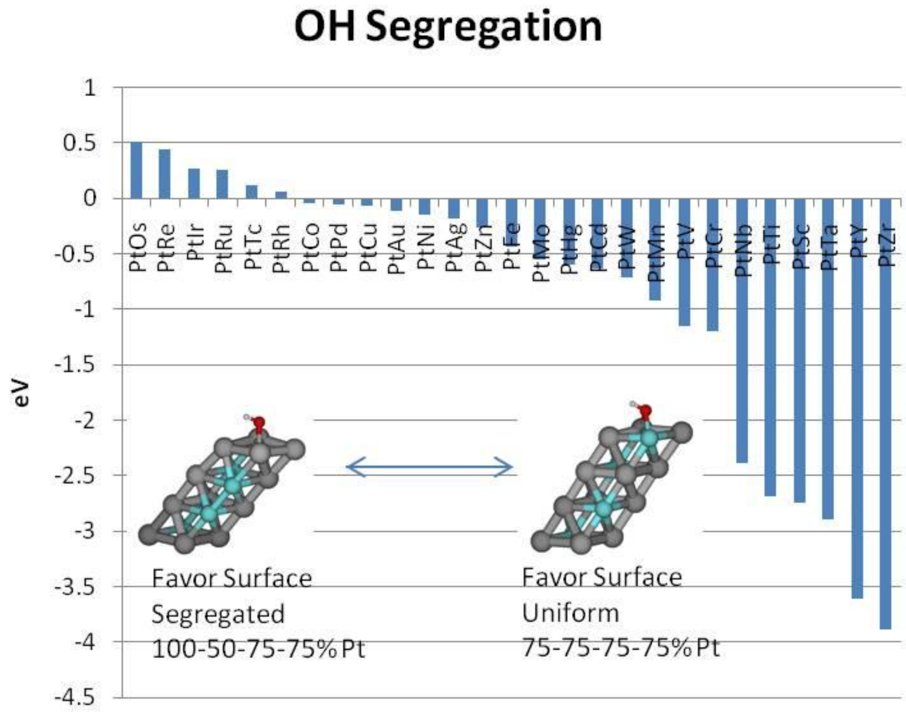

Figure 1a: Segregation energy with adsorbed OH.

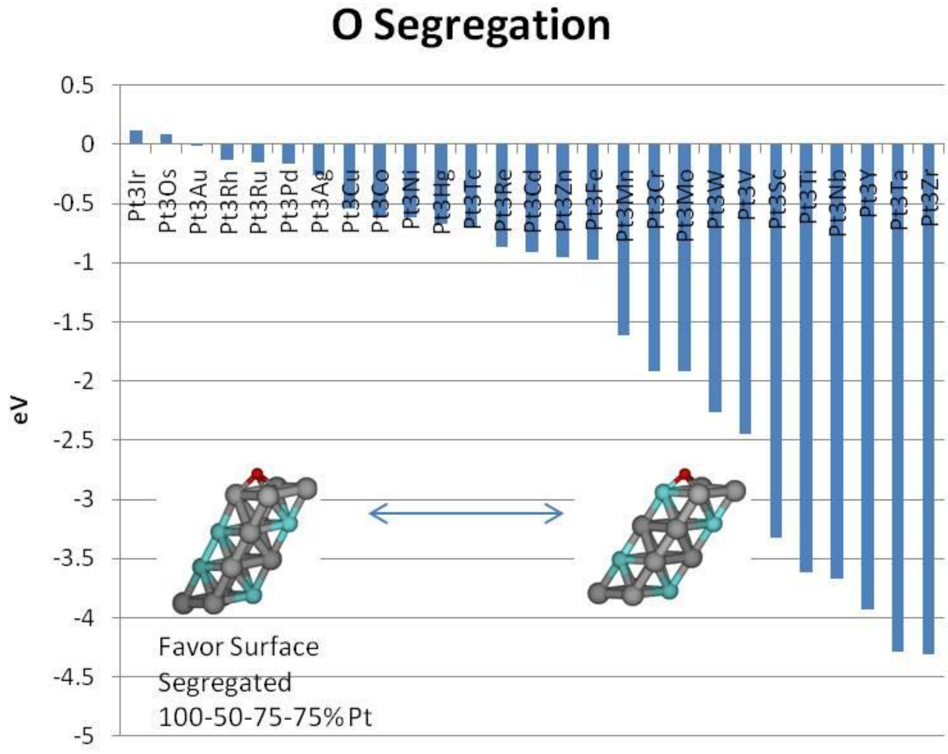

Figure 1b: Segregation energy with adsorbed O.

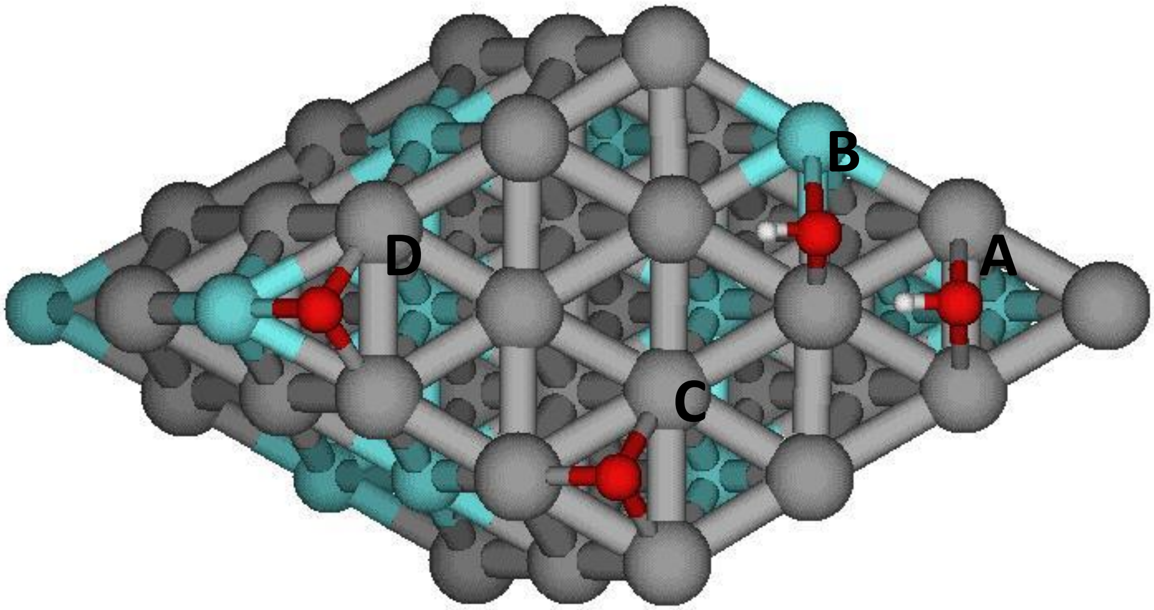

Figure 2: OH and O adsorption sites: A) OH on surface segregated slab, B) OH on surface uniform slab, C) O on surface segregated slab, D) O on surface uniform slab. These surface sites were determined as the lowest energy sites from Pt_3Ni studies, as shown in supplemental information S1.

REFERENCES

1. Gauthier, Y., PT-metal alloy surfaces: Systematic trends. *Surf Rev Lett* **1996,** *3* (5-6), 1663-1689.

2. Markovic, N. M.; Ross, P. N., Surface science studies of model fuel cell electrocatalysts. *Surf Sci Rep* **2002,** *45* (4-6), 121-229.

3. Ogasawara, H.; Naslund, L. A.; Macnaughton, J. B.; Anniyev, T.; A., N., *ECS Transactions* **2008,** *16*, 1385-1394.

4. Maillard, F.; Dubau, L.; Durst, J.; Chatenet, M.; Andre, J.; Rossinot, E., *Electrochem Commun* **2010,** *12*, 1161-1164.

5. Dubau, L.; Maillard, F.; Chatenet, M.; Guetaz, L.; Andre, J.; Rossinot, E., *J Electrochem Soc* **2010,** *157* (12), B1887-B1895.

6. Colon-Mercado, H. R.; Popov, B. N., Stability of platinum based alloy cathode catalysts in PEM fuel cells. *J Power Sources* **2006,** *155* (2), 253-263.

7. Colon-Mercado, H. R.; Kim, H.; Popov, B. N., Durability study Of Pt3Ni1 catalysts as cathode in PEM fuel cells. *Electrochem Commun* **2004,** *6* (8), 795-799.

8. Jacob, T.; Goddard, W. A., Water formation on Pt and Pt-based alloys: A theoretical description of a catalytic reaction. *Chemphyschem* **2006,** *7* (5), 992-1005.

9. Yu, T. H.; Sha, Y.; Merinov, B. V.; Goddard, W. A., Improved Non-Pt Alloys for the Oxygen Reduction Reaction at Fuel Cell Cathodes Predicted from Quantum Mechanics. *J Phys Chem C* **2010,** *114* (26), 11527-11533.

10. Ma, Y.; Balbuena, P. B., *Surf Sci Rep* **2009,** *603*, 349-353.

11. Sepa, D. B.; Jojnovic, M. V.; Vracar, L. M.; Damjanovic, A., *Electrochim Acta* **1981,** *26*, 781.

12. Sepa, D. B.; Jojnovic, M. V.; Vracar, L. M.; Damjanovic, A., *Electrochim Acta* **1987,** *32*.

13. Ramirez-Caballero, G. E.; Ma, Y. G.; Callejas-Tovar, R.; Balbuena, P. B., *Phys Chem Chem Phys* **2010,** *12* (9), 2209-2218.

14. Voronova, L. I.; Polyakova, V. P.; Savitskii, E. M., Alloys of the System Pt-Os. *Russian Metallurgy* **1984,** (5), 201-203.

15. Raub, E.; Plate, W., Aushartung Und Entmischung Der Platin-Iridium-Legierungen. *Zeitschrift Fur Metallkunde* **1956,** *47* (10), 688-693.

Theoretical Study of Zr Containing Ternary Alloy PEMFC Catalysts with Improved Durability

*Ted H. Yu, Boris V. Merinov, Ho Cheng Tsai, and William A. Goddard III**

Materials and Process Simulation Center, California Institute of Technology
MC 139-74, Pasadena, California 91125

1200 E California Blvd MC 139-74, Pasadena, CA 91125 M/S 139-74
Phone: +1 626 395 2731 FAX +1 626 585 0918
* Email: wag@wag.caltech.edu

ABSTRACT

We have computationally studied ternary alloys containing Zr, which show experimentally better stability compared to binary alloys Pt_3Co and Pt_3Ni, and found that the improved durability of the ternary alloys containing Zr had a tradeoff. The addition of Zr makes the alloy surface segregation worse. In our analysis, Pt-Co/Zr and Pt-Ni/Zr still favors surface segregation, but the extent of surface segregation is not as high as Pt-Co and Pt-Ni. Given that both surface segregation and durability are important, we scanned potential ternary alloys containing Pt or Pd, Zr, and M (transition metals from column 4-9), and found the combinations with the best durability and surface segregation to be alloys where M = Rh, Ir, Ru, Os, and Re.

KEYWORDS: Ternary alloys, DFT, Segregation, Durability, PEMFC ORR

In recent years, impressive progress has been made in the development of metal alloy cathode catalysts for a proton exchange membrane fuel cell (PEMFC). Alloys such as Pt_3Co and Pt_3Ni, demonstrate improved oxygen reduction reaction (ORR) activity compared to pure Pt [1, 2]. These materials show a unique surface segregation where the first layer is 100% Pt, while the 2nd layer is enriched to ~ 50% Co or Ni [3]. The subsurface Co or Ni enhances the catalytic activity and is covered by the noble Pt surface, preventing oxidation reactions of Co or Ni. According to [4, 5] the catalytic enhancement occurs because the subsurface non-Pt metals change the occupied density of state (DOS) of the surface Pt and modifies the binding energy of ORR species on the catalytic surface. The changes in the binding energy lower the barrier of the rate-determining step (RDS) for Pt_3Co and Pt_3Ni [6, 7]. That is why the metal distribution at the surface segregation is of great importance for the alloy catalysts.

An important issue that restrains commercialization of the binary Pt-alloys as PEMFC catalysts is the poor stability of these alloys under real fuel cell operating conditions. It was found that Co and Ni leach out of Pt_3Co and Pt_3Ni catalysts into the electrolyte [8-11]. As an alternative, Pt-alloys with early transition metals, such as Pt_3Y and Pt_3Sc, were proposed to improve the ORR efficiency and alloy catalyst durability [12]. These alloys have very favorable heat of formation (Pt_3Sc = -1.06 eV/atom, Pt_3Y = -0.99 eV/atom) compared to Pt_3Co (-0.06 eV/atom) or Pt_3Ni (-0.05 eV/atom). This affects the kinetic stability of the alloy, making it difficult for the solute metal (Sc, Y) in the bulk to migrate to the surface. However, the good bulk stability and durability properties of Pt_3Y and Pt_3Sc are compromised by the very poor surface segregation [7] that leads to the presence of Sc/Y on the surface, and formation of the corresponding oxides which reduce the Pt surface area, as found in experiments [13]. Poor surface segregation also means that the second layer of the catalyst will not be enriched from 25% to 50% in Sc/Y, as it is in the case of Co/Ni in Pt_3Co and Pt_3Ni [3].

Therefore, it is desirable to find alloy catalysts with both bulk stability and surface segregation. Unfortunately, the known Pt binary alloys have either good bulk stability or good surface segregation, but not both of these properties together.

Recently, ternary alloys(Pt-Co-Zr, Pt-Ni-Zr) containing valve metals (early column transition metals) have been studied experimentally and proposed as promising PEMFC catalysts for the ORR [14, 15]. These ternary alloys exhibit improved ORR activity as well as good durability. To better understand how adding a third valve metal influences energetics, segregation, and stability of the corresponding alloys, we performed a density functional theory (DFT) study of a number of ternary alloys with various valve metals.

The SeqQuest code [16] that employs Gaussian basis functions, rather than the plane wave basis often applied in periodic systems, was used for our periodic slab calculations. The Perdew, Burke, and Ernzerhof (PBE) [17] flavor of DFT was employed in this investigation. The core electrons were replaced with nonlocal core potentials or pseudopotentials [18]. A grid density of 5 points per angstrom was applied.

We used three-dimensional face-centered tetragonal unit cells containing 4 atoms (two Pt atoms, one “segregating” metal, and one valve metal) with a reciprocal space grid of 8 × 8 × 8 to determine the bulk heat of formation. A ternary alloy (111) surface was represented by a 2 × 2 hexagonal unit cell with 4 metal atoms in each of the 4 layers. This model was employed for calculations of segregation energy. The top two layers are allowed to relax, whereas the bottom layers are fixed with the atoms in the bulk positions of the Pt_3M binary alloy (where M is the segregating metal) with a reciprocal space grid of 5 × 5 × 0. The experimental study of the Pt-Ni-Zr alloys [14] indicates that the lattice parameters are uncorrelated to the Zr content and depend only on the Pt-Ni content. Due to the use of Gaussian basis functions, addition of an artificial vacuum surface is not necessary. All calculations were performed with optimized spin.

The heat of formation of ternary alloys of Pt, Co, or Ni, and X, where X is a valve metal, was calculated and compared with that of binary alloys, Pt_3Co, Pt_3Ni, Pt_3Sc, and Pt_3Y (Figure 1). We find that the ternary alloys with valve metals have heats of formation much better than Pt_3Co (-0.06 eV) and Pt_3Ni (-0.05 eV) and comparable to Pt_3Y (-0.99 eV) and Pt_3Sc (-1.06 eV). Thus, we would expect the durability of these ternary alloys to be much improved over Pt_3Co and Pt_3Ni, with the valve metals acting like a “glue” that reduces the migration of Co/Ni in the alloy. The addition of a valve metal X (Sc, Y, Ti, Zr, Hf, V, Nb, Ta) to Pt-Co greatly improves the heat of formation, because the valve metals have less-than-half-filled d-orbitals, making their electronegativity very low. The valve metals prefer to bond to a more electronegative Pt, Ni, or Co, than to themselves, making the mixture of Pt-Co-X very strong. The improvement in the heat of formation tends to be greatest for valve metals of the first two columns, and is much lower when the valve metal is of the third column (V, Nb, Ta). This strong preference of the valve metals for bonding to Pt also has a negative effect in terms of catalyst surface segregation.

The second-layer enrichment of Co or Ni [3] in Pt alloys is an important property that is not observed experimentally in other Pt alloys containing, for instance, Ti [19], Fe [3], or Cu [20]. Theoretical results of QM studies of surface segregation agree with experiments and show the segregation energy in Pt_3Co and Pt_3Ni to be more favorable than that of Pt_3Ti, Pt_3Fe, Pt_3Cu, Pt_3Sc, Pt_3Y, or Pt_3Zr[7]. This is due to the large energetic penalty associated with M - M bonds in the 2nd layer [7] in these Pt_3M cases, which means that the 2nd-layer enrichment of the segregating metals over 25% will not be observed in such binary alloys as Pt_3Sc, Pt_3Y, Pt_3Ti, and Pt_3Zr.

To study surface segregation in ternary alloys containing valve metals, we calculated the segregation energy of Pt_3M/Zr and Pd_3M/Zr, where M is a transition metal from the 4th to 9th column, using a method similar to previous ternary alloy calculations for Pt_3Ni/M [21] and Pt_2IrM

[22]. In our analysis, the two "surface segregated" slabs, shown in Figure 2, contain 100% Pt or Pd on the surface and 50% Pt or Pd on the 2nd layer, whereas the two fixed bottom layers contain 75% Pt or Pd. The two surface uniform slabs contain 75% Pt or Pd in all layers.

The relative energies of the four cases are shown in Table 1, with the segregation energy of the ternary alloy Pt-M-Zr defined as the energy of the lowest uniform case minus the energy of the lowest segregated case with positive quantities indicating good surface segregation. The segregation energies calculated previously [7] for binary alloy Pt_3M are tabulated for reference.

The addition of a segregating metal M from transition metal columns 4 to 9 increases the segregation energy versus Pt_3Zr (-2.063 eV) and Pd_3Zr (-1.983 eV) significantly (Table 1). The best segregation energies were found for the ternary alloys with M = Re (Pt_3Re/Zr = 0.671, Pd_3Re/Zr = 0.972). The reason for this is because the addition of M allows the 2nd layer to contain 25% Zr and 25% M, and there will not be a Zr - Zr bond energy penalty in the 2nd layer.

For Pt_3Co/Zr and Pt_3Ni/Zr, the segregation energy is positive (0.092 and 0.127 eV, respectively) indicating slight surface segregation. For comparison, the segregation energy of the above-mentioned ternary alloy is lower than the segregation energy of the corresponding binary alloys Pt_3Co (0.500 eV) and Pt_3Ni (0.462 eV). This makes sense, because the reported improved catalytic activity of Pt-Ni/Zr and Pt-Co/Zr over pure Pt is less than that of Pt_3Co and Pt_3Ni [14, 15]. As seen in Figure 1, the addition of Zr greatly improves the heat of formation of Pt-Ni and Pt-Co alloys, which agrees with experimental improved durability results [14, 15]. In most cases, the ternary alloy with Zr has lower segregation energy than its corresponding binary alloy without Zr.

Figure 3 shows potential ternary alloys with Zr which are categorized by their theoretical heat of formation and segregation energy. There are several ternary alloys with a better heat of formation and segregation energy than Pt-Co/Zr and Pt-Ni/Zr. For the Pd-based ternary alloys, the five most favorable cases with both high segregation energy and low heat of formation are Pd-Rh/Zr, Pd-Ir/Zr, Pd-Ru/Zr, Pd-Os/Zr, and Pd-Re/Zr. For the Pt-based ternary alloys, the five most favorable cases are Pt-Rh/Zr, Pt-Ir/Zr, Pt-Ru/Zr, Pt-Os/Zr, and Pt-Re/Zr. Among these cases, the alloys with Re have the best segregation energy and worst heat of formation. The alloys with Rh have the best heat of formation and worst segregation energy. The alloys with Ir, Ru, and Os are intermediate with values for heat of formation and segregation between those for the alloys with Rh and Re.

The addition of Zr to Pd or Pt alloys with M = Rh, Ir, Ru, Os, and Re make ternary alloys with negative heat of formation. This means that the ternary alloy will exist as a homogeneous phase rather than separate phases. Unlike Pt_3Co and Pt_3Ni, binary alloys Pt_3M and Pd_3M with M = Rh, Ir, Ru, Os, and Re, do not exhibit a phase at room temperature, (with the exception of Pt_3Re) because they have positive heat of formation. As such, it can be difficult to make homogeneous binary alloys with the above-mentioned M metals. The addition of Zr makes the mixing of the ternary alloy energetically favorable. The heat of formation of the best Pt-Rh/Zr alloy was found to be -0.96 eV/atom, which is comparable to that of Pt_3Sc and Pt_3Y.

In summary, we studied ternary alloys containing valve metals such as Zr, which were experimentally found to have better durability than Pt_3Co or Pt_3Ni. The improved durability is due to the better bulk heat of formation of the ternary alloys with valve metals, and the alloys with Hf have theoretically the best heat of formation. The poor surface segregation of Pt_3Zr is improved with the addition of a segregating metal, such as Co or Ni. In general, the surface segregation of ternary alloys containing Zr is worse than that of binary alloys without Zr, which partially explains why their improvement in experimental ORR activity is not as high as Pt_3Co or Pt_3Ni. Finally, we scanned potential ternary alloys containing Zr and found that the best cases are ternary alloys containing Rh, Ir, Ru, Os, or Re. Thus, the obtained results may have a significant interest for experimentalists and can be used for synthesis of new stable ternary alloys with improved ORR catalytic activity.

This work was supported by the U.S. National Science Foundation under Grant DE-AC02-06CH11357. The facilities of the Materials and Process Simulation Center (MSC) used in this study were established with grants from DURIP-ONR, DURIP-ARO, and NSF-MRI. Additional support for the fuel cell research was provided by the Ford Motor Company.

[1] N. M. Markovic, and P. N. Ross, Surf Sci Rep **45**, 121 (2002).
[2] V. R. Stamenkovic *et al.*, Science **315**, 493 (2007).
[3] Y. Gauthier, Surf Rev Lett **3**, 1663 (1996).
[4] A. Ruban *et al.*, J Mol Catal a-Chem **115**, 421 (1997).
[5] B. Hammer, and J. K. Norskov, Surf Sci **343**, 211 (1995).
[6] Y. Sha *et al.*, Journal of Physical Chemistry Letters **2**, 572 (2011).
[7] T. H. Yu *et al.*, J Phys Chem C **114**, 11527 (2010).
[8] H. R. Colon-Mercado, and B. N. Popov, J Power Sources **155**, 253 (2006).
[9] L. Dubau *et al.*, J Electrochem Soc **157**, B1887 (2010).
[10] F. Maillard *et al.*, Electrochem Commun **12**, 1161 (2010).
[11] H. R. Colon-Mercado, H. Kim, and B. N. Popov, Electrochem Commun **6**, 795 (2004).
[12] J. Greeley *et al.*, Nature Chemistry **1**, 552 (2009).
[13] M. K. Jeon, and P. J. McGinn, J Power Sources **196**, 1127 (2011).
[14] J. F. Whitacre, T. I. Valdez, and S. R. Narayanan, Electrochim Acta **53**, 3680 (2008).
[15] C. C. Hays *et al.*, ECS Transactions **25**, 619 (2009).
[16] P. Schultz, SEQQUEST, Sandia National Laboratory).
[17] J. P. Perdew, K. Burke, and M. Ernzerhof, Phys Rev Lett **77**, 3865 (1996).
[18] C. F. Melius, B. D. Olafson, and W. A. Goddard, Chem Phys Lett **28**, 457 (1974).
[19] W. H. Chen *et al.*, J Phys-Condens Mat **5**, 4585 (1993).
[20] Y. Gauthier *et al.*, Surf Sci **527**, 71 (2003).
[21] Y. H. Zhang *et al.*, Surf Sci **605**, 1577 (2011).
[22] Y. G. Ma, and P. B. Balbuena, J Electrochem Soc **157**, B959 (2010).

Table 1. Four-layer surface slabs (Figure 2) containing Pt$_3$M/Zr and Pd$_3$M/Zr were calculated with DFT. For the surface uniform cases, the slabs contain 75% Pd or Pt in all four layers, with the position of M and Zr varying in the surface and 2nd layer. For the surface segregated cases, the slabs contain 100% Pd or Pt in the surface layer, 50% Pd or Pt in the 2nd layer, and 75% Pd or Pt in the 3rd and 4th layer, with the position of M and Zr varying. The segregation energy of the ternary alloys was determined to be the difference between the best surface uniform case and the best surface segregated case, with a positive number indicating good surface segregation. The surface segregation of binary alloy Pd$_3$M and Pt$_3$M are tabulated for reference [7].

Pd$_3$M/Zr **Pt$_3$M/Zr**	**Surface Segregated A**	**Surface Segregated B**	**Surface Uniform A**	**Surface 25% Zr**	**Segregation Energy Ternary**	**Segregation Energy Binary [7]**
Pd$_3$Cr/Zr	0.702	0.919	0.000	0.743	-0.702	-0.074
Pd$_3$Mn/Zr	0.598	0.935	0.000	0.756	-0.598	-0.105
Pd$_3$Fe/Zr	0.254	0.555	0.000	0.322	-0.254	-0.133
Pd$_3$Co/Zr	0.074	0.099	0.000	0.904	-0.074	0.409
Pd$_3$Ni/Zr	0.167	0.686	0.000	1.043	-0.167	0.311
Pd$_3$Cu/Zr	0.111	0.201	0.000	0.986	-0.111	0.031
Pd$_3$Mo/Zr	0.000	0.488	0.141	0.350	0.141	1.232
Pd$_3$Tc/Zr	0.000	0.755	0.480	1.020	0.480	0.742
Pd$_3$Ru/Zr	0.000	0.472	0.641	1.213	0.641	0.884
Pd$_3$Rh/Zr	0.000	0.060	0.339	1.150	0.339	0.474
Pd$_3$Ag/Zr	0.578	0.751	0.000	1.272	-0.578	-0.223
Pd$_3$W/Zr	0.000	0.627	0.462	0.406	0.406	1.996
Pd$_3$Re/Zr	0.000	0.957	0.972	1.407	0.972	2.089
Pd$_3$Os/Zr	0.000	0.760	0.927	1.590	0.927	1.275
Pd$_3$Ir/Zr	0.000	0.152	0.505	1.370	0.505	0.764
Pd$_3$Pt/Zr	0.073	0.000	0.124	1.247	0.124	-0.001
Pd$_3$Au/Zr	0.445	0.489	0.000	1.311	-0.445	-0.392
Pt$_3$Cr/Zr	0.635	0.796	0.000	0.385	-0.635	-0.023
Pt$_3$Mn/Zr	0.515	0.861	0.000	0.554	-0.515	-0.122
Pt$_3$Fe/Zr	0.161	0.378	0.000	0.170	-0.161	0.105
Pt$_3$Co/Zr	0.000	0.152	0.092	0.757	0.092	0.500
Pt$_3$Ni/Zr	0.000	0.270	0.127	0.921	0.127	0.462
Pt$_3$Cu/Zr	0.029	0.188	0.000	0.863	-0.029	0.142
Pt$_3$Mo/Zr	0.053	0.565	0.165	0.000	-0.053	1.002
Pt$_3$Tc/Zr	0.000	0.635	0.406	0.756	0.406	1.029
Pt$_3$Ru/Zr	0.000	0.348	0.376	0.936	0.376	0.830
Pt$_3$Rh/Zr	0.020	0.000	0.240	0.943	0.240	0.391
Pt$_3$Pd/Zr	0.000	0.070	0.021	1.024	0.021	0.005

Pt_3Ag/Zr	0.607	0.911	0.000	1.491	-0.607	-0.177
Pt_3W/Zr	0.122	0.644	0.201	0.000	-0.122	1.372
Pt_3Re/Zr	0.000	0.796	0.671	0.782	0.671	1.686
Pt_3Os/Zr	0.000	0.513	0.633	1.154	0.633	1.327
Pt_3Ir/Zr	0.031	0.000	0.269	1.037	0.269	0.566
Pt_3Au/Zr	0.513	0.722	0.000	1.567	-0.513	-0.328

Figure 1. The heat of formation of Pt_2Co/X and Pt_2Ni/X alloys (where X is a valve metal) compared to Pt_3M alloys.

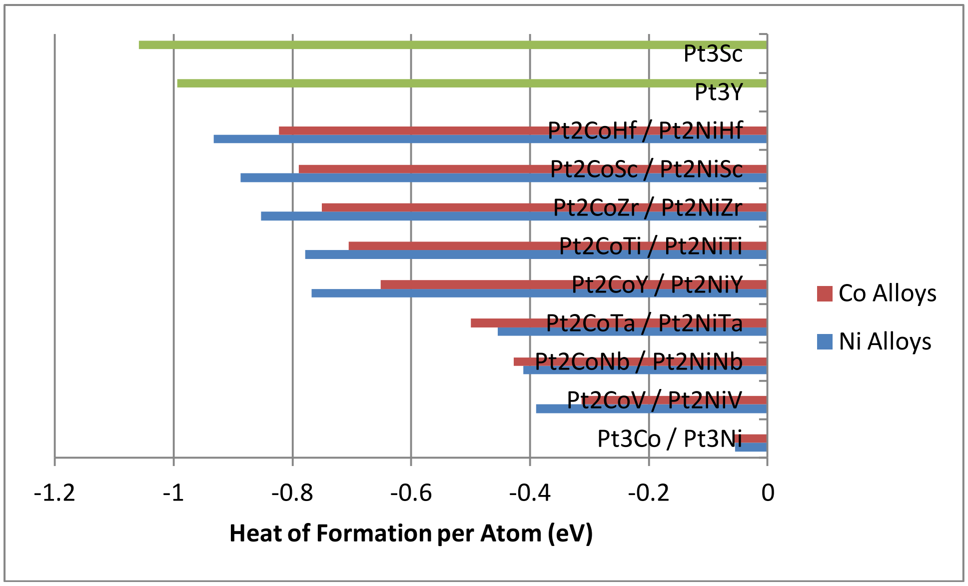

Figure 2. The slabs of Zr-containing ternary alloys of Pt-M/Zr or Pd-M/Zr, where M is a segregating metal. The two surface segregated cases differ in the bond between layer 2 and 3. In case A, the bond is M - M, while in case B, the bond is M - Zr. For the two surface uniform cases, case A has 25% M on the surface, while case B has 25% Zr.

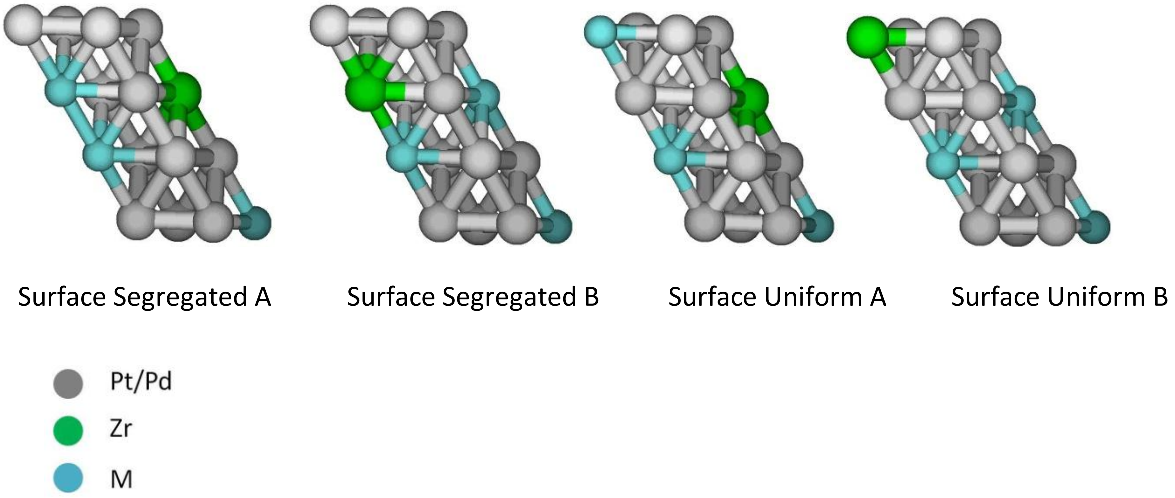

Surface Segregated A Surface Segregated B Surface Uniform A Surface Uniform B

Figure 3. We scan ternary alloys containing Pt/Pd, Z,r and atoms from transition metal columns 4-9. The best cases with good surface segregation and heat of formation are those in the bottom right corner. Alloys containing Rh, Ir, Ru, Os, and Re are the best in terms of alloys with high segregation energy and low heat of formation. In comparison, Pt_3Co and Pt_3Ni have segregation energy ~ 0.5 eV and heat of formation of ~ -0.05 eV. Pt_3Zr has segregation energy of ~ -2 eV and heat of formation ~ -1 eV.